UNIVERSITY of CALIFORNIA
Santa Barbara

Terahertz electro-optic effects in (In)GaAs quantum wells

A dissertation submitted in partial satisfaction of the
requirements for the degree of

Doctor of Philosophy

in

Physics

by

Samuel G. Carter

Committee in charge:

Professor Mark Sherwin, Chair
Professor S. James Allen
Professor Matthew P. A. Fisher
Professor Björn Birnir

December 2004

The dissertation of Samuel G. Carter is approved:

Professor S. James Allen

Professor Matthew P. A. Fisher

Professor Björn Birnir

Professor Mark Sherwin, Chair

December 2004

Terahertz electro-optic effects in (In)GaAs quantum wells

by

Samuel G. Carter

Acknowledgements

First of all, I want to thank Mark Sherwin for being a great advisor. He gave me a chance to work on an interesting project when I wasn't sure whether I wanted to do experimental physics and had little research experience. He has been very patient and supportive and has been more positive about my results than I have been. I also want to thank Mark for being so welcoming and considerate of my family.

Thanks to Mark Su for being a great mentor during my first year in the Sherwin group. He taught me a great deal about experimental physics when I knew very little. He also got me up and running on a good project very quickly. We had a number of good physics conversations, and I even gained from his sometimes warped view on being a graduate student.

Thanks to Victoria Ciulin for being an excellent mentor and colleague during the later part of my graduate student career. She has been very supportive of me as a scientist and a person. I am very grateful for her careful study and criticism of my writing and research, which has given significant improvement. Most of the work presented in this dissertation was performed in collaboration with Victoria, so she deserves a great deal of credit.

Thanks to Matt, Kohl, Nathan, Brendan, Carey, and Tom for being kind,

friendly, and sometimes helpful from when I started in the Sherwin group until now. I've also enjoyed the company of more recent Sherwin group members: Dan, Sang woo, James, and Tristan. I appreciate Tristan's help for performing some FTIR measurements, and I wish him good luck in continuing the THz electro-optic experiments.

I thank Andrew, Chad, and Micah for growing some great samples for me, often in record times. I also thank the cleanroom staff for their help. David Enyeart deserves special appreciation for doing such a great job running and maintaining the Free Electron Laser. I thank him for putting up with all of the different FEL wavenumbers I asked for, particularly for the higher wavenumbers near the end.

I also had the opportunity to work with Professors Martin Koch and James Heyman during their visits to UCSB. I thank them for the valuable experience I gained from them. I also thank Alex Maslov and David Citrin for their theoretical support.

Finally, I am very thankful for the support and sacrifices of my family. My parents have been extremely helpful during this time, and deserve much of the credit for me getting this far. I thank my kids, Charlie, Joey, and Caroline for their love and for taking my mind off physics. Most importantly, I thank my wife for sacrificing a great deal for me to go to graduate school and for her love and unfailing confidence in me.

Curriculum Vitæ

Samuel G. Carter

Education

1999–2004	Ph.D. Physics University of California, Santa Barbara Santa Barbara, California
1994–1999	B.S. Physics, B.A Chemistry Brigham Young University Provo, Utah
1990–1994	University High School Irvine, California

Employment

7/00-12/04	Graduate Student Researcher, University of California, Santa Barbara. Advisor: Prof. Mark S. Sherwin.
9/99-6/00	Teaching Assistant, University of California, Santa Barbara. Supervisors: Prof. Paul Hansma, Jatila van der Veen, Prof. Philip Pincus.

9/96-4/99	Teaching Assistant, Brigham Young University. Supervisor: Prof. David Allred
5/98-8/98	Research Assistant, Brigham Young University. Supervisor: Prof. Harold Stokes
5/97-8/97	Research Assistant, Beckman Laser Institute, University of California, Irvine. Supervisor: Prof. Bruce Tromberg

Publications

S. G. Carter, V. Ciulin, A. V. Maslov, C. S. Wang, L. A. Coldren, and M. S. Sherwin, "Excitonic quantum coherence and strong coupling induced by an intense THz field." (In preparation.)

S. G. Carter, V. Ciulin, M. Hanson, A. Huntington, C. S. Wang, A. C. Gossard, L. A. Coldren, and M. S. Sherwin, "Terahertz-optical mixing in undoped and doped GaAs quantum wells: from excitonic to electronic intersubband transitions." (submitted to Phys. Rev. Lett.)

V. Ciulin, S. G. Carter, M. S. Sherwin, A. Huntington, and L. Coldren, "Terahertz optical mixing in biased GaAs single-quantum wells." Phys. Rev. B **70**, 115312 (2004).

S. G. Carter, V. Ciulin, M. S. Sherwin, M. Hanson, A. Huntington, L. A. Coldren, and A. C. Gossard, "THz electro-optic wavelength conversion in GaAs quantum wells: Improved efficiency and room-temperature operation." Appl. Phys. Lett. **84**, 840 (2004).

M. Y. Su, S. G. Carter, M. S. Sherwin, A. Huntington, and L. A. Coldren, "Strong-field terahertz optical mixing in excitons." Phys. Rev. B **67**, 125307 (2003).

M. Y. Su, S. G. Carter, M. S. Sherwin, A. Huntington, and L. A. Coldren, "Voltage-controlled wavelength conversion by terahertz electro-optic modulation in double quantum wells." Appl. Phys. Lett. **51**, 1564 (2002).

Conference Proceedings

S. G. Carter, V. Ciulin, M. S. Sherwin, C. S. Wang, A. Huntington, and L. A. Coldren, "Terahertz-optical mixing in n-doped GaAs quantum wells: suppression of excitonic resonances," CLEO/IQEC and PhAST Technical Digest on CDROM (The Optical Society of America, Washington, DC, 2004), IMD1.

V. Ciulin, S. Carter, M. Sherwin, A. Huntington, L. Coldren, A. V. Maslov, and D. S. Citrin, "Terahertz electrooptic modulation of a single biased GaAs quantum well," Proceedings of the Quantum Electronics and Laser Science Conference, Baltimore (2003).

S. G. Carter, M. Y. Su, M. S. Sherwin, A. Huntington, L. A. Coldren, "Strong-field, voltage-tunable Terahertz-optical mixing in confined excitons," Proceedings of the 26th International Conference on the Physics of Semiconductors, pR4.3, 2002.

M. Y. Su, S. Carter, M. S. Sherwin, A. Huntington, L. A. Coldren, C. Kadow, and A. Gossard, "Nonperturbative terahertz nonlinear optics of excitons," Proceedings of the Quantum Electronics and Laser Science Conference, vol. 1, p. 61, 2002.

Awards

John Cardy award for strongest academic performance in core first-year graduate courses, 2000.

Abstract

Terahertz electro-optic effects in (In)GaAs quantum wells

by

Samuel G. Carter

The effects of a Terahertz (THz) field on the optical properties of semiconductor quantum wells (QWs) have been studied. The experiments involved driving (In)GaAs QWs with a THz field provided by the UCSB Free Electron Laser. The THz field was polarized in the growth direction to couple to intersubband transitions, while a much weaker near-infrared (NIR) beam probed the interband optical properties.

The interband absorption was significantly affected by the THz field. In an undoped, square $In_{0.06}Ga_{0.94}As$ QW, two exciton states were strongly coupled by the THz field, manifested by a splitting of the exciton absorption. This exciting effect is similar to Autler-Townes splitting in atomic systems and electromagnetically-induced-transparency. The THz field also mixed with the NIR beam to generate sidebands at $\omega_{NIR} + n\omega_{THz}$, where $n = \pm 1, 2, \ldots$. These sidebands were studied extensively in an undoped square GaAs QW sample. The sideband dependence

on NIR and THz frequencies and intensities was studied and modelled along with the effect of a dc electric field. These results have application to ultrafast QW modulators, and the sidebands can be used for wavelength conversion in an optical communication network. The suitability of THz-optical mixing was further demonstrated in a 50 QW sample, which gave improved sideband conversion that was even significant at room temperature.

Finally, sideband generation in doped GaAs QWs was observed for the first time and was quite different from that in undoped QWs. The mixing in doped QWs was primarily sensitive to electronic intersubband transitions while that in undoped QWs was due to excitonic intersubband transitions. These results demonstrate that THz-optical mixing can be used as a tool for probing intersubband dynamics.

Contents

Chapter 1

Introduction

1.1 Motivations

Terahertz electro-optics (THz EO) is the study of the effect of a Terahertz (THz) electric field on the optical properties of matter. In this dissertation, THz EO effects will be examined in thin Gallium Arsenide (GaAs) or Indium Gallium Arsenide (InGaAs) layers that confine carriers into quantum wells (QWs). Such a study is important in terms of device applications, semiconductor spectroscopy, and the strong interaction of light with matter.

Semiconductor QWs have a very important role in optoelectronics, where they are used in QW diode lasers, LEDs, and QW modulators. Such devices are relatively cheap, compact, and can be tuned over a wide range of wavelengths through

band-gap engineering. Fast modulation in optoelectronic devices allows for information transfer with up to ∼50 GHz bandwidth. As this bandwidth increases towards the THz regime, a study of Terahertz EO effects in QWs is particularly important. A related motivation is that in a Wavelength Division Multiplexed (WDM) network, in which information is carried over many channels at different carrier wavelengths, there is a need for all-optical conversion from one wavelength to another. This can be accomplished through THz-optical mixing, one of the primary THz EO effects.

Optical spectroscopy of semiconductors has taken a prominent role over the past few decades, partly due to device applications, but also as semiconductor heterostructures form a controllable laboratory for fundamental physics, particularly in quantum-confined systems. Interband linear spectroscopy of semiconductors in the form of photoluminescence (PL), reflectivity, and transmission is used extensively to characterize semiconductor samples. Intersubband spectroscopy has also been used primarily in doped samples although it tends to be more difficult as intersubband transitions are in the infrared range. Recently, nonlinear spectroscopy, in the form of pump-probe experiments or four-wave mixing, has provided an excellent tool for probing coherent effects in semiconductors that take place over very short time scales.[1] THz EO allows nonlinear spectroscopy involving both interband and intersubband transitions, providing a better understanding of the

interplay of these processes. It also allows the use of near-infrared (NIR) light, as well as mature NIR optics and detectors, to probe intersubband dynamics.

The final motivation for studying THz EO is that novel strong-field physics can be explored. Nonperturbative strong-field effects such as Rabi oscillations and the AC Stark effect have been shown useful in optically manipulating semiconductors. These have mainly utilized NIR light, leaving the THz regime unexplored. Strong THz fields are unique in that the Rabi energy can be comparable to the photon energy without destroying the samples. This leads to quantum states that are strongly "dressed" by the THz field, the first indication of which would be the observation of an Autler-Townes splitting, as initially observed in molecular systems.[2] In doped QWs, the quantum states can be "dressed" by the Coulomb interaction. A strong THz field has been predicted to induce novel nonlinear quantum dynamics in such systems, including optical bistability and chaos.[3]

THz EO is a rich field that has only recently started to be explored. Many results will be presented in this thesis that will illustrate the basic physics of THz EO, reveal the complexity of semiconductor-light interactions, and demonstrate technological applications.

1.2 Semiconductor (GaAs) optical properties

1.2.1 Band Structure

An introduction to the optical properties of semiconductors will be essential to understanding this dissertation. The focus of this section will be on III-V semiconductors, particularly GaAs, as it is central to this work. The band structure of GaAs is a good starting place. The periodicity of the crystal lattice implies that the electronic eigenstates can be written as

$$\Psi_{\vec{k}}(\vec{x}) = u_{\vec{k}}(\vec{x})e^{i\vec{k}\cdot\vec{x}} \tag{1.1}$$

where $u_{\vec{k}}(\vec{x})$ is periodic with the lattice and $\vec{k}$ is the Bloch wave number. This is Bloch's Theorem. The function $u_{\vec{k}}(\vec{x})$ takes on some of the characteristics of the atomic orbitals of the lattice, in particular their symmetry. The Bloch wave number can always be brought into a reciprocal unit cell of the lattice called the Brillouin zone. This is true because factors of $e^{i\vec{G}\cdot\vec{x}}$, where $\vec{G}$ is a reciprocal lattice vector, are lattice-periodic and can be incorporated into $u_{\vec{k}}(\vec{x})$. When all eigenstates are brought into the Brillouin zone, many energy bands are formed, and Eq. (1.1) becomes

$$\Psi_{\vec{k},n}(\vec{x}) = u_{\vec{k},n}(\vec{x})e^{i\vec{k}\cdot\vec{x}} \tag{1.2}$$

where n is the band index.

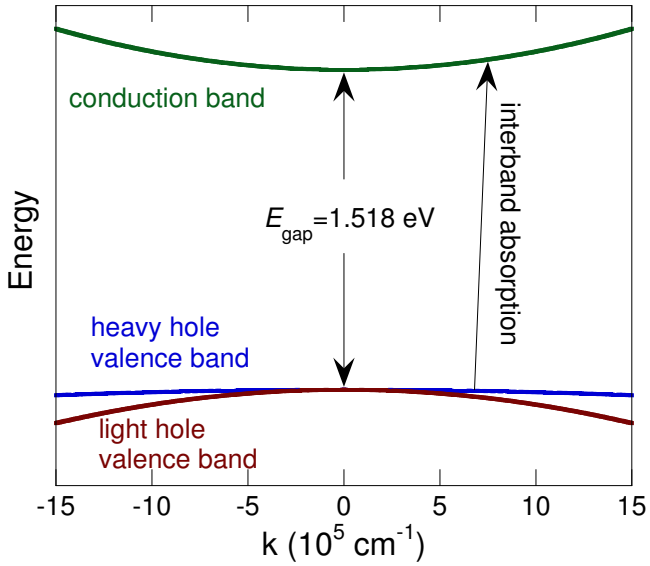

Figure 1.1: Simplified band diagram of GaAs near the Γ point (not to scale). The band gap is given for low temperatures (∼4 K).

In GaAs, there is a direct gap between the lowest empty band, the conduction band, and the highest filled band, the valence band, at the center of the Brillouin zone, called the Γ point, where $k = 0$. These bands are shown in Fig. 1.1. Only the properties of these two bands near $k = 0$ will be considered here. The Γ valley of the conduction band is spherically symmetric with s-like states. It is also parabolic, leading to an effective mass of $0.067m_e$. The valence band is more complicated, with two degenerate bands near $k = 0$, both of which are anisotropic with p-like states. As the bands have different curvature, they are called the heavy-hole and light-hole valence bands.

In intrinsic GaAs, the valence band is largely full, and the conduction band is

largely empty. The thermal distribution of electrons yields very few free carriers even at room temperature due to the significant band gap. The conductivity can be increased by doping GaAs with impurities. In order to n-dope GaAs with electrons in the conduction band, typically Silicon impurities are added. They occupy Gallium sites, donating one extra electron which can ionize and provide free carriers. In p-doping, an impurity such as Beryllium occupies Gallium sites to accept electrons from the valence band. This induces "holes" in the valence band, which also act as carriers.

NIR light can excite transitions from the valence band to the conduction band. The transition rate between valence band and conduction band states is given by Fermi's golden rule in the dipole approximation,

$$W_{\vec{k},v\to\vec{k}',c}(\omega) \propto \left|\langle u_{\vec{k}',c}(\vec{x})e^{i\vec{k}'\cdot\vec{x}}|\hat{e}\cdot\hat{p}|u_{\vec{k},v}(\vec{x})e^{i\vec{k}\cdot\vec{x}}\rangle\right|^2 \delta(E_{\vec{k}',c} - E_{\vec{k},v} - \hbar\omega), \qquad (1.3)$$

where $\hat{e}$ is the electric field polarization unit vector and $\hat{p}$ is the momentum operator. The absorption can be obtained by summing over the valence and conduction band states, resulting in the expression,

$$\alpha(\omega) \propto \left|\langle u_{\vec{k}=0,c}(\vec{x})|\hat{e}\cdot\hat{p}|u_{\vec{k}=0,v}(\vec{x})\rangle\right|^2 n_{opt}(\hbar\omega). \qquad (1.4)$$

This equation applies near $\vec{k} = 0$ at the band edge, where $u_{\vec{k}} \approx u_{\vec{k}=0}$. The function $n(\hbar\omega)$ is the joint density of states, which is zero when $\hbar\omega < E_{gap}$ and proportional to $\sqrt{\hbar\omega - E_{gap}}$ when $\hbar\omega > E_{gap}$ for parabolic bands. However, in undoped GaAs

the absorption near the band edge is strongly modified by excitons, as will be discussed in Section 1.2.3.

1.2.2 Quantum Wells

With the advent of epitaxial growth techniques, such as Molecular Beam Epitaxy, very thin layers of different materials with similar lattice constants can be grown on top of each other with high quality interfaces. AlAs and GaAs have essentially identical lattice constants, so layers of $Al_xGa_{1-x}As$ of any thickness or fraction x can be grown without strain on a GaAs substrate. Growth in this material system is very mature. The properties of $Al_xGa_{1-x}As$ are very similar to that of GaAs up to $x \approx 0.45$, where the gap becomes indirect. The room temperature direct band gap can therefore be varied between 1.423 eV and 2.026 (1.518 eV and 2.176 eV low temperature).[4] This allows the growth of GaAs layers in between $Al_xGa_{1-x}As$ barriers, forming wells in one dimension in which carriers are confined in both the conduction band and valence band. When the thickness of the GaAs layer is comparable to the carrier de Broglie wavelength, quantum confinement becomes significant. A GaAs quantum well is depicted in Fig. 1.2, illustrating the band diagram.

The electronic eigenstates in a semiconductor heterostructure can be expressed simply using the effective mass approximation. In this case, an eigenstate is formed

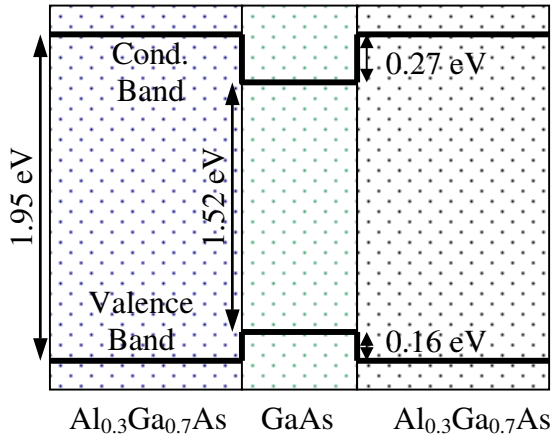

Figure 1.2: GaAs QW with $Al_{0.3}Ga_{0.7}As$ barriers, showing the Γ point of the conduction and valence bands in the different materials. The values of the band gap and the band offset are low temperature values.

from bulk crystal wavefunctions in Eq. (1.2) belonging to a single band, yielding the state,

$$\psi(\vec{x}) = u_{\vec{k}=0,n}(\vec{x})\phi(\vec{x}), \tag{1.5}$$

where n is the index of the conduction band or a valence band and $\phi(\vec{x})$ is the envelope function. This approximation assumes that $\phi(\vec{x})$ varies over distances large compared to the lattice spacing so that the lattice periodic Bloch function, $u_{\vec{k},n}$, can be approximated by the $\vec{k} = 0$ lattice periodic Bloch function, $u_{\vec{k}=0,n}$. It also assumes that $u_{\vec{k}=0,n}$ is the same in all materials used. (See Ref. [5] for more details.)

The envelope function is then determined by the Schrödinger equation, replacing the mass of the electron with the effective mass, m^*, determined by the

curvature of the band at $\vec{k} = 0$:

$$-\frac{\hbar^2}{2m^*}\nabla^2\psi(\vec{x}) + V(\vec{x})\psi(\vec{x}) = E\psi(\vec{x}). \tag{1.6}$$

The function $V(\vec{x})$ is the well potential, which consists of the Γ point of the conduction or valence band as a function of position. For a structure with layers stacked in the z-direction, Eq. (1.6) is separable, yielding

$$\psi(\vec{x}) = \frac{1}{\sqrt{A}}e^{i\vec{k}_\parallel\cdot\vec{x}}\varphi(z), \tag{1.7}$$

where $\vec{k}_\parallel$ is the in-plane wavevector and A is the sample area. The wavefunction $\varphi(z)$ must satisfy the one-dimensional Schrödinger equation,

$$-\frac{\hbar^2}{2m^*}\frac{d^2\varphi_n}{dz^2} + V(z)\varphi_n(z) = E_n\varphi_n(z), \tag{1.8}$$

with energies,

$$E_{n,\vec{k}_\parallel} = E_n + \frac{\hbar^2\vec{k}_\parallel^2}{2m^*}. \tag{1.9}$$

Eq. (1.9) gives rise to a number of subbands in the valence and conduction bands, with minima determined by the confinement in the growth direction. These subbands are illustrated in Fig. 1.3, ignoring some additional complexity in the valence band, such as heavy hole/light hole coupling.

Interband transitions take a similar form as that of Eq. (1.4), but include the overlap of the growth direction envelope wavefunctions, as shown below.

$$\alpha_{n\to n',interband}(\omega) \propto \left|\hat{e}\cdot\hat{p_{cv}}\langle\varphi_n|\varphi_{n'}\rangle\right|^2 n_{2D}(\hbar\omega). \tag{1.10}$$

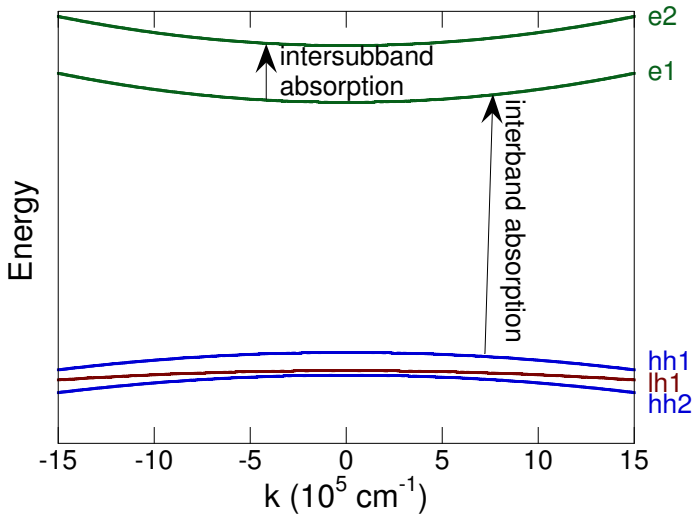

Figure 1.3: Subbands of a quantum well, illustrating interband and intersubband transitions. The electron subbands are labelled with an "e," while the heavy and light hole subbands are labelled by "hh" and "lh," respectively.

The substitution of $\hat{e}\cdot\hat{p_{cv}}$ for $\langle u_{\vec{k}=0,c}(\vec{x})|\hat{e}\cdot\hat{p}|u_{\vec{k}=0,v}(\vec{x})\rangle$ has been made for simplicity. Polarization selection rules become important in QW structures. For an in-plane electric field polarization, interband absorption is allowed from both heavy hole and light hole subbands, with a ratio of 3:1 in strength. For a polarization in the growth direction, however, interband absorption is only allowed from light hole subbands. The envelope functions must also overlap, which means that in a symmetric QW, the conduction and valence band envelope functions must have the same parity. Another change in QW samples is that the 2-dimensional joint density of states, $n_{2D}(\hbar\omega)$, is a constant for $\hbar\omega \geq E_{n'} - E_n$, leading to a step-like structure in the absorption as increasing photon energies make more subbands

accessible.[6]

Absorption can also occur between two different subbands within the same band. In the conduction band, where the subbands are more parabolic, this intersubband absorption takes the form,

$$\alpha_{n\to n',intersubband}(\omega) \propto |\langle\varphi_{n'}|\hat{e}\cdot\hat{p}|\varphi_n\rangle|^2\,\delta(E_{n'}-E_n-\hbar\omega). \tag{1.11}$$

In this case, the polarization must be in the growth direction, and the absorption occurs at a discrete frequency. Obviously, there must also be free carriers in the well for intersubband absorption to occur. This is typically accomplished through modulation doping, in which dopants are placed in the barrier material several 10s of nm away from the QW. This reduces scattering of the carriers by the ionized dopants, improving carrier mobility.

1.2.3 Coulomb interaction

Interaction between carriers significantly affects the optical properties of semiconductors. In doped QWs the Coulomb interaction can be thought of as inducing an effective potential that depends on the charge density. To find the QW eigenstates, the Schrödinger equation and Poisson's equation, which determines the effective potential, must be solved self-consistently. The well potential for a modulation-doped double QW including the effective potential is shown in Fig. 1.4.

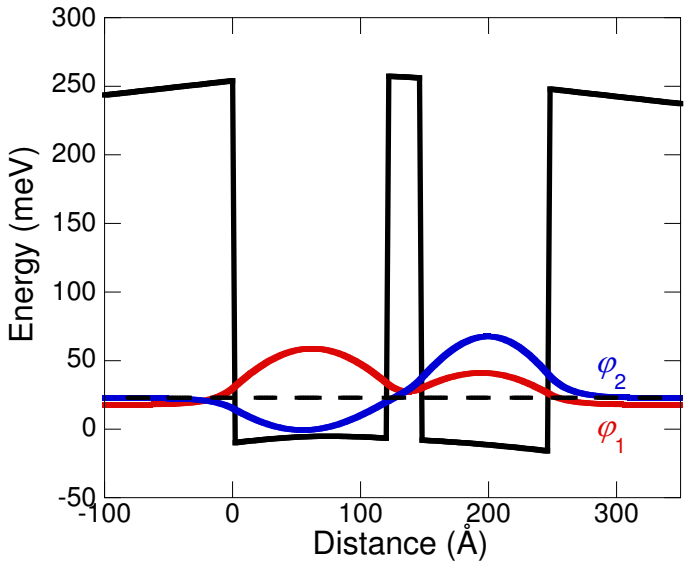

Figure 1.4: Well potential of a modulation-doped double QW, including the effective potential due to the Coulomb interaction. The lowest two envelope functions are plotted as well, offset according to their energies.

The slightly lower potential near the QW edges occurs because the charge density in the ground state is primarily in the center of the wells, giving a higher effective potential there. The Coulomb interaction also modifies the dynamics of the QW, such that a driving field induces collective excitations of the electron gas.[7]

The interband absorption is strongly affected by the creation of excitons: bound electron-hole pairs. When an electron is excited from the valence band to the conduction band, there is a Coulomb interaction between the electron and the hole left behind in the valence band. The bound states are similar to atomic states but with a binding energy of ∼10 meV and a Bohr radius of ∼10 nm, due to a smaller reduced mass and a larger permittivity. The formation of exci-

tons leads to discrete states, which dominate the interband spectrum in undoped GaAs QWs. In significantly doped QWs, this interaction is largely screened by free carriers.

1.3 Background on THz electro-optics

Probably the most well-known electro-optic effect is the Pockels effect, in which an electric field modifies the index of refraction of a crystal. This effect is used for THz detection in various types of THz spectroscopy.[8] The THz field induces a time-dependent birefringence in the crystal, which rotates a NIR probe. The effect is non-resonant and occurs in bulk crystals. In this dissertation, near-resonance electro-optic effects due to changes in the electronic states will be considered. These effects dominate in QW structures.

The first THz EO effect observed was photoluminescence (PL) quenching in undoped [9, 10] and doped [11] QWs. In the presence of the in-plane THz field, the PL was weaker and broader. This effect was explained as being due to free carrier heating, either of photoexcited carriers in undoped wells or the electron gas in the doped case. The heating fit a Drude model, which meant that the effects were largely non-resonant. In a magnetic field, however, resonant PL quenching was observed in an undoped well when the THz field was resonant with internal

transitions of excitons.[12]

While studying changes in magnetoexciton PL, Černe and Kono discovered sidebands at $\omega_{NIR} \pm n\omega_{THz}$, where ω_{NIR} is the NIR laser frequency, ω_{THz} is the THz frequency, and n is an even integer.[13] These sidebands were attributed to four-wave mixing of the NIR and THz fields, and application to optical communications was discussed. The resonant structure was further characterized, illustrating that sideband generation could also be used for spectroscopy.[14] The results were explained by a $\chi^{(3)}$ model in which the sidebands were strongest when the NIR frequency was resonant with interband excitonic transitions and the THz frequency was resonant with the $1s \rightarrow 2p^+, 2p^-$ transitions. These experiments generated a great deal of theoretical interest in sideband generation in QWs due to an in-plane THz field,[15, 16, 17, 18] most of which related to strong-field effects.

Nordstrom *et. al.* experimentally demonstrated one such strong-field effect by examining the effect of the THz field on the interband absorption.[19] They probed the NIR tranmission of $In_{0.2}Ga_{0.8}As$ QWs and observed shifts attributed to the dynamic Franz-Keldysh effect and the ac Stark effect. Interesting nonperturbative effects have also been measured in QW samples and bulk GaAs samples using strong mid-infrared fields.[20, 21] Numerous theoretical papers have been written on these effects,[15, 16, 17, 18, 22, 23] predicting shifts in the absorption and even a splitting of the $1s$ exciton when the $1s \rightarrow 2p$ transition is resonantly driven

(similar to Autler-Townes splitting in atomic systems.[2])

All of the above-mentioned effects in QWs used THz fields polarized in the QW plane. The effects can be quite different when the THz field is polarized in the growth direction. This is well-known for static electric fields. In-plane electric fields will quench QW PL when tens of V/cm are applied [24] due to exciton ionization. A growth direction electric field cannot ionize the excitons for fields of tens of kV/cm due to the confinement, but it does shift the QW energies and decreases the PL as part of the Quantum Confined Stark effect.[25, 26] Similar differences occur for THz electric fields, as well as the fact that a growth direction THz field couples to intersubband transitions. The focus of this thesis will be on fields polarized in the growth direction.

Phillips and Su [27] were the first to demonstrate sideband generation with a THz field polarized in the growth direction. An asymmetric coupled QW (ACQW) structure (see Fig. 1.4) was used to eliminate inversion symmetry, thus allowing $\chi^{(2)}$ processes which generate sidebands with odd multiples of ω_{THz}. This included $n = +1$ sidebands, which are generated most efficiently for moderate THz fields. ($n = +1$ sidebands can be generated in bulk GaAs, due to the noncentrosymmetric lattice.[28] In this case polarization components of the incident NIR beam, the sidebands, and the THz beam must be orthogonal.) Figure 1.5 displays the sideband spectrum of a similar ACQW sample. Coupled QWs were used so that

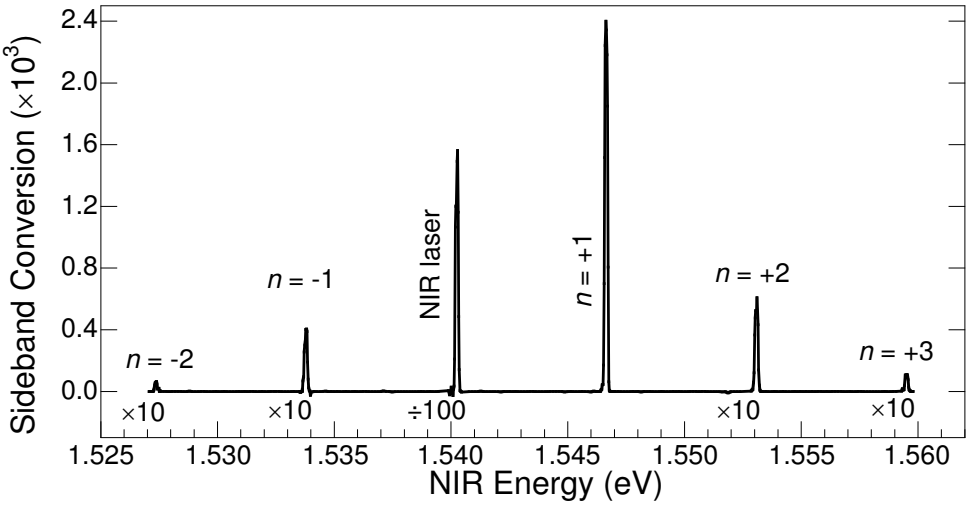

Figure 1.5: Transmitted sideband spectrum of a multiple ACQW sample (SC4) at 20 K, taken using the UCSB FEL at 1.5 THz (6.4 meV). The transmitted beam at ω_{NIR} is divided by 100 and the $n = +3, +2, -1, -2$ sidebands are multiplied by 10 for clarity. The THz power was ∼1 kW and the NIR power was 0.2 mW.

the tunnel splitting produced an electron intersubband spacing in the range of the THz source, the UCSB Free Electron Laser (FEL). Sidebands were strongest when the NIR was resonant with interband exciton transitions and when the THz was resonant with excitonic intersubband transitions.

These experiments were extended to gated ACQW samples by Su and Carter [29]. The gates were used to apply a dc electric field to the QWs, tuning the intersubband spacing as well as the interband energies. The results demonstrated voltage-controlled all-optical wavelength conversion using THz EO, something particularly useful in optical communications. The resonant structure was also mapped out and modelled in terms of excitonic intersubband transitions.[30] A

number of theoretical papers also explored sideband generation in QWs with a growth direction THz field,[31, 32] and some explored the effect of an additional dc electric field as well.[33, 34] Strong THz field effects were observed in the same sample by examining the dependence of sideband generation on the THz power. A non-monotonic dependence on THz power was observed and interpreted as being due to a "dressing" of the exciton states by the THz field.[35]

Considerable theoretical attention has been paid to changes in interband absorption in the presence of a strong, intersubband pump field.[36, 37, 38] These papers predict very interesting effects, such as an Autler-Townes type splitting of the exciton resonance and replicas of the exciton lines. Until now, very few experimental results have been observed on this subject.

In this dissertation, THz EO effects in GaAs QWs will be further examined by studying THz-induced changes in the interband absorption and by studying THz-optical mixing in a variety of different samples. In the next chapter, the sample design, characteristics, and experimental methods for such experiments will be discussed. Then, Chapter 3 will present results on changes in the interband absorption spectrum of a square InGaAs QW. In Chapter 4 THz-optical mixing in a similar GaAs QW sample will be examined in detail, demonstrating the resonance structure and technological implications. The application to wavelength conversion will be further demonstrated in Chapter 5 by results on high sideband

conversion efficiency and room-temperature operation in a 50 ACQW sample. Chapter 6 will explore sideband generation in doped QWs and its sensitivity to intersubband dynamics. Efforts to observe chaotic dynamics in such strongly driven systems using sidebands will be presented in Chapter 7.

Chapter 2

Sample design and Experimental methods

2.1 Sample design

Sample design has been a significant challenge in these experiments. The properties of the QWs are important, as well as effective interaction of the QWs with THz and NIR radiation. The samples typically must also be fabricated into gated devices. Several of the design constraints are listed below.

1. The samples must have strong interband and intersubband oscillator strengths, and the intersubband spacing should be within the range of the FEL.

2. The THz field must be coupled into the sample with a significant growth-direction THz field at the QW positions. In-plane THz fields should usually be much weaker.

3. The NIR beam must be effectively coupled in and out of the sample, with a significant interaction with the QWs.

4. Often, a dc electric field must be applied to the QWs.

Figure 2.1 displays two sample structures and experimental geometries that have been used to satisfy the above conditions for the THz electro-optic experiments. An explanation is presented in the following subsections.

2.1.1 Quantum well design

The samples have all been grown by molecular beam epitaxy at UCSB by Andrew Huntington, Chad Wang, or Micah Hanson. Andrew and Chad worked in the Larry Coldren research group, and Micah worked in the Art Gossard research group. Details on specific samples can be found in Appendix C.

Most of the samples consist of GaAs QWs with $Al_{0.3}Ga_{0.7}As$ barriers, due to the maturity of growth in the system, lack of strain in such samples, and the narrow linewidths observed. Also, GaAs QW absorption is within the range of our tunable Ti:sapphire laser. The main difficulty with GaAs QW samples is that

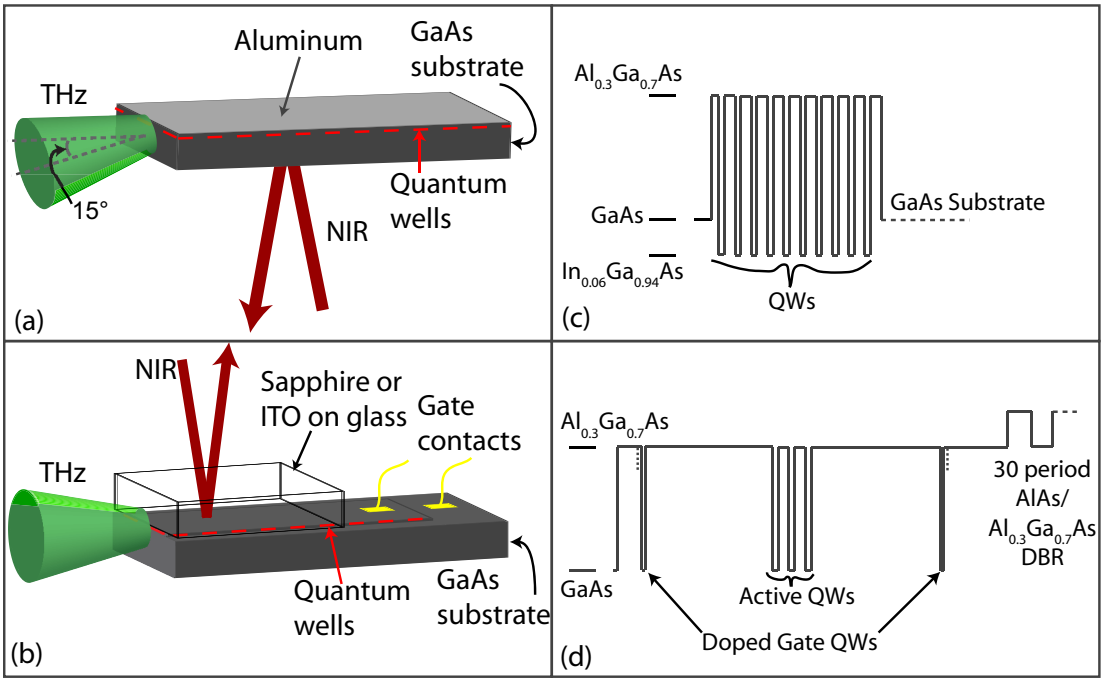

Figure 2.1: Two experimental geometries, (a) and (b), and their typical sample structures as illustrated by their respective conduction band profiles, (c) and (d).

NIR light resonant with QW states is absorbed by the GaAs substrate. In order to effectively couple NIR light out of the sample, the substrate must be removed, or a Distributed Bragg Reflector (DBR) must be grown behind the QWs. To avoid this problem, InGaAs QWs can be used, for which the QW absorption is below the GaAs band edge. The tradeoff is that InGaAs QWs don't seem to be grown as reliably, there can be significant strain, and the linewidths are broader. Also, the performance of most of our detectors becomes quite poor below the low-temperature GaAs band edge. Still, these InGaAs QWs samples have shown a great deal of promise for THz EO experiments.

The simplest QW structure is of course a single square QW. The band diagram of square GaAs QWs with $Al_{0.3}Ga_{0.7}As$ barriers is illustrated in Fig. 2.2(a) and (b). The lines represent the bottoms of the subbands as calculated using Greg Snider's 1D Poisson program.[39] Due to the low effective mass of electrons, the spacing of conduction subbands is much higher than that of heavy holes. In order to have a conduction subband spacing of a few THz (the optimum range for the FEL), a square GaAs QW must be about 300 Å or more as in Fig. 2.2(a). Such wide QWs can be used, but have weaker electron-hole overlap, leading to weaker interband absorption. They also have a multitude of closely-spaced hole subbands. This can be avoided with narrower coupled QWs, in which tunnel splitting produces two closely spaced electron subbands as in Fig. 2.2(c). There are fewer closely spaced

hole states although the interband spectra are still quite complicated. An added advantage is that the QWs can be made asymmetric. A number of experiments on such asymmetric coupled QWs (ACQWs) will be discussed in this dissertation. A QW with a heavy hole subband spacing within the range of the FEL can be as narrow as ∼130 Å, as in Fig. 2.2(b), leading to much simpler interband spectra. A number of interesting THz electro-optic effects in these wells will be discussed.

The number of QWs in a sample is also an important consideration. Having multiple QWs makes the absorption and changes in the absorption much easier to observe. Also, sideband generation tends to scale with the number of wells squared. For these reasons, all of the samples discussed will be multiple QWs. However, uniformity and complexity is an issue in multiple QWs, particularly in multiple doped QWs, where the charge density can vary significantly between QWs. Also, in multiple doped QWs, the charge density can no longer be controlled with a gate voltage, taking away a degree of freedom and making intersubband absorption measurements more difficult.

Gate Quantum Wells

In addition to the "active" QWs for the THz EO experiments, doped gate QWs are typically included in the samples. Ohmic contact was made to these QWs in order to apply a dc electric field across the active QWs. The gate QWs are made

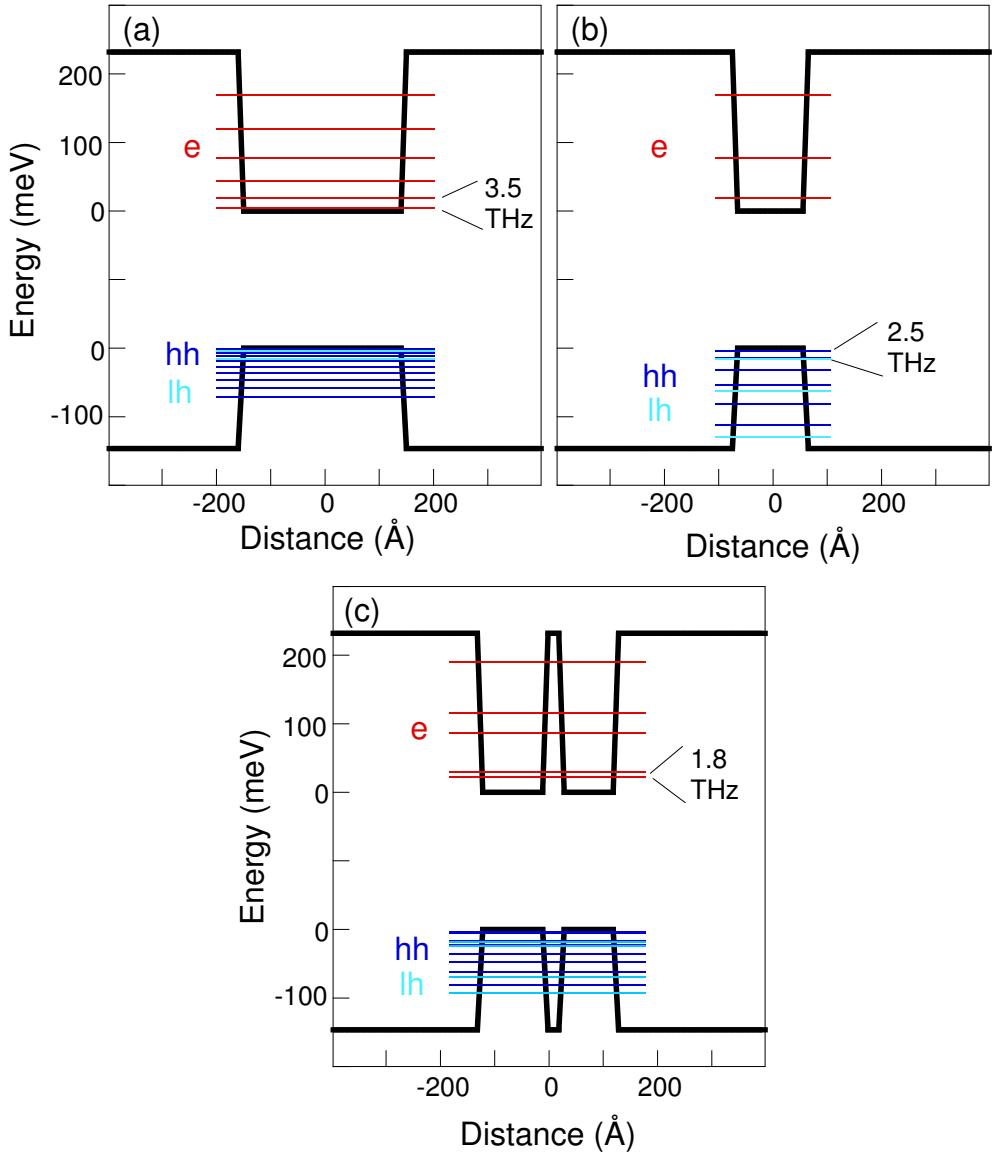

Figure 2.2: Conduction band and Valence band of (a) a 300 Å QW, (b) a 130 Å QW, and (c) coupled QWs. The lines represent the bottoms of the conduction subbands (red), heavy hole subbands (dark blue), and light hole subbands (light blue) as calculated by Greg Snider's 1D Poisson program.[39]

quite narrow (70-80 Å) so that their interband and intersubband transitions are well above those of the active QWs. The gate QWs are modulation doped to $\sim 1 \times 10^{12}$ e/cm^2 and are placed at least several thousand Å away from the active wells.

2.1.2 Near-infrared coupling

In GaAs QW samples, coupling NIR light in and out of the QW layers can be difficult due to the substrate. Interband absorption experiments can be done without a DBR or substrate removal using Photoluminescence Excitation (PLE), in which photoluminescence (PL) is measured while scanning the excitation wavelength. This method would not work well for THz EO experiments because THz affects both the absorption and the PL, confusing the two. Another possibility is to measure the NIR light reflected off of the QWs. This typically gives a rather indirect measure of the interband absorption, and sidebands measured in this way have been weak.

In most of the GaAs samples used in these experiments, a Distributed Bragg Reflector (DBR) was grown underneath the QWs as illustrated in Fig. 2.1(d). The DBR consists of 30 alternating layers of AlAs and $Al_{0.3}Ga_{0.7}As$, each of thickness $\lambda_{NIR}/(4n)$, where λ_{NIR} is chosen to be close to the QW absorption and n is the index of refraction of the layer.[40] Each DBR is actually quite thick ($\sim$4 μm) and

must be grown very accurately to be close to the desired λ_{NIR}. The reflectivity of a sample with a DBR is displayed in Fig. 3.5 on page 59. Ignoring the QW absorption near 1.535 eV, the DBR looks mirror-like from 1.48 to 1.58 eV, the range called the stopband.

NIR light reflected off of the DBR will interfere with the incident NIR light, giving nodes and antinodes. The sample should be designed so that the QWs are placed at the antinodes, which are spaced by $\lambda_{NIR}/(2n)$, $\sim$120 nm. In some samples, such as that illustrated in Fig. 2.1(d), a small number of closely-spaced QWs were all placed close to one antinode. In the doped samples, each QW was placed at an antinode as the modulation doping necessitated significant space between wells.

Due to the high index of GaAs, internal reflection at the surface is quite significant. This results in some cavity effects, in which the electric field and the absorption are enhanced at certain NIR wavelengths. The enhancement should take place at λ_{NIR} when the cavity length is a multiple of $\lambda_{NIR}/(2n)$. A transfer matrix program was used in the design process to calculate the reflectivity of samples to enhance the QW absorption. In Fig. 3.5 on page 59, a cavity mode centered near the QW absorption can be seen, illustrating the enhancement.

Samples with DBRs must be designed for a certain temperature because the QW absorption shifts by about -90 meV going from low temperatures to room

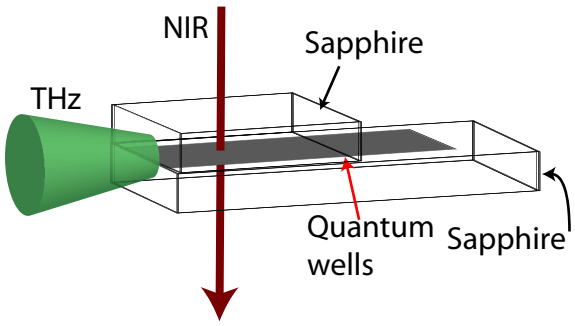

Figure 2.3: Illustration of a sample with its substrate removed, glued in between two pieces of sapphire, along with incident NIR and THz beams.

temperature. One multiple GaAs QW sample was grown with a stop-etch layer instead of a DBR. The sample was glued to a piece of sapphire, and the substrate was etched away. Another piece of sapphire was then glued to the exposed side of the sample (see Fig. 2.3). The NIR coupling was much simpler due to the lack of a DBR, and the transmission and sideband generation could be measured from low temperatures to room temperature.

NIR coupling for InGaAs samples is even simpler as the substrate is transparent at the QW energies. One can work in transmission, but for most of the experiments discussed, an Aluminum layer is deposited on the sample frontside to improve THz coupling. In this case, the NIR light is coupled in through the substrate, and reflected light is detected as shown in Fig. 2.1(a).

2.1.3 THz coupling

Obtaining a significant growth-direction THz field at the QW layers has been a challenging problem. In intersubband absorption measurements, a strong growth-direction field is typically obtained by depositing a good conductor such as Al on the surface and coupling the THz into the edge.[7] A good way to understand the effect of the metal is to imagine a plane wave inside the semiconductor reflecting off of the metal, as illustrated in Fig. 2.4(a). The boundary condition at the metal interface eliminates in-plane fields and gives constructive interference for the growth-direction field. The growth-direction surface field is plotted as a function of incident angle in Fig. 2.4(b). The THz field is edge-coupled into the sample, so the angle of incidence should be near 90°, particularly with the high refractive index of GaAs.

However, for THz electro-optic experiments, NIR light must be coupled into the sample, typically through sample frontside. If the metal is removed from the sample surface, the THz field becomes very weak at the surface, and in-plane fields become significant, as displayed in Fig. 2.4(b). This fact was demonstrated in earlier THz EO experiments with Mark Su.[30] When nothing was placed on the sample surface, THz-optical mixing was much weaker. The solution developed by Su was to clip Sapphire onto the sample surface as illustrated in Fig. 2.1(b).

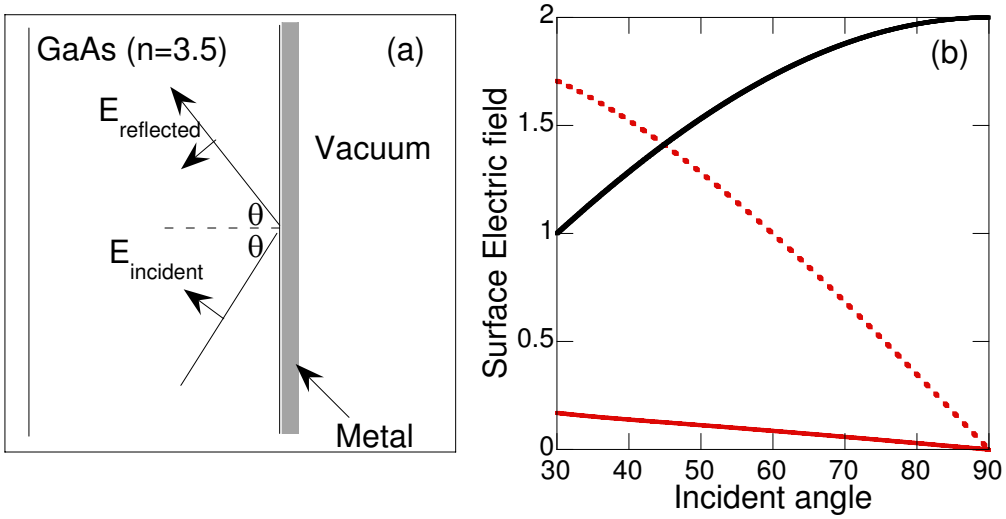

Figure 2.4: (a) Illustration of plane wave inside GaAs reflecting off of a metal on the surface. (b) Graph of the surface electric field as a function of the angle of incidence with a metal coating (solid black line) and without (red lines). Without the metal coating, both in-plane (dashed, red) and growth direction (solid, red) fields are present.

Sapphire is transparent for the NIR and at low temperatures is transparent for THz. Also, its slow axis index of refraction at THz frequencies is matched to GaAs. Sapphire pressed onto GaAs should form a thicker dielectric waveguide for the THz, with the QWs at the center. This method gave somewhat improved THz-optical mixing,[30, 35] and was used in several of the experiments presented here. The THz coupling of the thinned sample glued between two pieces of sapphire should be similar.

However, the effect of gaps between the sapphire and the GaAs must be considered. These gaps were evident from interference fringes seen when the sapphire

was pressed onto the GaAs with a clip. Based on the fringes, the gap could be quite small (∼100 nm) near the clip, but was probably closer to ∼1 μm near the sample edge. It would seem that the gap is so much smaller than the THz wavelength (∼100 μm) that it would have no effect. In the edge-coupled geometry, however, the gap is predicted to have a significant effect, as shown in Fig. 2.5. Even for gaps of several hundred nm, the growth-direction field is significantly reduced near the surface. This gap effect likely reduced the THz field near the surface for the experiments that will be discussed.

Another issue is whether in-plane fields are present using the sapphire. Even if the incident THz field is completely polarized in the growth-direction, reflections inside the sample can produce in-plane fields comparable to the growth direction fields at the surface. As will be discussed in Chapter 3, in-plane THz fields can give large unwanted affects in QW samples. This led to pressing Indium Tin Oxide (ITO) coated slides onto the sample surface. ITO is semi-transparent for NIR light but conducts at THz frequencies.[41] The conductive layer on the surface should suppress any in-plane fields. However, as shown in Fig. 2.6, gaps between the ITO and sample surface may cause the same problems as for the sapphire. Significant THz-EO effects have been observed using ITO and using sapphire, but the strength and polarization of the THz field are still uncertain.

The most successful method of coupling in the THz field has been to use

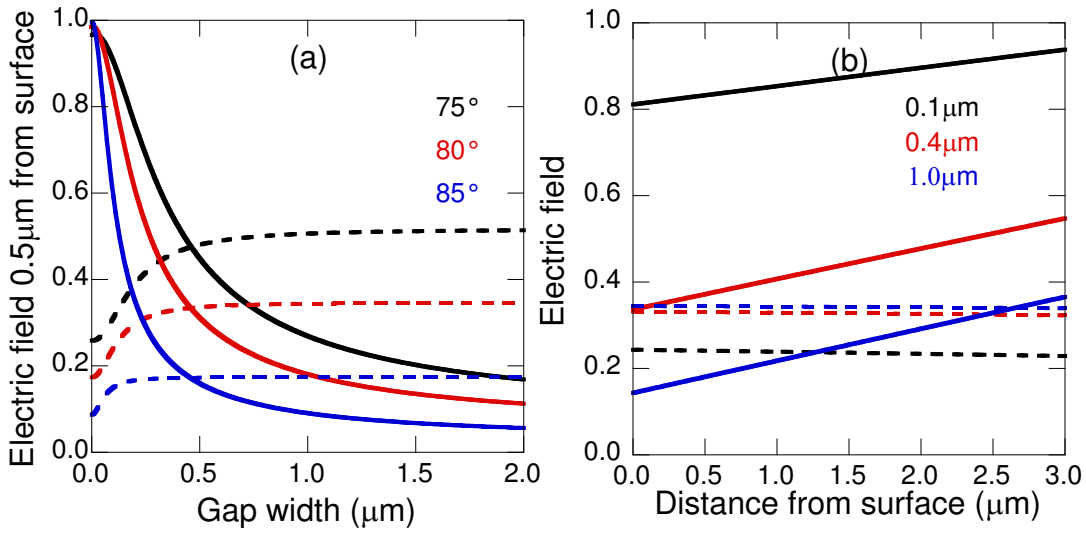

Figure 2.5: (a) Plots of the calculated electric field 0.5 μm into the sample vs. the gap width between GaAs and sapphire. The calculations were performed using the Fresnel equations for a wavelength of 100 μm and plotted for several different incident angles, 75° (black lines), 80° (red lines), and 85° (blue lines). The solid lines represent the growth-direction field and the dashed lines represent the in-plane field. (b) Graph of the calculated electric field vs. position inside the sample relative to the surface. The incident angle is 80°, and the fields are plotted for an air gap of 0.1 μm (black), 0.4 μm (red), and 1.0 μm (blue).

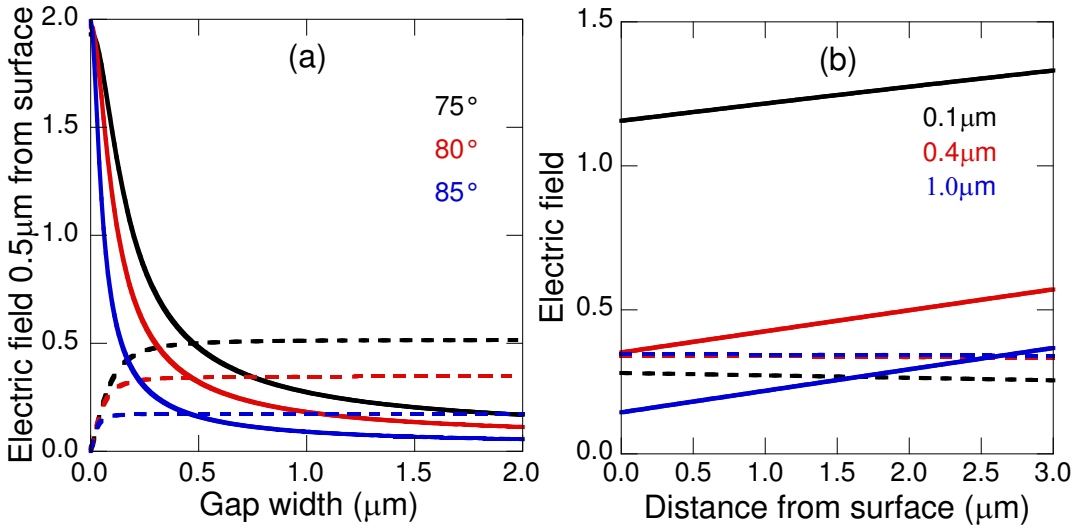

Figure 2.6: (a) Plots of the calculated electric field 0.5 μm into the sample vs. the gap width between GaAs and ITO. The calculations were performed using the Fresnel equations for a wavelength of 100 μm, assuming a perfect conductor for the ITO. The calculations are plotted for several different incident angles, 75° (black lines), 80° (red lines), and 85° (blue lines). The solid lines represent the growth-direction field and the dashed lines represent the in-plane field. (b) Graph of the calculated electric field vs. position inside the sample relative to the surface. The incident angle is 80°, and the fields are plotted for an air gap of 0.1 μm (black), 0.4 μm (red), and 1.0 μm (blue).

InGaAs QWs and deposit a layer of Al on the sample frontside. This gives a strong growth-direction THz field with no in-plane field. The NIR light is coupled in through the substrate as shown in Fig. 2.1(a) and reflected off of the Al.

2.2 Device fabrication

For many of the samples used, the application of a dc electric field was necessary to eliminate inversion symmetry or to tune the intersubband spacing. The field was applied by making ohmic contact to the front gate (FG), the doped gate QW near the surface, and to the back gate (BG), the doped QW below the active QWs. For doped active QW samples, the fabrication of devices to measure the intersubband absorption and capacitance-voltage (CV) devices to measure charge density was necessary. The fabrication of all these devices will be discussed below. Details on the processing steps can be found in Appendix A.

2.2.1 THz Electro-optic devices

The first step for processing the THz EO devices is to etch several, long, 1 mm wide mesas, as illustrated in Fig. 2.7. The mesa etch is performed primarily so that ohmic contact can be made to the back gate. Some early devices were fabricated by just etching the right side of the sample. Several devices were then

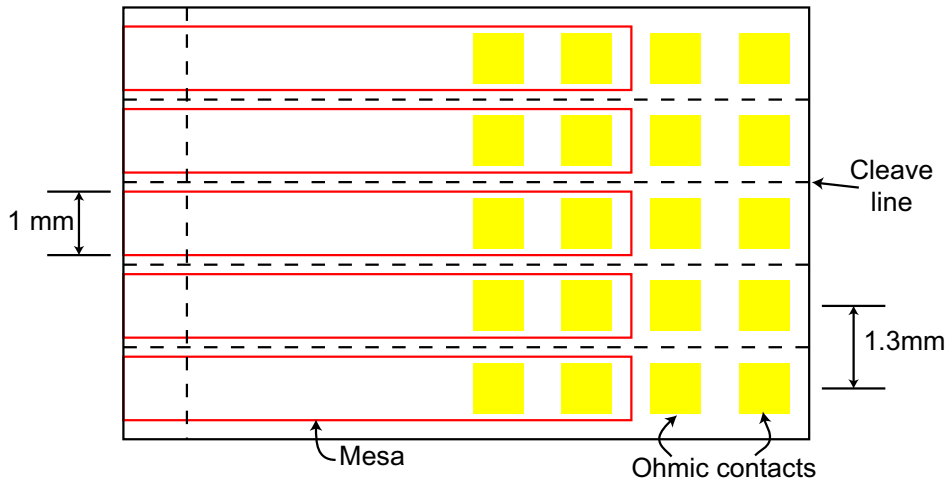

Figure 2.7: Illustration of a sample processed into THz electro-optic devices.

obtained by cleaving the sample into long, thin pieces, which was also useful for confining the THz radiation to a smaller area. This method gave a poorer yield than etching several devices because metal inadvertently deposited on the wafer edge would often short the two gate QWs. Isolating the mesas from the edge and from each other significantly improved the yield. The etch should go down to about 1000-1500 Å above the BG QW. A wet etch, NH_4OH:H_2O_2:H_2O (10.5:1.8:150), is typically used. This etch is rather critical because etching too far may deplete the BG, due to the migration of charge to the surface states. Not etching far enough means that the alloy used for ohmic contact, typically GeAu, may not diffuse down far enough to make good contact.

The next step is to deposit Ni/Ge/Au/Ni/Au (50/177/350/100/2000 Å) onto

the mesas and onto the etched area, as displayed by the yellow squares in Fig. 2.7. The Ge/Au layers form an alloy that is used to heavily dope the area, forming an ohmic contact to the QWs. The 2000 Å layer of Au gives a thick pad for bonding to wires. The Ni layers form diffusion barriers and may have other effects as well. Two contacts are deposited for each FG and BG QW for each device. Measuring the resistance between two BG or FG contacts allows one to check that the contacts are ohmic. The contacts are not ohmic until the sample is annealed at 430°C for 30 s. At this temperature, the Ge/Au alloy spikes down to the QW layer, forming a good contact. A typical resistance between good ohmic contacts to the same gate QW is $\sim$1 kΩ.

Forming good ohmic contacts and not shorting the FG and BG has been the main challenge in fabricating these devices. As stated previously, if the etch is not just right, the ohmic contact to the BG will be quite poor. One solution that has been used to eliminate this problem is to use In contacts for the BG. It spikes down much farther ($\sim$1 μm) than Ge/Au, so the etch becomes less critical. Shorting of the gates is a more difficult problem. While good ohmic contact with Ge/Au will typically only be obtained when the QW is within a few thousand Å of the surface, sometimes the Ge/Au on the mesa seems to spike down much further, partially shorting the FG and BG. The best way to address this problem seems to be making distance between the FG and BG QWs at least 1 μm. It is

also critical to ensure that there is no Ge/Au alloy on the edge of the mesa. When the devices are fabricated correctly, about 80% of the devices have good ohmic contact with no shorting. However, the current-voltage (IV) characteristics still vary quite a bit between the devices. The best devices will give a field of ∼20 kV/cm with little leakage current (less than ∼0.1 μA).

The last step is to cleave the sample up into thin pieces as illustrated by the dashed lines along the sample in Fig. 2.7. This should better confine the THz within the sample, and it also saves space on the cryostat sample mount so that several of these narrow pieces from different QW samples can be mounted together. Usually, the left edge of the sample is cleaved off as well. This is to eliminate shorting that tends to occur due to Ge/Au on the edge of the sample.

2.2.2 FTIR devices

An FTIR device is designed for Fourier Transform Infrared (FTIR) spectroscopy measurements of intersubband absorption. It must effectively couple in infrared radiation with a significant field in the growth direction at the QW positions. This is accomplished simply by depositing Al on the front and back of the sample so that infrared light edge-coupled into the sample couples into TEM modes. The device also should be able to deplete the active QWs to get a good reference for the FTIR spectra. However, in multiple QW samples this is often not

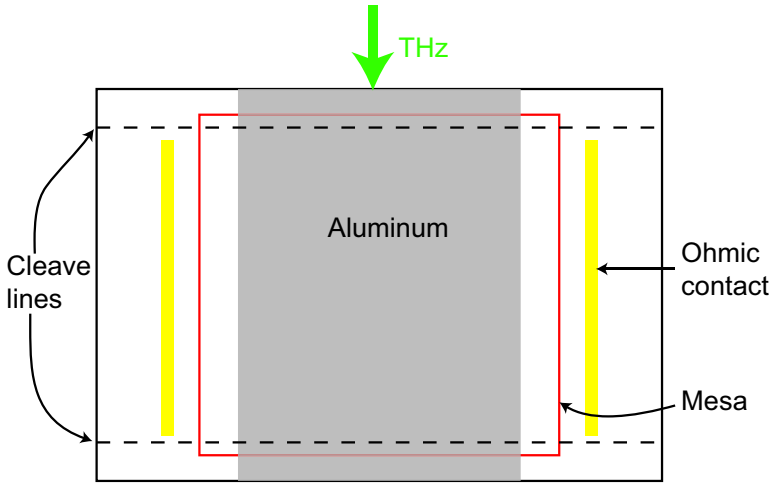

Figure 2.8: Illustration of a sample processed into an FTIR sample.

possible because there are simply too many wells to deplete. Instead, the device applies an electric field to the active QWs in order to measure the intersubband absorption as a function of electric field. The field is applied using the Al on the front surface as one gate and by making ohmic contact to the BG for the other. A typical design for FTIR devices is displayed in Fig. 2.8.

First, an etch is made down close to the BG, defining a large mesa in the center. Ohmic contacts, using Ge/Au or In, are deposited on the etched region and annealed. Then, Al is deposited on the mesa (and part of the etched region) and over the whole back side. Finally, the top and bottom edges are cleaved off so that there is no Al connecting the BG region and the mesa.

2.2.3 CV devices

The function of a CV device is to have a large capacitance between a FG and the active wells and to be able to deplete one or more of the active wells. The FG QW can be used, but typically a large Al Schottky gate is used instead because higher depletion voltages can typically be obtained this way. The process is quite similar to that of the FTIR devices. First, an etch is made down to about 1500 Å above the first active well, defining a large mesa. Sometimes the mesa is etched down to within $\sim$0.5 μm of the first active well, so the Schottky gate is closer to the active wells. Ohmic contacts, using Ge/Au or In, are deposited on the etched region and annealed. In has the advantage of contacting more of the wells. Then, Al is deposited on the mesa, and the edges are cleaved off as in the FTIR samples.

2.3 Experimental setup and measurements

This section will discuss how THz EO experiments are performed and what sources, detectors, and optics are used for THz and NIR radiation. Many more details can be found in Appendix G. An illustration of the experimental setup is shown in Fig. 2.9.

2.3.1 Sample

The sample is mounted in a closed-cycle He refrigerator, the temperature of which can be varied between 10 K and room temperature. The sample sticks out over the edge of the sample mount so that the THz radiation can couple into the cleaved edge. Any gold wires connected to gates on the sample are In soldered to sample mount pins, which can be connected to several twisted pair wires connected to a breakout box. Voltages applied to the sample are typically pulsed for less than 1 ms to overlap each measurement. Pulsing the voltage avoids heating and migration of charge between wells.

2.3.2 Terahertz

The source of Terahertz radiation for THz EO experiments is the UCSB Free Electron Laser (FEL), which provides kilowatt-level power from 0.12 to 4.8 THz. The FEL is quasi-CW, putting out 1-10 μs pulses at a repetition rate of typically 0.75 or 1.5 Hz. In principle, the FEL is continuously tunable, but is often used in "water windows," where absorption by atmospheric water is low. The experiments discussed in this dissertation were performed in water windows to avoid purging or evacuating the experimental area.

The FEL is connected to the experimental setup with an evacuated optical

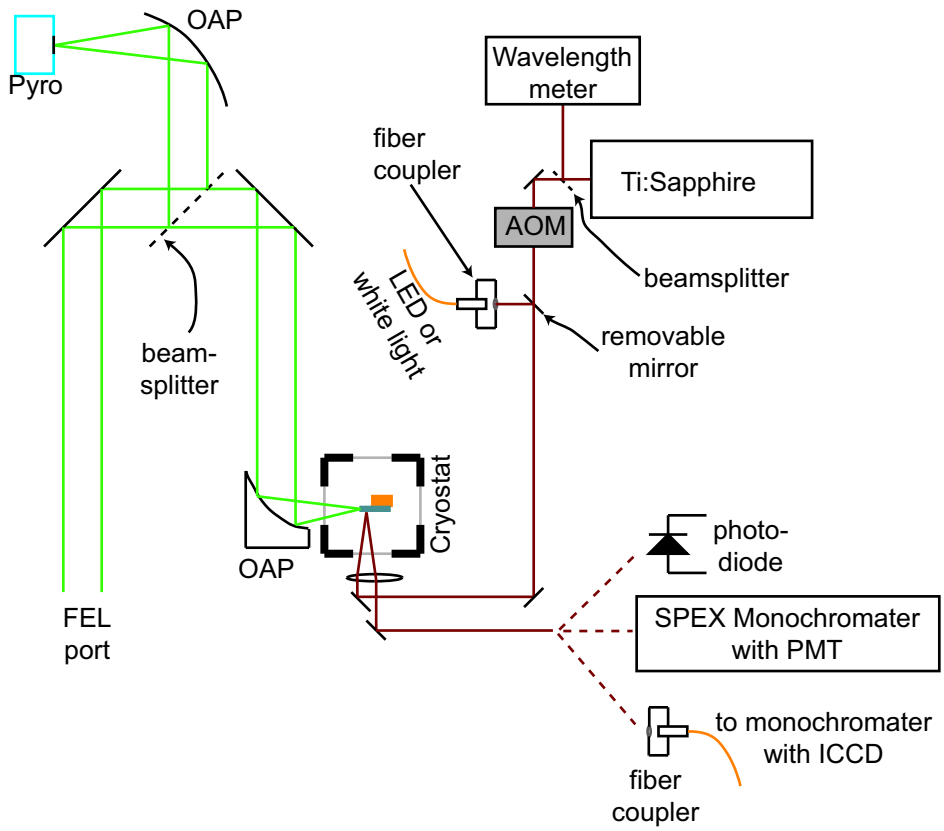

Figure 2.9: Illustration of the experimental setup.

transport system. The THz beam must pass through a focusing lens in the transport system before reaching the setup to prevent divergence of the beam. This gives the beam a relatively small diameter ($\sim$1.5 inch) at our port. As displayed in Fig. 2.9, the beam passes through a thin, polyethylene beamsplitter, which directs a small percentage of the power ($< 10\%$) to an off-axis parobolic mirror (OAP) focusing onto a reference pyroelectric (pyro) detector. The rest of the THz beam is directed to the cryostat and focused onto the edge of the sample with an OAP (3 inch focal length). In some measurements a 6 inch focal length OAP was used. The reference pyro is used to monitor the power during an experiment but is not well-calibrated. For absolute measurements of the THz power, the self-calibrated Thomas Keating detector is placed just before the final OAP. The THz spot size at the focus was also measured for several different THz frequencies, giving a good estimate on the THz intensity. Details on measurements of the power and spot size are given in Appendix B.

2.3.3 Near-infrared

There are three sources of NIR radiation used in these experiments: a cw, tunable, Titianium:Sapphire laser; infrared LEDs; and "white light" from a lamp. The Coherent 890 Ti:Sapphire laser is pumped by a Coherent Innova 300 Argon laser and puts out $\sim$500 mW, 30% of which is sent to a New Focus Fizeau wave-

length meter. The remaining beam is sent through an Intraaction AOM-602N acousto-optic modulator (AOM), which chops the beam into ∼200 μs pulses that overlap the THz pulses. The laser is pulsed to limit the energy incident on the sample and to avoid overloading the detector, but pulsing is not strictly necessary. The laser is focused onto the sample (high f-number) near normal incidence to a spot size of ∼50 μm.

The infrared LEDs and the lamp are used for measuring interband spectra. White light from the lamp is useful for linear optical measurements, but the power per nm is too low for THz EO experiments. The LEDs used have broad (50 nm FWHM) emission wavelengths centered at either 810 nm (Zarlink MF272) or 850 nm (Appointech). Light from the LEDs is coupled into a multimode fiber (62.5 μm core) either by the LED manufacturer or with a fiber coupler. This forces the output of the fiber to come from a more point-like source, but decreases the power to less than ∼100 μW (for manufacturer coupled LEDs). A fiber output coupler in the THz EO setup sends the light onto a removable mirror, which directs it along the same path as the NIR laser. The LED light is focused onto the sample with a diameter of 200-300 μm, much larger than for the laser.

Depending on the sample and the experiment, the transmitted NIR beam, the reflected NIR beam, or photoluminescence is collected and sent to one of several different monochromators/detectors. For high resolution measurements, the

NIR light is sent to a SPEX 0.85m double monochromator with a Hamamatsu R7400U-20 photomultiplier tube (PMT) detector. To measure a NIR spectrum with somewhat lower resolution all at once, the light can be sent through a multi-mode optical fiber to an Acton 0.275 meter triple grating monochromator with a Princeton Instruments intensified CCD (ICCD). Both detectors amplify electrons ejected from a photocathode, which provides the high, noise-free gain needed for these experiments. However, the photocathode quantum efficiency for both starts to get weak past ∼800 nm. For reflectivity/transmission measurements using the Ti:Sapphire, the reflected/transmitted beam can also be sent directly to a Si photodiode.

2.3.4 Sideband measurements

For sideband measurements, the reflected/transmitted NIR laser is sent to the SPEX/PMT along with any sidebands. A sideband spectrum (see Fig. 1.5, page 16) is measured by scanning the monochromator and measuring the PMT signal on an oscilloscope. The sideband signal appears only when the THz pulse is present. The laser line must be carefully avoided during measurements as it may damage the detector. For this reason, the SPEX must be used in sideband experiments instead of the Acton/ICCD.

A number of other measurements are made in sideband experiments, as listed

below.

1. Sideband Resonance Spectrum: The Ti:Sapphire frequency is scanned while always measuring a particular sideband. The monochromator must be scanned along with the laser, maintaining a fixed offset. (See Fig. 4.5, page 90)

2. Sideband Voltage Scan: The voltage applied to the sample is scanned while measuring the sideband signal. The Ti:sapphire frequency is fixed. (See Fig. 4.4, page 89)

3. Sideband Resonance Map: Sideband Voltage Scans at many Ti:sapphire frequencies are performed, producing a map. Again, the monochromator must be scanned along with the laser. (See Fig. 6.7, page 142)

4. NIR Power dependence: The sideband signal is measured for a series of NIR powers. (The NIR power must be measured after the AOM). (See Fig. 4.8, page 95)

5. FEL Power dependence: The sideband signal is measured for a series of THz powers. (See Fig. 6.8(b), page 144)

2.3.5 Reflectivity and Transmission

Reflectivity and transmission spectra were taken using both the Ti:Sapphire and the broadband sources (LEDs and lamp). Using the laser, spectra are obtained by scanning the laser and measuring the reflected or transmitted signal with a photodiode. Using a fast preamplifier (Matec model 254), the signal can be measured as a function of time, with a time resolution of ∼100 ns. This method can measure small (∼1%) changes in reflectivity/transmission. A sample oscilloscope trace of a reflected signal is displayed in Fig. 2.10(a) with the corresponding THz pulse in (b). The problem with these measurements is that jumps in the Ti:Sapphire frequency of ∼0.5 meV and jumps in the power yield mediocre spectra.

Reflectivity and transmission with the LED or lamp source is measured by sending the beam to either the SPEX/PMT or to the Acton/ICCD. The SPEX/PMT is typically used for measuring the linear reflectivity/transmission and gives very smooth spectra. For THz EO measurements, the signal can only be measured for 1-2 μs per pulse, making the signal level very important. The LEDs must be used, due to their higher power per nm, and the small monochromator/ICCD is used to reduce the time required for each spectrum. The ICCD is gated only during the 1-2 μs at the peak of the THz pulse, but leakthrough during the long ungated

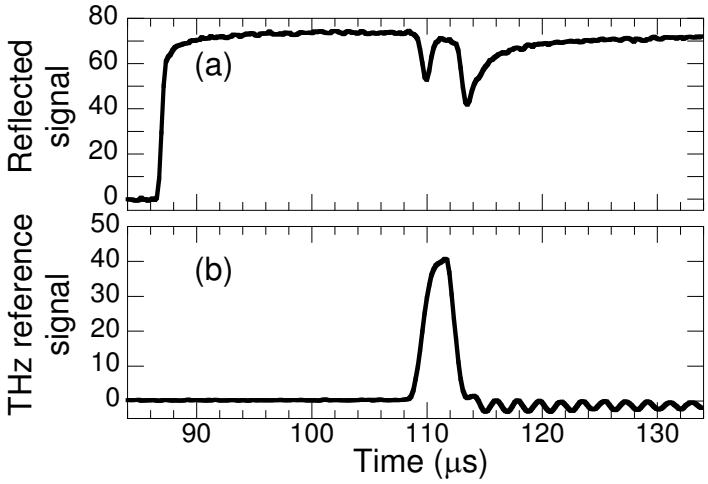

Figure 2.10: (a) Oscilloscope trace (averaged 12 times) of the reflected signal from Intest5 with Al coating. The NIR laser is at 1.4596 eV, just below the exciton absorption, and $\hbar\omega_{THz} = 10.4$ meV. (b) Corresponding trace of the THz reference detector.

periods necessitates pulsing of the LED. Usually, 100-200 averages are necessary to obtain a nice spectrum.

2.3.6 Photoluminescence

Photoluminescence (PL) is obtained by exciting the sample with the Ti:Sapphire at ∼770 nm or with a diode laser at ∼640 nm. In both cases, the excitation is below the AlGaAs barrier bandgap. The PL is collected and sent to either the SPEX/PMT or the Acton/ICCD.

2.3.7 FTIR and CV

FTIR absorption measurements were performed using the Bruker IFS66v FTIR with a 1.4 K Germanium bolometer. The sample was placed inside the detector cyrostat just before the bolometer element. More details on this type of FTIR measurement can be found in Jon William's dissertation.[42]

CV measurements were performed by applying a small ac voltage to the sample gates and measuring the quadrature component of the current. A dc voltage was also applied to deplete the sample. More details on CV measurements can be found in [42].

Chapter 3

THz field effects on exciton absorption

The effect of an electric field on QW interband absorption has been studied extensively. In the Quantum Confined Stark Effect (QCSE), a dc electric field in the growth direction shifts absorption lines to lower energies and induces some broadening.[25, 26] This effect is used in optoelectronic devices to modulate NIR light at frequencies up to ∼50 GHz.

At much higher frequencies, the effect is called the Optical Stark Effect. A strong "pump" field, typically below the band gap, "dresses" the QW states, which induces shifts in the linear absorption.[43, 44] When the pump field is near resonance, Autler-Townes splitting[45] and even Electromagnetically-Induced-Transparency

(EIT) have been observed.[46, 47] These experiments have used pump wavelengths from approximately 400 nm to 10 μm.

The effect of a THz electric field on QW interband absorption has been given a great deal of theoretical attention,[15, 16, 17, 18, 22, 23, 36, 37] but little experimental work has been reported. The effect of a strong in-plane THz field on exciton absorption was demonstrated and attributed to the dynamical Franz-Keldysh effect, but the effects were relatively small.[19]

In this chapter, the interband absorption spectra of QWs will be examined in the presence of a strong THz field polarized in the growth direction. Undoped square QWs are used, as in the above-mentioned experiments, to simplify the interband spectra and to prevent absorption of the pump field. The THz field couples two heavy hole exciton states and demonstrates the formation of THz-dressed states, manifested in part by Autler-Townes splitting of the exciton absorption. These experiments are unique for the following reasons:

1. A splitting is observed due to a THz QCSE.

2. The Rabi frequency, $2\mu E/\hbar$, can be a significant fraction of the pump frequency.

3. Dressed states are observed for large detunings of the pump frequency.

4. The pump field is quasi-CW.

The first sections of this chapter will discuss excitons in QWs and the basics of dressed states. Then, results on experiments in GaAs QWs will be presented, in which the THz QCSE is obscured by other, less understood effects. Finally, results in InGaAs will resolve this problem, and clearly demonstrate the formation of THz dressed exciton states.

3.1 Excitons in Quantum Wells

As stated in the introduction, the formation of excitons strongly modifies the interband absorption. In the effective mass approximation, the exciton states can be found by solving the following Schrödinger equation:

$$\left\{ \left[-\frac{\hbar^2}{2m_e^*}\frac{\partial^2}{\partial z_e^2} + V_e(z_e) \right] + \left[-\frac{\hbar^2}{2m_h^*}\frac{\partial^2}{\partial z_h^2} + V_h(z_h) \right] - \frac{\hbar^2}{2m_{eh}^*}\nabla_{\vec{\rho}}^2 - \frac{e^2}{4\pi\epsilon\sqrt{\rho^2 + (z_e - z_h)^2}} \right\} \psi(\vec{\rho}, z_e, z_h) = E\psi(\vec{\rho}, z_e, z_h). \tag{3.1}$$

In Eq. (3.1), the kinetic energy of the center of mass has been removed, leaving a dependence on the relative coordinate $\vec{\rho}$ in the QW plane and the z-coordinates. The effective masses m_e^* and m_h^* are for motion along z, while m_{eh}^* is the reduced mass for motion in the QW plane. Equation (3.1) is not separable, but if the confinement potential is more significant than the Coulomb potential, then a simple

variational wave function can be used.

$$\psi_{mn}^{(1s)}(\vec{\rho}, z_e, z_h) = \sqrt{\frac{2}{\pi}} \frac{1}{\lambda_{mn}} \varphi_{cm}(z_e)\varphi_{vn}(z_h) e^{-\frac{\rho}{\lambda_{mn}}}, \tag{3.2}$$

where φ_{cm} (φ_{vn}) is the mth (nth) growth-direction wavefunction in the conduction (valence) band calculated without the Coulomb interaction. As a function of ρ, $\psi_{mn}^{(1s)}$ is spherically symmetric with no nodes, making it a "1s" state. The variational parameter λ_{mn} must be calculated for each exciton state. $\psi_{mn}^{(1s)}$ will make a good wavefunction as long as the energy spacing due to confinement is much larger than the exciton binding energy, $\sim$8 meV. This is not necessarily satisfied for the QWs studied, but these wave functions are still useful for describing exciton states.

Figure 3.1(a) displays the conduction and valence subband energies in the 150 Å GaAs QW used for some of the experiments described in this chapter. Figure 3.1(b) represents the exciton state picture, in which each exciton consists of an electron from a conduction subband and a hole from a valence subband. The energies are modified by the binding energy of each exciton.

In principle, each level drawn in Fig. 3.1(b) should also have a series of levels above that represent exciton states of higher in-plane orbital angular momentum extending up to continuum states. All of these states have significantly weaker oscillator strength due to decreased electron-hole overlap and will largely be ig-

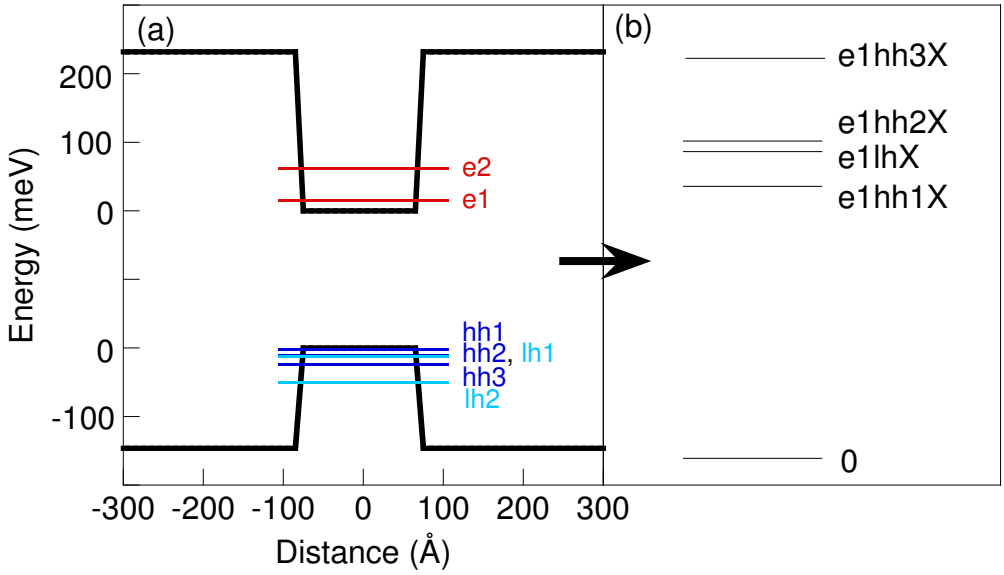

Figure 3.1: (a) Conduction band and Valence band of a 150 Å QW. The lines represent the bottoms of the conduction subbands (red), heavy hole subbands (dark blue), and light hole subbands (light blue). (b) Exciton state picture.

nored. The in-plane center of mass momentum is also neglected, which would lead to subbands instead of discrete states. This simplification is justified as NIR light will only interact with excitons with near-zero center of mass momentum due to small photon momentum. Figure 3.2 displays the reflectivity spectrum of V5, the 150 Å GaAs QW sample, demonstrating the discrete absorption lines.

3.2 Dressed States

The exciton states described above are no longer stationary states in the presence of an intense electromagnetic field. For low fields, a perturbative approach to

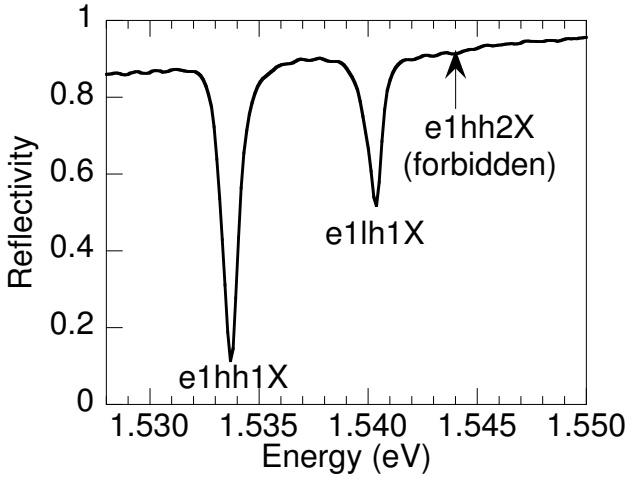

Figure 3.2: Reflectivity of sample V5 at 13 K using white light. The approximate position of e1hh2X was determined by applying a dc electric field.

the dipole response of the system is appropriate, and the unperturbed states still represent the system well. When the Rabi energy of a transition, $\hbar\Omega = 2\mu E$, is comparable to the linewidth, perturbative approaches break down. (μ is the electric dipole moment, and E is the electric field amplitude.) In this case, the most general solution can be obtained using Floquet theory.[48] For near-resonant fields in which $\Omega \ll \omega$, where ω is the drive frequency, the rotating wave approximation (RWA) can be made, leading to the Rabi solution of the Schrödinger Equation.

In the Rabi solution, two states are considered, the ground state a, and the excited state b. In the presence of the applied field, the time-dependent wavefunction can be written as

$$\psi(\vec{r},t) = C_a(t)u_a(\vec{r})e^{-i\omega_a t} + C_b(t)u_b(\vec{r})e^{-i\omega_b t}, \tag{3.3}$$

where u_a (u_b) is the unperturbed ground (excited) state wavefunction with energy $\hbar\omega_a$ ($\hbar\omega_b$). (This treatment follows that found in Ref. [49]) When expression (3.3) is plugged into the Schrödinger equation, the RWA is made, and the time-dependent coefficients are solved for, we obtain

$$C_a(t) = e^{(1/2)i\Delta t}\left(A_+ e^{-(1/2)i\Omega' t} + A_- e^{(1/2)i\Omega' t}\right), \tag{3.4}$$

$$C_b(t) = e^{(-1/2)i\Delta t}\left(\frac{\Delta-\Omega'}{\Omega^*}A_+ e^{-(1/2)i\Omega' t} + \frac{\Delta+\Omega'}{\Omega^*}A_- e^{(1/2)i\Omega' t}\right). \tag{3.5}$$

We have introduced the generalized Rabi frequency

$$\Omega' = \sqrt{|\Omega|^2 + \Delta^2}, \tag{3.6}$$

and the detuning

$$\Delta = \omega - \omega_{ba}, \tag{3.7}$$

where $\omega_{ba} = \omega_b - \omega_a$. The constants of integration, A_+ and A_-, are determined by initial conditions. According to this solution, the wavefunctions pick up additional frequency components. $C_a(t)$ contains frequencies $-\frac{1}{2}(\Delta \pm \Omega')$ and $C_b(t)$ contains frequencies $\frac{1}{2}(\Delta \pm \Omega')$. When these levels are probed with a weak field, the system should respond at the unperturbed eigenstate frequencies, ω_a and ω_b, plus these additional frequencies. The unperturbed eigenstates are in this way "dressed" by the strong field. The dressed frequencies for the ground state should be at

$$\omega_\pm = \omega_a - \frac{1}{2}\left(\Delta \mp \Omega'\right). \tag{3.8}$$

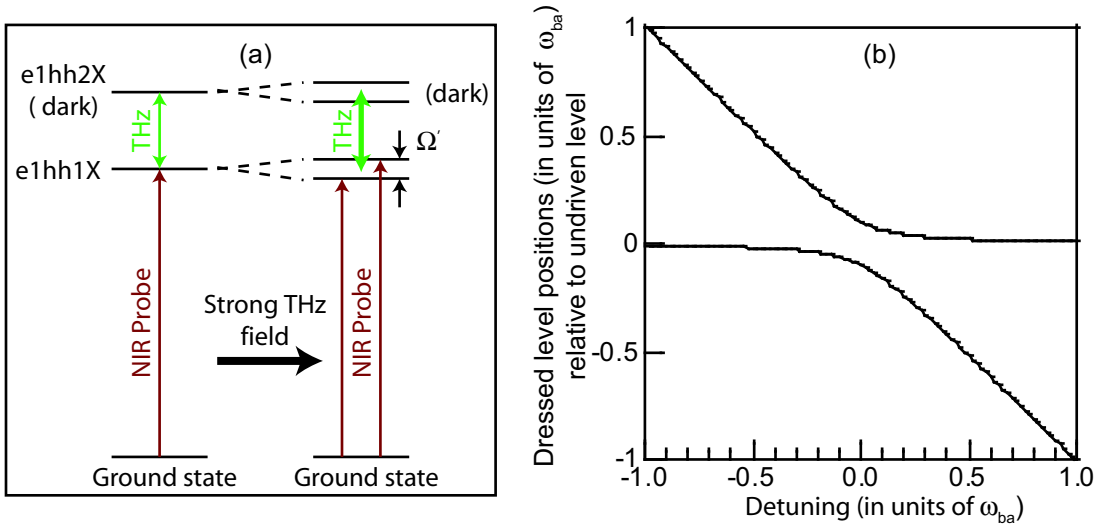

Figure 3.3: (a) Exciton level splitting diagram. Transitions from the ground state to e1hh2X are optically forbidden, so only e1hh1X is probed with the NIR beam. (b) Dressed level positions as a function of detuning calculated using Eq. (3.8) with $\Omega/\omega_{ba} = 0.2$.

The situation in the undoped QW may seem quite different from this simple two-level model, but a number of reasonable approximations make the model more applicable. We can limit the relevant states in the square QW to the ground state, e1hh1X, and e1hh2X. This assumes that other exciton states will couple only very weakly to e1hh1X. Higher exciton states are sufficiently far away that transitions from e1hh1X are far off-resonance and/or have much weaker oscillator strengths. Since heavy hole-light hole transitions are forbidden in the absence of valence band mixing, e1lh1X can also be ignored. In this approximation, the strong THz field will couple only to the e1hh1X-e1hh2X transition, and a weak NIR beam will probe the exciton states. The THz field does not drive any real transitions in the

absence of the probe, but the exciton states should still be dressed.

Figure 3.3(a) shows the expected splitting of the e1hh1X exciton when the e1hh1X-e1hh2X transition is driven on resonance by the strong THz field. Figure 3.3(b) displays the calculated dressed level positions from the Rabi model as a function of detuning. Off-resonance, the splitting is asymmetric, and the oscillator strength of the level near the unperturbed exciton level dominates. The presence of this second, weaker level can be thought of as e1hh2X becoming optically allowed as it is coupled to e1hh1X. Indeed, for very low drive frequencies, the weaker level appears close to where the e1hh2X is expected. As the drive frequency increases, the level redshifts. This second level is strongest when e1hh1X and e1hh2X are strongly coupled near resonance, and there is an anticrossing of the levels.

The observation of this splitting by probing absorption from a third level was first observed and explained in a molecular system by Autler and Townes.[2] Vibrational states of carbonyl sulfide (OCS) were driven with a strong rf field and probed by measuring the absorption to or from another state with a weak microwave probe. This type of splitting has also been observed in CuCl[45] and GaAs QWs[47] using an interband pump. Theoretical studies have predicted Autler-Townes splitting in QWs using an intersubband pump coupling electron levels[38] and heavy-hole levels[32].

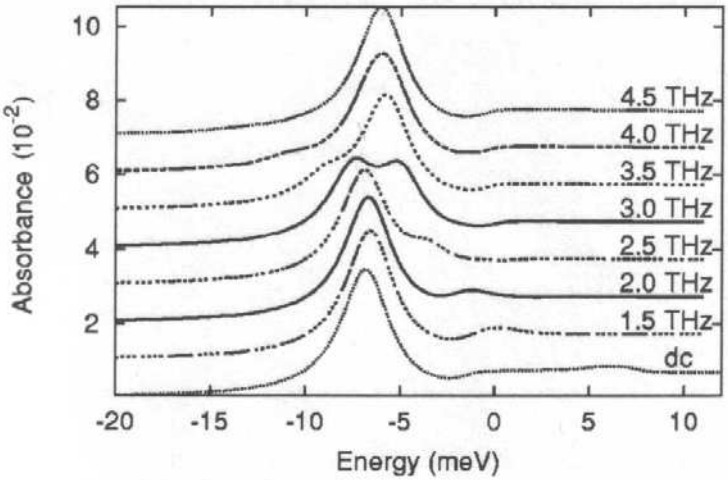

Figure 3.4: Calculated interband absorption of a THz driven 150 Å GaAs QW reprinted with permission from Ref. [32] (Copyright (2000) by the American Physical Society) at a field of 10 kV/cm. The THz field is on resonance with the e1hh1X-e1hh2X transition at 3.0 THz, showing the e1hh1X line splitting.

Figure 3.4 displays the interband absorption spectrum of a 150 Å GaAs QW driven by a 10 kV/cm THz field as calculated by Maslov *et. al.* in Ref. [32]. The splitting occurred when the THz frequency was near the e1hh1X-e1hh2X transition at 3.0 THz. The anticrossing behavior, similar to that found in Fig. 3.3(b) is also visible. These calculations are particularly relevant to the results in GaAs QWs that follow.

3.3 Results in GaAs QWs

In this section, the effect of a THz field on the interband absorption of sample V5 will be presented. The complete structure of this sample is found in Appendix

C, and it is also illustrated in Fig. 2.1(d), page 21. The sample consists of 3 undoped 150 Å QWs separated by 300 Å $Al_{0.3}Ga_{0.7}As$ barriers. These wells are in-between two doped 80 Å gate QWs used for applying a dc field to the wells. A 30 period DBR is behind all of these wells to reflect the NIR beam which would otherwise be absorbed in the semi-insulating GaAs substrate. The active 150 Å QWs are placed close to a multiple of $\lambda_{NIR}/2$ from both the sample surface and the DBR. This forms a low-Q cavity in which the electric field at the active QWs is enhanced along with the absorption. The reflectivity of V5 at 13 K and zero bias is shown in Fig. 3.5. (Figure 3.2 zooms in on the exciton lines in this spectrum.) The stopband of the DBR from 1.48 to 1.58 eV is apparent as well as the strong exciton lines. There also appears to be a cavity mode centered near the e1hh1X line as expected.

Changes in reflectivity were first measured on V5 with sapphire pressed onto the frontside as shown in Fig. 2.1(b), page 21. Figure 3.6 displays changes in the reflectivity for a series of incident THz powers at $\hbar\omega_{THz} = 10.4$ meV and $\hbar\omega_{THz} = 6.4$ meV. As the THz power increased, there was a significant redshift and broadening as well as a decrease in the peak absorption. One can imagine some of this broadening being due to a splitting that is not resolved. However, an additional source of broadening is necessary to explain the data. The redshift could be similar to that induced by a dc electric field in the QCSE as shown in

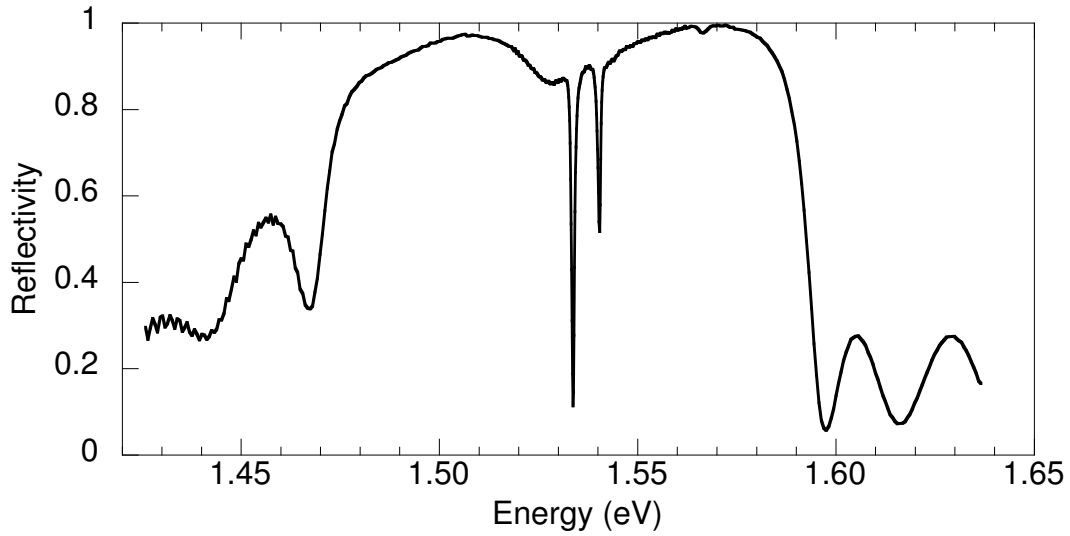

Figure 3.5: Reflectivity of sample V5 at 13 K using white light.

Fig. 4.2(c). Another point is that the e1hh1X-e1hh2X resonance should be at about 10.3 meV, but there was no well-defined difference between the changes in reflectivity at $\hbar\omega_{THz} = 10.4$ meV and $\hbar\omega_{THz} = 6.4$ meV or at any other THz frequency measured.

On first inspection, one might suspect that these changes were due primarily to heating. However, the increase in lattice temperature required to broaden the excitons so much would redshift the exciton lines far more than observed. Time resolved measurements in Fig. 3.7 demonstrated that there was a change in reflectivity that persisted after the THz pulse. We attribute this to heating. However, this persistent effect was relatively small compared to the effect at the

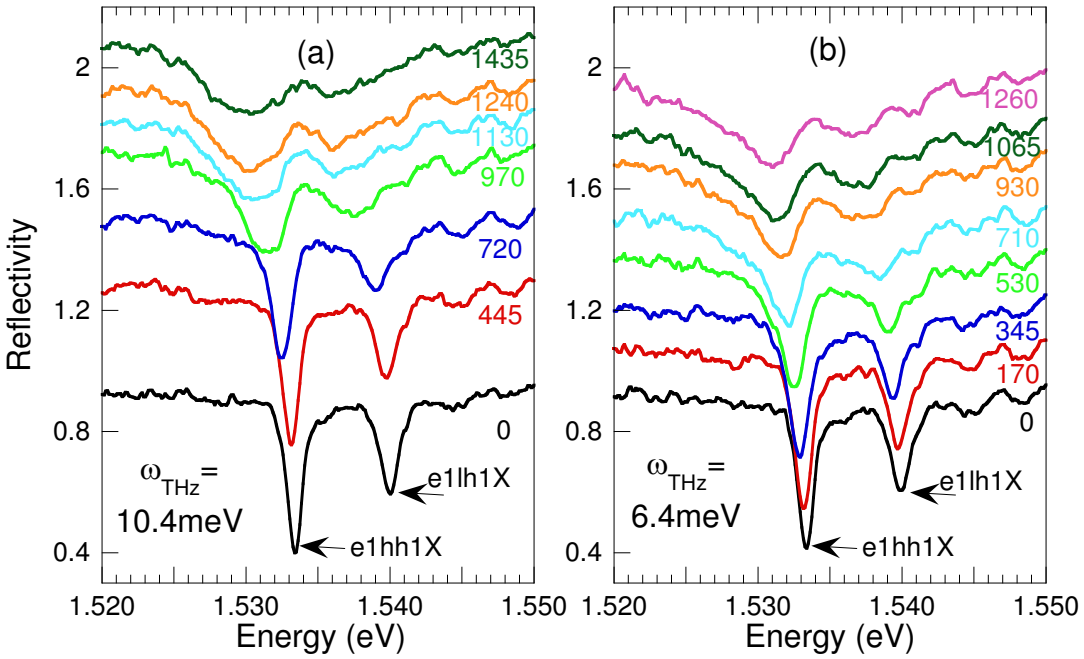

Figure 3.6: Reflectivity of V5 with sapphire at 20 K using an LED at (a) $\hbar\omega_{THz} =$ 10.4 meV (2.5 THz) and (b) $\hbar\omega_{THz} = 6.4$ meV (1.55 THz). The spectra are offset and labelled according to the approximate incident THz power in Watts.

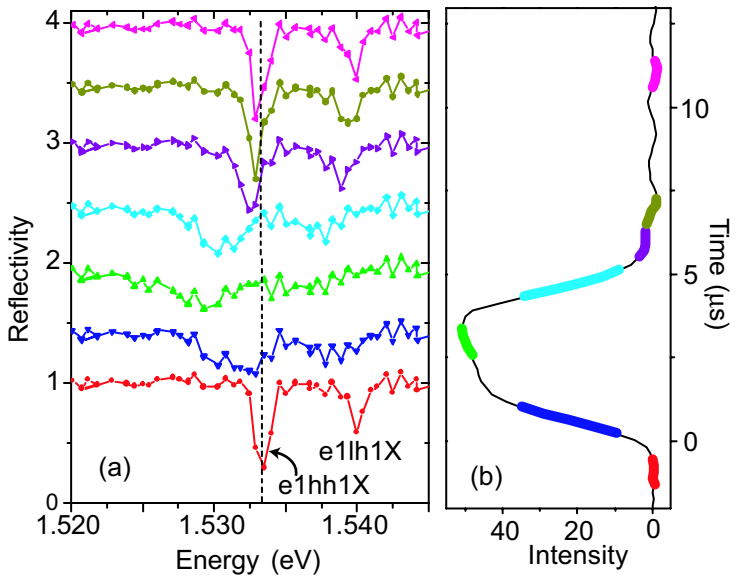

Figure 3.7: (a) Reflectivity of V5 with Sapphire at different times along the THz pulse. The reflectivity spectra are offset and color-coded according to the time intervals of the THz pulse, shown in (b). The dashed line marks the e1hh1X position before the THz pulse.

peak of the THz pulse.

One possible explanation for these strange results is that a significant in-plane field may have been present. While the incident THz field was almost completely in growth direction, the dielectric waveguide modes in the sample have significant in-plane components, and gaps between the sample and sapphire can also result in in-plane fields (see Section 2.1.3). In-plane fields have been shown to ionize excitons in some situations,[24] and could cause broadening. Figure 3.8 displays the results of an experiment measuring changes in the reflectivity of V5 (with no sapphire) with the THz beam incident normal to the sample, giving a strong

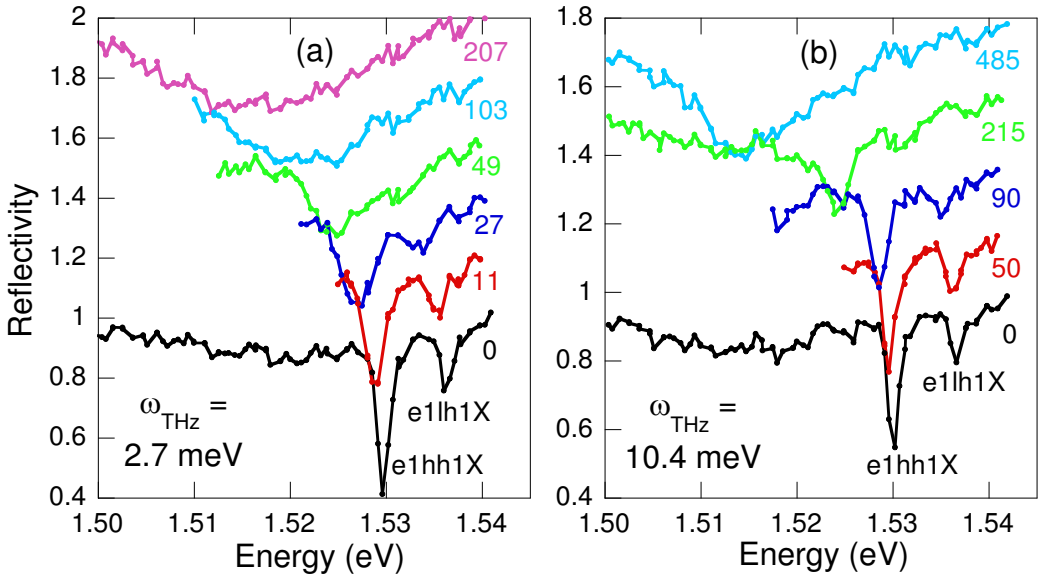

Figure 3.8: Reflectivity of V5 at 12 K at a series of in-plane THz fields, offset and labelled by THz intensity in kW/cm^2. The THz frequency was (a) 2.7 meV (0.66 THz) and (b) 10.4 meV (2.5 THz), and the NIR laser intensity was ∼6 W/cm^2.

in-plane field.

The effect of an in-plane THz field was quite dramatic. The exciton lines appeared to redshift and broaden until there was only a very broad resonance well below the undriven exciton lines. At similar intensities, the effect was much greater at the lower frequency, $\hbar\omega_{THz} = 2.7$ meV. These results seem very different from those in Ref. [19], in which changes in transmission of 80 Å $In_{0.2}Ga_{0.8}As$ QWs due to an in-plane THz field were measured. Only a little broadening was observed, along with small shifts, which tended to be blueshifts at high THz intensity. These changes were attributed to the dynamic Franz-Keldysh effect, which also predicts

increased subgap absorption. It is possible that the results in Fig. 3.8 were in part due to this subgap absorption. The broad resonance appeared to move toward the cavity mode, as if any increased absorption there was effectively "amplified." Whatever the explanation might be, however, it is clear that even a small in-plane THz field can have a significant effect on the reflectivity of V5.

This prompted a different THz-coupling strategy, in which a piece of ITO-coated glass was pressed onto sample frontside instead of sapphire. The ITO is transparent for NIR light, but is conductive for THz fields. In principle, this should eliminate in-plane THz fields at the surface. The results at $\hbar\omega_{THz} = 6.4$ meV and $\hbar\omega_{THz} = 10.4$ meV are displayed in Fig. 3.9. The results do not appear very different from those in Fig. 3.6. The undriven reflectivity looked somewhat different as the cavity mode seemed to be affected by the presence of the ITO. The changes in reflectivity with THz power seemed to also be affected by the altered cavity mode, making a comparison difficult. It may not be too surprising that the results were qualitatively similar. As discussed in Chapter 2, a gap greater than several 100 nm between the sample surface and the ITO will likely result in significant in-plane THz fields. Gaps of this thickness are certainly present when ITO is pressed onto the sample based on the interference fringes observed.

The results presented in the section on V5 are still not well understood. There are a number of complications that make the results hard to understand, including

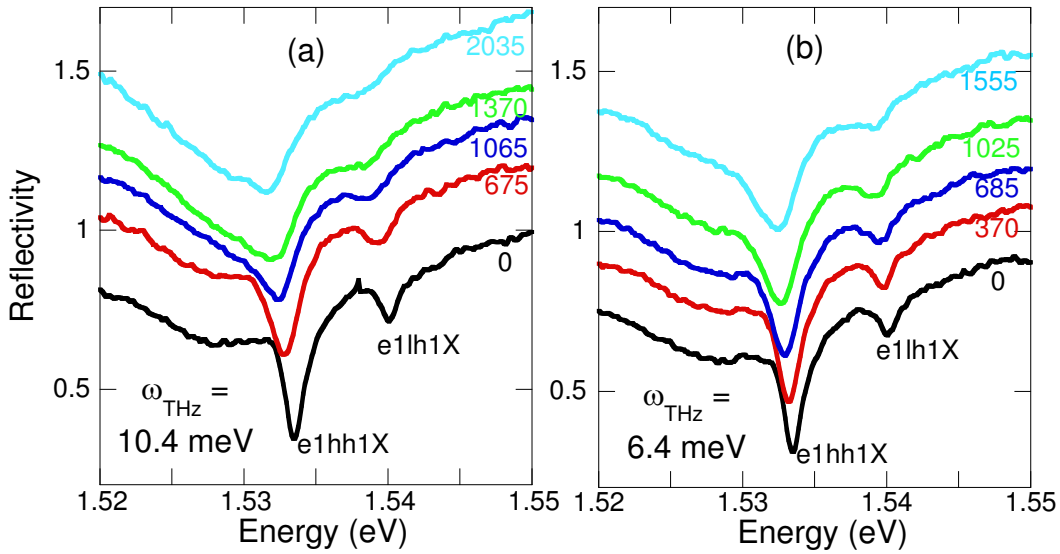

Figure 3.9: Reflectivity of V5 with ITO at 11 K at a series of THz fields, offset and labelled by THz power in Watts. The THz frequency was (a) 10.4 meV (2.5 THz) and (b) 6.4 meV (1.55 THz), and the reflectivity was measured using an LED.

the DBR/cavity modes, the presence of e1lh1X, uncertainty in the THz field strength/polarization, and possible charge in the wells from the gate QWs. In the next section, experiments on $In_{0.06}Ga_{0.94}As$ QWs will be presented which eliminate many of these complications.

3.4 Results in InGaAs QWs

Several $In_{0.06}Ga_{0.94}As$ QW samples were grown (by Chad Wang) and examined, each having the structure shown in Fig. 2.1(c), Page 21 (see Appendix C for complete structure), with varying QW widths and Indium concentration. The

sample named Intest5 will be the focus of this section. Intest5 consists of 10 undoped 143 Å $In_{0.06}Ga_{0.94}As$ QWs separated by 300 Å $Al_{0.3}Ga_{0.7}As$ barriers. This sample structure has no need of a DBR since the GaAs substrate is transparent to NIR light resonant with the QW excitons. It also has no gate QWs, preventing any inadvertent doping. Figure 3.10 displays the transmission of the sample, illustrating the simplicity of the interband spectrum. The strong absorption at 1.461 eV is due to e1hh1X, which has a significantly larger linewidth than in V5. e1hh2X is expected to be 13.5 meV above e1hh1X,[1] but is optically forbidden. The light hole exciton is gone, apparently shifted out of the way due to strain.

The transmission of this sample in the presence of a THz field was first measured with ITO pressed onto the frontside, as displayed in Fig. 3.10 (dashed line). There was almost no effect on the exciton line. The increased absorption just below the GaAs band edge due to the dynamic Franz-Keldysh effect is apparent, indicating a significant THz field in the substrate. The likely explanation is that the THz field at the surface was weak due to a gap between the sample surface and the ITO as discussed in Chapter 2. Certainly, this InGaAs sample behaves very differently from V5 in the presence of a THz field. The reason is uncertain, but one explanation is that cavity effects in V5 enhance and modify the changes

[1]Energies were calculated in the same manner as in Section 4.4.1 for GaAs QWs but 0.34 was used for the heavy hole effective mass.[4] The energies were relatively insensitive to the barrier height, so the values for GaAs QWs were used.

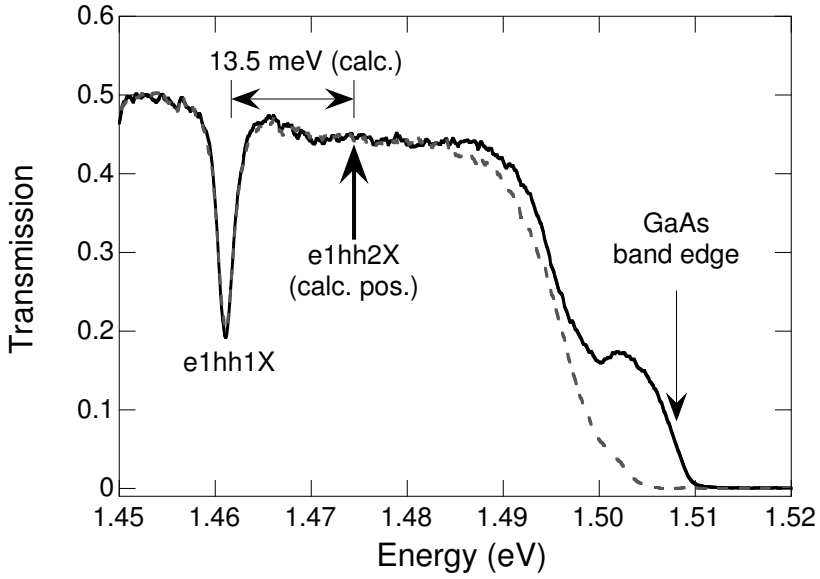

Figure 3.10: Transmission spectrum of Intest5 with ITO at 10.5 K using an LED. The dashed line displays the transmission in the presence of a 1.4 kW THz field at $\hbar\omega_{THz} = 10.4$ meV. The calculated position of e1hh2X is indicated by an arrow.

in reflectivity.

In an attempt to improve the THz field in the QW layers, about 100 nm of Aluminum was evaporated onto the sample surface. Having no gap between the Al and the sample surface as well as the high conductivity of Al produces a much better boundary condition at the surface. The NIR light coupled into the sample through the backside, interacted with the QWs and was reflected off of the Al, as shown in Fig. 2.1(a), page 21. The sample was also rotated 15° with respect to the axis perpendicular to both the NIR and THz beams, as this increased the changes in reflectivity. The results as shown in Fig. 3.11 were quite impressive.

Near resonance at $\hbar\omega_{THz} = 14.1$ meV, there was a clear splitting of the exciton line, which increased as a function of power. Below the resonance, at $\hbar\omega_{THz} = 10.4$ meV, a weaker absorption line appeared above the undriven exciton line. At $\hbar\omega_{THz} = 6.4$ meV, the weaker absorption line was nearly buried in the noise. While just above the resonance, at $\hbar\omega_{THz} = 16.1$ meV, a weaker absorption line appeared below the undriven exciton line. These results are a clear manifestation of Autler-Townes splitting and THz-dressed states.

Figure 3.12 displays the reflectivity of Intest5 at many more THz frequencies, all at similar THz powers. The power was relatively low ($\sim$550W) because it was the highest power available at $\hbar\omega_{THz} = 15.5$ and 16.1 meV, where the FEL is not typically used. Actually, the THz intensity should be held constant for this comparison instead of the THz power. The THz intensity outside the sample has been measured for many frequencies, but it does not represent the intensity in the QW layers. This is particularly true because the reflectivity spectra were obtained with the NIR beam several mm away from the sample edge, where the reflectivity changes were greatest. This far into the sample, the free space intensity distribution should be less significant than the guided mode distribution. Therefore, the approximation was made that neither the power coupled into the sample nor the intensity distribution in the sample depended too much on frequency.

Figure 3.12 shows much of the behavior expected from the Rabi solution and

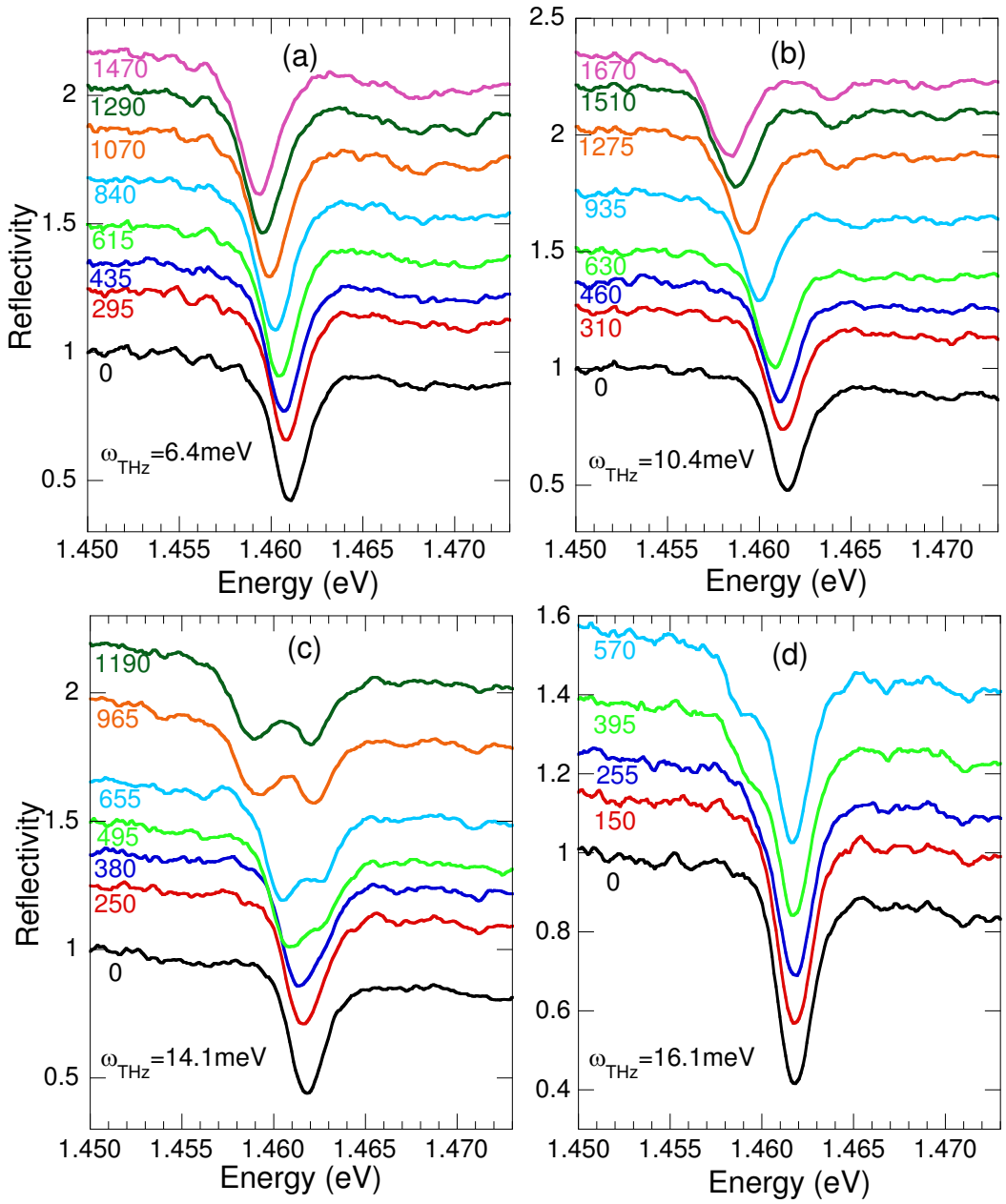

Figure 3.11: Reflectivity spectra of Intest5 with Al at 10 K for a series of THz powers at $\hbar\omega_{THz}$ = (a) 6.4 meV, (b) 10.4 meV, (c) 14.1 meV, and (d) 16.1 meV. The spectra were taken using an LED and were normalized by the reflected spectrum of a gold mirror. They are offset and labelled according to the THz power (in Watts).

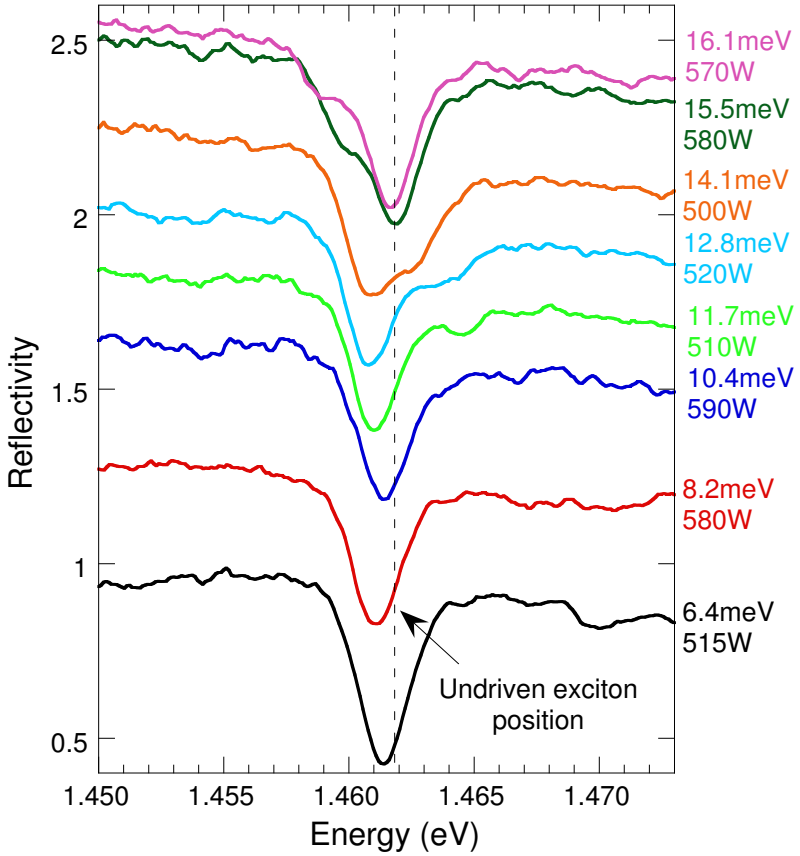

Figure 3.12: Reflectivity spectra of Intest5 at ∼10.5 K using an LED, offset and labelled according to the THz frequency. The THz power was ∼550 W for each spectrum. Several spectra are slightly shifted to correct for small shifts (< 0.25 meV) in the undriven e1hh1X position.

from the calculations in Ref. [32] (see Fig. 3.4), including an anticrossing near resonance. The positions of the two absorption lines are not very clear in Fig. 3.12, particularly off-resonance. The positions were obtained by fitting the spectra to two Lorentzians. This was performed by first correcting for the downward slope of the spectra due to the GaAs band edge and continuum absorption by dividing by the appropriate linear function. Then, the absorption was obtained by taking the negative natural log of the reflectivity. These absorption spectra are displayed in Fig. 3.13 for $\hbar\omega_{THz} = 11.7$ meV to 16.1 meV (black lines). The fits (red lines) to two Lorentzians match up quite nicely.

This fitting procedure did not work well for the spectra at $\hbar\omega_{THz} = 6.4$ meV to 10.4 meV because the weaker absorption line was almost lost in the noise. Even ignoring the noise, it is very difficult to fit a spectrum to two Lorentzians when the actual spectrum contains continuum absorption and other features. One way to reduce this problem is to look at the differential spectrum. If the reflectivity with (without) the THz field is called $R(\omega)$ ($R_0(\omega)$), the differential signal is

$$d(\omega) = \frac{R(\omega) - R_0(\omega)}{R_0(\omega)}. \tag{3.9}$$

This differential reflectivity is plotted in Fig. 3.14 (blue lines) along with the reflectivity with the FEL blocked (black lines) for $\hbar\omega_{THz} = 10.4$ meV to 6.4 meV. The large feature in the differential reflectivity near the undriven exciton line

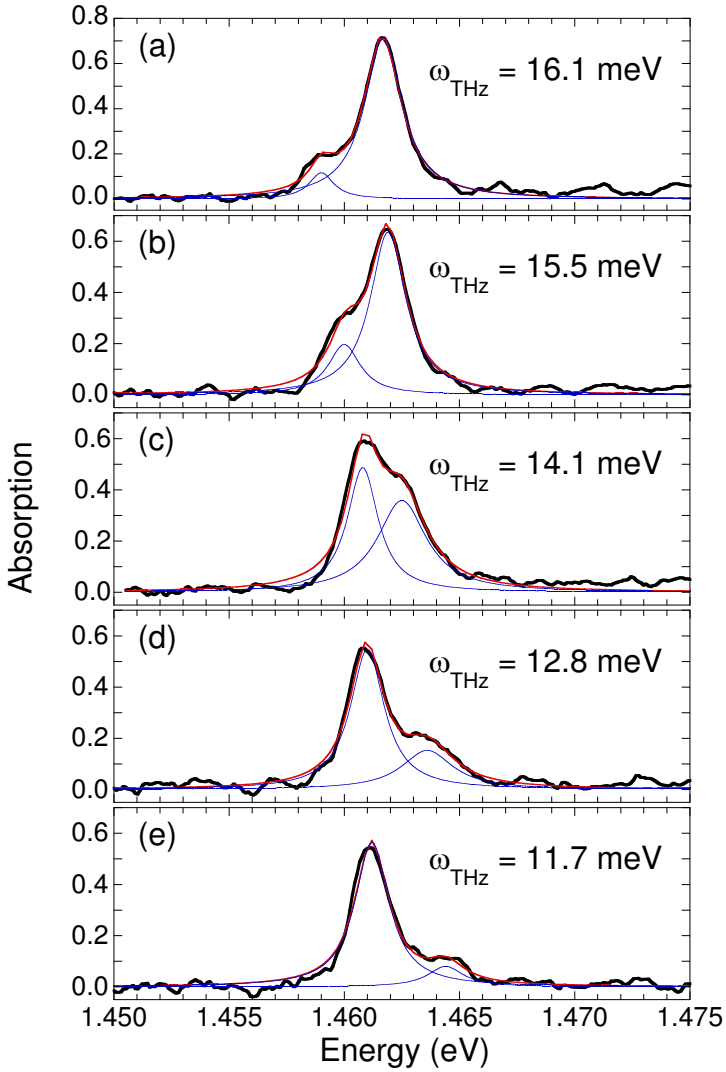

Figure 3.13: Absorption spectra and fits for $\hbar\omega_{THz} = 16.1$ meV to 11.7 meV, (a) to (e). The black lines represent the absorption obtained from the reflectivity spectra in Fig. 3.12 by correcting for the downward slope and taking the negative natural log. The red curves are fits to two Lorentzians, and the the blue curves are the individual Lorentzians.

represents a redshift, and there is also a small negative dip above the exciton line (indicated by an arrow) for $\hbar\omega_{THz} = 10.4$ meV and 8.2 meV that is due to the 2nd, weaker absorption line.

The differential spectra cannot be fit directly, but they can be applied to the Lorentzian fits to the undriven exciton lines shown in Fig. 3.14 (red lines). From Eq. (3.9), $R(\omega) = R_0(\omega) + d(\omega)R_0(\omega)$. Replacing $R_0(\omega)$ with $R_0^{fit}(\omega)$ ensures that the background is flat and gets rid of noise common to R and R_0. This procedure may seem a little convoluted, but it is essentially a two-step method of fitting the differential spectra. The resulting absorption spectra for $\hbar\omega_{THz} = 10.4$ meV and 8.2 meV are displayed in Fig. 3.15 along with fits to two Lorentzians. The agreement is quite good. The reflectivity for $\hbar\omega_{THz} = 6.4$ meV was fit to one Lorentzian since a second absorption line was not at all visible in the differential reflectivity at this low THz power.

When the absorption line positions obtained from the fits are plotted as a function of THz frequency, the anticrossing behavior is seen more clearly, as shown in Fig. 3.16. The absorption strength is represented on a greyscale for each marker. The uncertainty in the positions, determined by the fits, is smaller than the dots except at $\hbar\omega_{THz} = 8.2$ meV (upper dot). The two absorption lines can be considered e1hh1X and e1hh2X "dressed" by the strong THz field. On resonance, the two were strongly-coupled, so the absorption strength of the two was equal

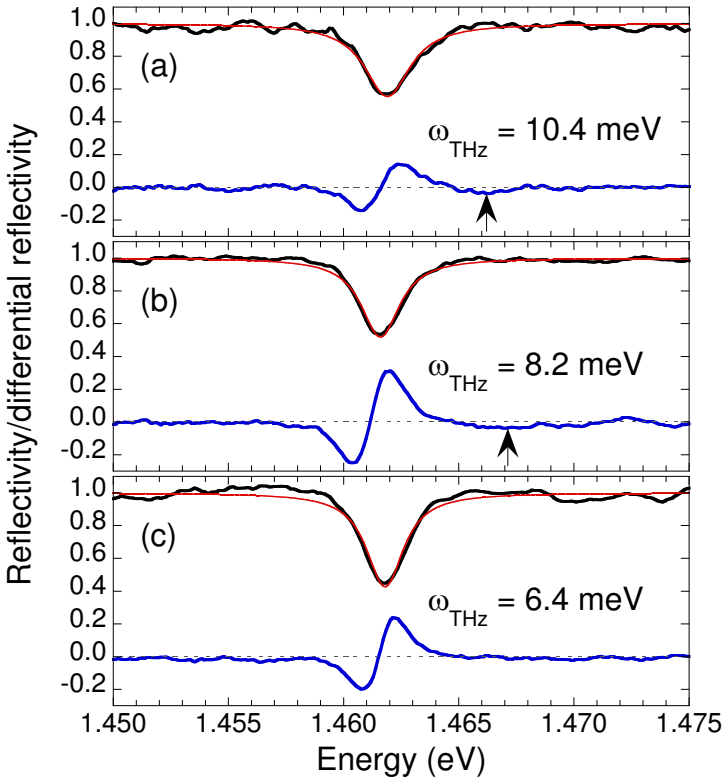

Figure 3.14: Reflectivity spectra with the FEL blocked (black lines) and differential reflectivity spectra (blue lines) for $\hbar\omega_{THz} = 10.4$ meV to 6.4 meV, (a) to (c). The differential spectra are taken by subtracting the blocked spectra from the spectra in Fig. 3.12 and then dividing by the blocked spectra. Lorentian fits to the blocked spectra are also displayed (red lines). The dashed black line at zero is a reference for the differential reflectivity. The arrows indicate the small negative dip above the exciton line.

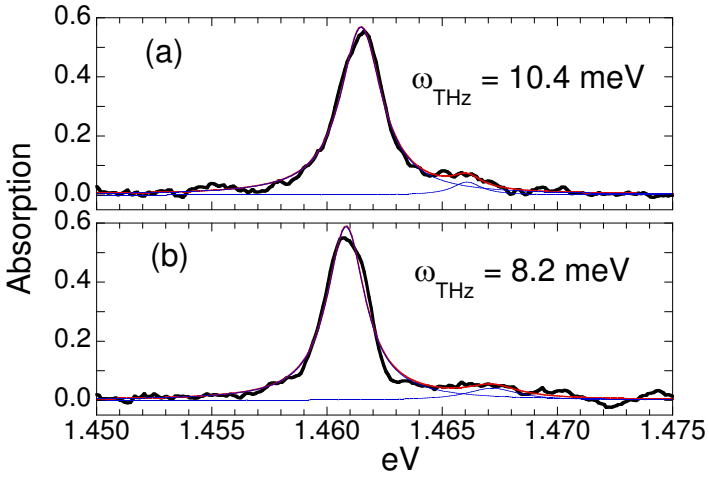

Figure 3.15: Absorption spectra and fits for $\hbar\omega_{THz} = 10.4$ meV and 8.2 meV, (a) and (b). The black lines represent the absorption obtained by applying the differential reflectivity to the fit of the undriven exciton spectrum as explained in the text. The red curves are fits to two Lorentzians, and the the blue curves are the individual Lorentzians.

and there was an anti-crossing. Off-resonance, one of the lines was weaker and approached the e1hh2X energy at low THz frequencies. The lines display the expected positions of the dressed states from the Rabi model, given by

$$E_{\pm} = E_0 - \frac{1}{2}\hbar\left(\Delta \mp \sqrt{\Delta^2 + \Omega^2}\right), \tag{3.10}$$

where E_0 is the undriven energy of e1hh1X, E_{THz} is the THz electric field, and $\Omega = (2\mu E_{THz}/\hbar)$ is the Rabi frequency. Equation (3.10) was evaluated in Fig. 3.16 using $E_{21} = 14.2$ meV (e1hh1X-e1hh2X energy spacing) and $\hbar\Omega = 2$ meV. The fit worked well despite the approximations made. The aspect of Figs. 3.12 and 3.16 that did not fit was the lack of a blueshift with respect to the undriven exciton

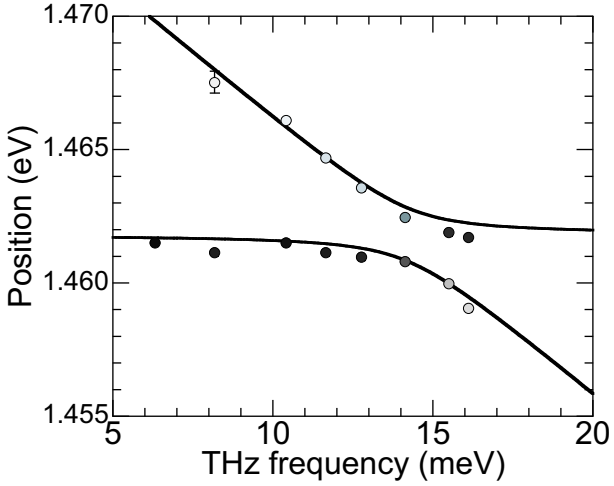

Figure 3.16: Absorption line positions vs. THz frequency as taken from the spectra in Fig. 3.12 showing the anticrossing behavior. The positions were obtained by fitting to two Lorentzians. The absorption strength for each point is represented on a grey scale. A completely black dot indicates the absorption strength was the same as the undriven absorption strength, while a white dot indicates very small absorption. Uncertainty in the positions is smaller than the dots except at $\hbar\omega_{THz} = 8.2$ meV (upper). The lines are plots of $E_{\pm}$ taken from Eq. (3.10), with the parameters $E_{21} = 14.2$ meV and $\hbar\Omega = 2$ meV.

energy of the stronger absorption line at $\hbar\omega_{THz} = 15.5$ and 16.1 meV. This was due to an overall redshift of the spectra.

For each THz frequency in Fig. 3.11, there was an overall redshift of the absorption as a function of power. In Fig. 3.17(a) the two absorption line positions for $\hbar\omega_{THz} = 14.1$ meV are plotted as a function of power. For powers less than $\sim$600 W, one line moved up and one down, but past that point the upper line started to shift down. From Eq. (3.10), one level should always move up and the other down as a function of power. Equation (3.10) also predicts that the

splitting on resonance should be proportional to E_{THz} or the square root of the power, which does not seem to be the case in Fig. 3.17(b).

There are several possible explanations for why these results did not fit Eq. 3.10. One possibility is that this simple Rabi model is not adequate for this system. For instance, if the Rabi frequency were becoming comparable to the drive frequency, the RWA used in the Rabi solution would be invalid. Equating the splitting at the highest power in Fig. 3.11(c) with the Rabi energy gives $\Omega/\omega \approx 0.2$. This ratio does not seem large enough to make the RWA invalid, but even if the Rabi energy were getting too high, the results at lower THz power could still not be explained. The simple Rabi model also does not take into account coupling to higher exciton states. Sophisticated calculations using the semiconductor Bloch equations were performed by Maslov that did not use the RWA for the THz field and that included higher exciton states.[32] This model also predicted a linear dependence of the splitting on E_{THz} with no redshift.

Heating effects may explain the redshift. These were examined by measuring the reflectivity of Intest5 several μs after the THz pulse. As shown in Fig. 3.18(a), the absorption line was slightly redshifted just after the THz pulse. This effect persisted to a lesser extent up until the next THz pulse, $\sim$0.67 s later. This persistent effect must have been due to an increase in the lattice temperature. Fig. 3.18(b) plots the persistent absorption line shift as a function of THz power

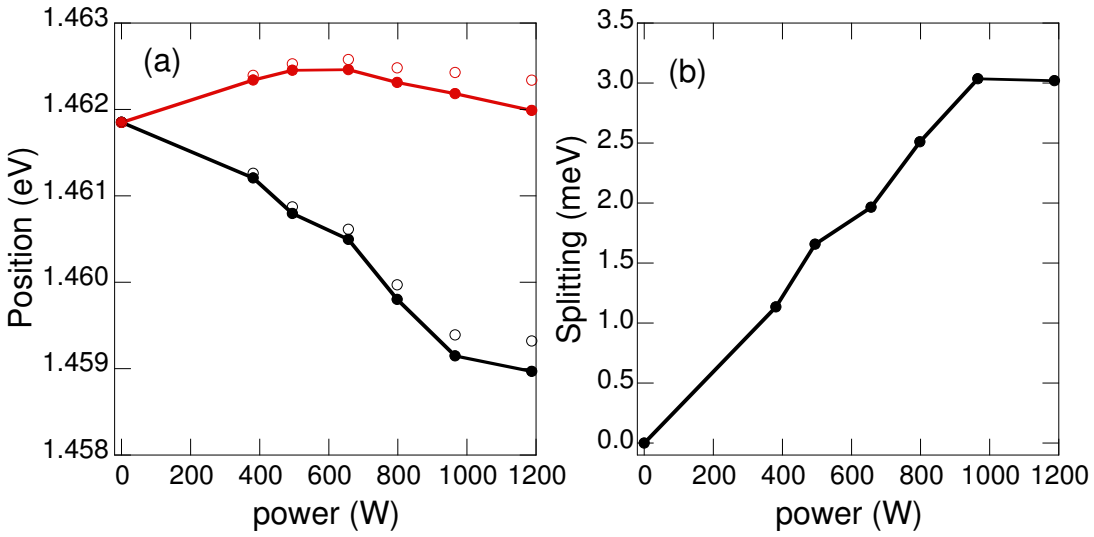

Figure 3.17: (a) Positions of the absorption lines of Intest5 as a function of THz power at $\hbar\omega_{THz} = 14.1$ meV. The positions were determined by fitting the spectra in Fig. 3.11(c) to two Lorentzians. The open circles display the absorption lines corrected for shifts due to heating effects as shown in Fig. 3.18, while the solid circles do not. (b) Splitting of the absorption lines vs. THz power.

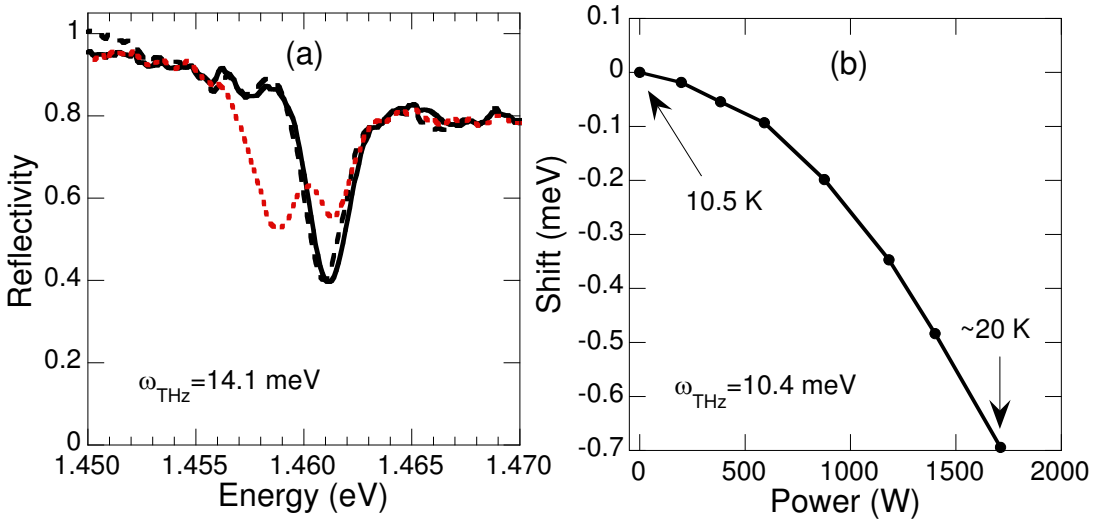

Figure 3.18: (a) Reflectivity of Intest5 with the THz pulse blocked (solid line), a few μs after the pulse (dashed, black line), and at the peak of the THz pulse (dashed, red line). The sample was at 10.5 K, and $\hbar\omega_{THz} = 14.1$ meV. (b) Persistent shift in the absorption line as a function of THz power for $\hbar\omega_{THz} = 10.4$ meV.

for $\hbar\omega_{THz} = 10.4$ meV. At 1.7 kW, the shift is consistent with an increase in lattice temperature from 10.5 K to ∼20 K, based on measurements of the exciton position as a function of temperature. Similar measurements were done at $\hbar\omega_{THz} = 6.4$ and 14.1 meV, which matched up well with these results. The quadratic dependence on power was due to the quadratic band gap changes as a function of temperature. Interestingly, when ITO was pressed onto Intest5, this heating effect was not observed, implying that the heating is more sensitive to the THz intensity close to the QWs or that the heating is due to the Al.

In principle, each reflectivity spectrum in Fig. 3.11 could be corrected for the

shift due to heating. In Fig. 3.17(a), the corrected absorption line positions at $\hbar\omega_{THz} = 14.1$ meV are plotted as open circles. The corrections do not significantly change the positions, however, particularly at lower powers. The spectra in Fig. 3.11 would change little if corrected for heating shifts, and an overall redshift of the absorption would still be present. All of the redshift may still have been due to heating if the lattice temperature during the THz pulse was significantly higher than it was a few μs after the pulse. This could have occurred if the THz beam heated up the Al layer, giving a higher temperature for the QWs than for the substrate. Just after the THz pulse, the temperature would quickly (100s of ns) become uniform due to the high thermal diffusivity of GaAs at low temperatures, decreasing the temperature at the QWs (see Appendix F). However, it is still difficult to say how much of the redshift was due to heating.

The temperature dependence of the splitting was also measured, as shown in Fig. 3.19. A splitting was observed up to 77 K. Past that temperature, the THz field simply broadened the exciton line. This temperature dependence seemed primarily due to a broader undriven exciton line at higher temperatures. Also, the heating shift became more significant at higher temperatures, as expected from the band gap dependence on temperature.

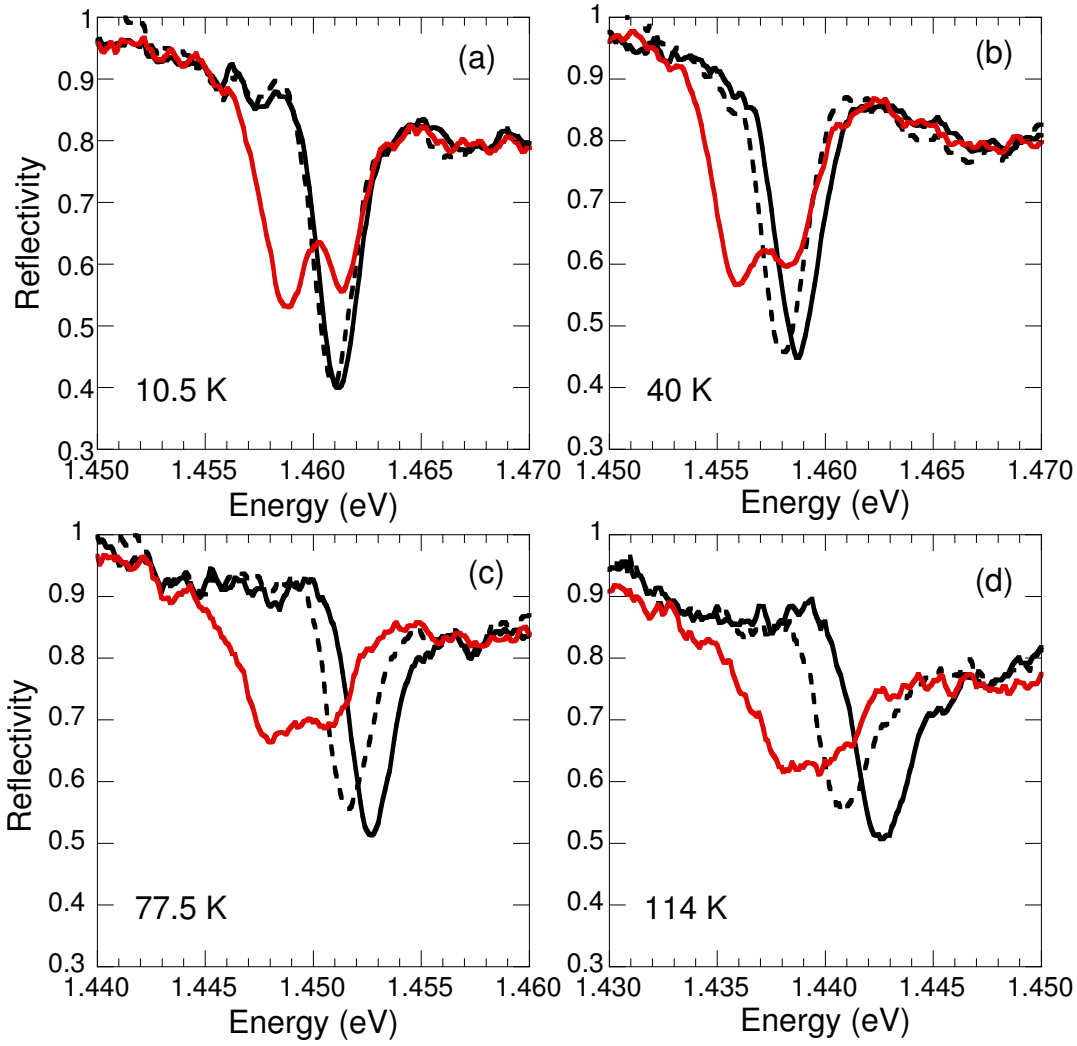

Figure 3.19: Reflectivity of Intest5 with $\hbar\omega = 14.1$ meV at (a) 10.5 K, (b) 40 K, (c) 77.5 K, and (d) 114 K. The reflectivity at each temperature is displayed with the THz pulse blocked (solid, black line), a few μs after the pulse (dashed, black line), and at the peak of the THz pulse (solid, red line). The THz power was 700 W at 10.5 K and 40 K, and was 950 W at 77.5 K and 114 K.

3.5 Conclusions

The results presented on InGaAs QWs have clearly demonstrated THz-dressed exciton states including Autler-Townes splitting due to a strong growth-direction THz field. The effects have been observed over a wide range of THz frequencies, where the detuning from the resonance was a significant fraction of the drive frequency. The results were fairly consistent with a Rabi model, in which the splitting is due to coherent oscillation between two exciton states. However, the overall redshift of the reflectivity spectra and the linear dependence of the splitting on power did not fit this model well. The redshift may be due to heating, but the dependence of the splitting on power is still not understood.

It is also interesting to note that the Rabi frequency was becoming a significant fraction of the drive frequency, making the RWA less valid. The ratio Ω/ω was estimated at $\sim$0.2 at the highest power for $\hbar\omega_{THz} = 14.1$ meV. This ratio was still rather small, but at $\hbar\omega_{THz} = 6.4$ meV the ratio should have been close to 0.5. Further increases in THz field at the QW positions should be possible as well, opening the way for further exciting strong-field experiments in which Floquet theory is more appropriate. This system is also technologically interesting as it is essentially a QW modulator driven at THz frequencies. The presence of quantum coherence in a QW modulator may enable fascinating new functionalities.

Chapter 4

THz-optical mixing in square quantum wells

This chapter and the following chapters will focus on another THz EO effect: mixing of the NIR and THz beams. This mixing generates sidebands at $\omega_{sideband} = \omega_{NIR} + n\omega_{THz}$, where $n = \pm 1, 2, \ldots$. For a weak NIR beam, these sidebands are useful as a probe of driven QWs. An advantage of studying THz EO effects using sideband generation is that the measurements are background free: sideband signals are only measured when the THz field is on. Sideband generation is also interesting technologically as it can be used for wavelength conversion.

The simplest system for studying THz-optical mixing is an undoped square GaAs QW because there are only a few relevant exciton states involved. This

chapter will explore the resonant behavior of mixing in this system as well as the dependence on an applied bias. The results will give an in-depth understanding of the physics and will also demonstrate voltage-controlled wavelength conversion. An interesting connection to fast quantum well modulators, used extensively in optoelectronics, will also be made.

4.1 Introduction to the Nonlinear Susceptibility

An brief introduction to the nonlinear susceptibility χ is helpful for understanding THz-optical mixing. In linear optics, the polarization of a medium can be expressed as $P = \epsilon_0(1+\chi_{linear})E$. A nonlinear dependence on the electric field can be added as a perturbative expansion in terms of E:

$$P(t) = \epsilon_0\chi^{(1)}E(t) + \epsilon_0\chi^{(2)}E^2(t) + \epsilon_0\chi^{(3)}E^3(t) + \ldots \tag{4.1}$$

This nonlinearity leads to mixing of different frequency components. For $E(t) = E_{NIR}\cos(\omega_{NIR}t) + E_{THz}\cos(\omega_{THz}t)$, the E^2 term gives rise to

$$\begin{aligned} P^{(2)} = \; & \epsilon_0\chi^{(2)}\Big[\tfrac{1}{2}E_{THz}^2 + \tfrac{1}{2}E_{NIR}^2 + \tfrac{1}{2}E_{THz}^2\cos 2\omega_{THz}t + \tfrac{1}{2}E_{NIR}^2\cos 2\omega_{NIR}t + \\ & E_{THz}E_{NIR}\cos(\omega_{NIR}+\omega_{THz})t + E_{THz}E_{NIR}\cos(\omega_{NIR}-\omega_{THz})t\Big]. \end{aligned} \tag{4.2}$$

This polarization can act as a source of new electromagnetic waves. The constant terms represent optical rectification, the $\cos 2\omega t$ terms represent 2nd harmonic

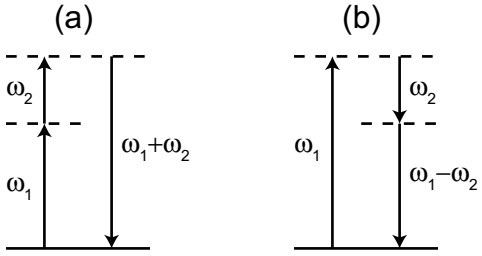

Figure 4.1: Energy level diagrams of sum (a) and difference (b) frequency generation. The solid line represents the ground state and the dashed lines represent virtual levels.

generation, and the $\cos(\omega_{NIR} \pm \omega_{THz})t$ terms represent sum/difference frequency generation (*i.e.* $n = \pm 1$ sideband generation). In general $\chi^{(2)}$ depends on the frequency components and the polarizations of the electric field. The polarization at a given frequency can then be written as

$$P_i^{(2)}(\omega_\alpha + \omega_\beta) = \sum_{jk} \sum_{(\alpha\beta)} \epsilon_0 \chi_{ijk}^{(2)}(\omega_\alpha + \omega_\beta; \omega_\alpha, \omega_\beta) E_j(\omega_\alpha) E_k(\omega_\beta). \tag{4.3}$$

The sum over different frequency components, represented by the indices α and β, is only carried out over frequency pairs that result in a fixed value for $\omega_\alpha + \omega_\beta$. The indices ijk represent the field directions, $\hat{x}$, $\hat{y}$, or $\hat{z}$. Optical rectification takes place when $\omega_\beta = -\omega_\alpha$, 2nd harmonic generation when $\omega_\beta = \omega_\alpha$, and sum (difference) frequency generation when ω_α and ω_β are the same (opposite) sign.

These $\chi^{(2)}$ processes can be illustrated schematically, as shown for sum and difference frequency generation in Fig. 4.1. The energy level diagrams display the frequencies lined up with virtual levels. Significant enhancement occurs when

the frequencies are nearly resonant with real levels, as will be the case in the experiments described.

One property of $\chi^{(2)}$ that will be immediately useful is that it is zero for materials with inversion symmetry. In fact, $\chi^{(m)} = 0$ for even m. This means that a bias must be applied to the QW to observe $n = \pm 1$ sidebands. These sidebands are the strongest for moderate THz intensities since they are generated in the lowest order of E_{THz}. Later in the chapter, an expression for $\chi^{(2)}$ and $\chi^{(3)}$ will be developed for excitons in a square QW, which will be used to model $n = \pm 1, 2$ sidebands.

4.2 Sample Characteristics

The sample called V5 was primarily used for these experiments. It consists of three 150 Å GaAs QWs in-between two gate QWs, as described in section 3.3. A sample called V4, which only had one 150 Å QW, was also measured and gave similar results. The sideband signal was weaker in V4, so results will only be presented on V5. The reflectivity of V5 is displayed in Fig. 4.2(a), showing the strong e1hh1X and e1lh1X absorption lines. When a voltage was applied, the e1hh1X and e1lh1X positions redshifted, as expected for the quantum confined Stark effect, and e1hh2X became optically allowed. Fig. 4.2(c) displays the e1hh1X position as

a function of voltage as well as the calculated positions (discussed in Section 4.4). The graph looks quite symmetric for $|V_{bias}| < 1.6$ V, but the tuning was poor for more negative voltages. One reason for this asymmetry is that this device started drawing some current past ± 1 V, and the IV curve was not always symmetric. At higher voltages ($|V_{bias}| >\sim 2$) the integrated PL was not constant. Another explanation for the poor tuning at negative voltages is that the GaAs/AlGaAs interface tends to be poorer that the AlGaAs/GaAs interface.[50] For these reasons, most of the sideband measurements were performed at +1 V.

Figure 4.2(b) plots the differential reflectivity signal taken by chopping the gate voltage between 0 and 1 V and locking into the changes in reflectivity. This measurement, usually called electroabsorption, can detect very small changes in reflectivity. The large amplitude features near e1hh1X and e1lh1X indicate a redshift of the peaks, and there was also a small dip at 1.5436 eV that we assign to e1hh2X. Based on this measurement, the e1hh2X-e1hh1X spacing was $\sim$10.8 meV at +1 V, quite close to the calculated spacing of $\sim$10.3 meV.

4.3 Sideband Measurements

Sidebands were measured on this sample by pressing Sapphire onto the front surface in the experimental geometry illustrated in Fig. 2.1(b), page 21. A side-

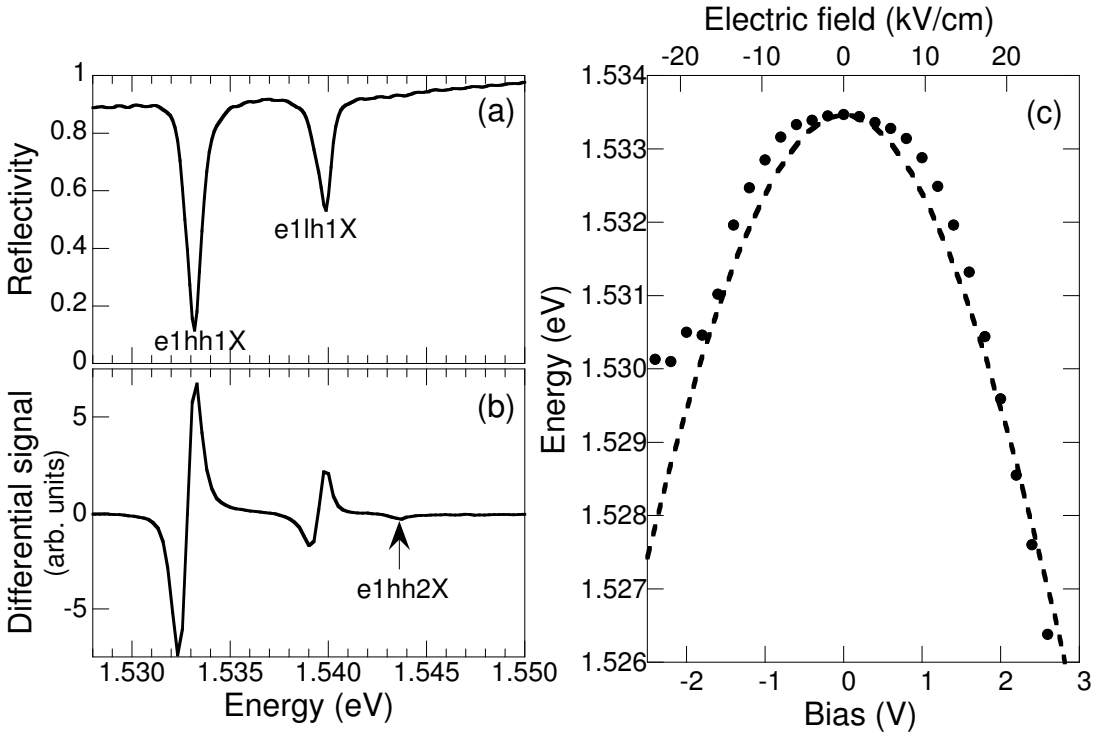

Figure 4.2: (a) Reflectivity spectrum of V5 at 19 K at zero bias. (b) Differential reflectivity for voltage chopped between 0 and +1 V. (c) Energy position of the e1hh1X absorption line as a function of bias at 19 K, solid cirlces. The dashed line plots the exciton model calculations (described in Section 4.4.1).

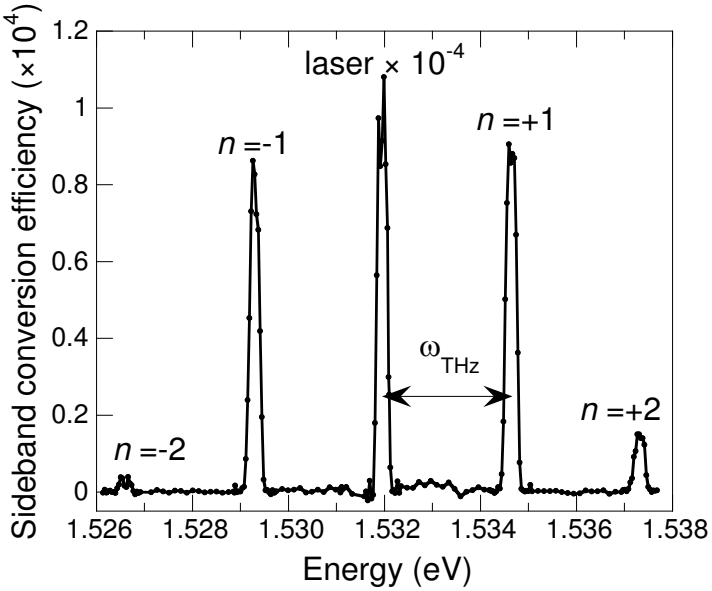

Figure 4.3: Sideband spectrum of V5 at 25 K at a bias of +1V. The THz intensity was ∼100 kW/cm^2 at $\hbar\omega_{THz} = 2.7$ meV.

band spectrum at $\hbar\omega_{THz} = 2.7$ meV is displayed in Fig. 4.3, demonstrating a relatively high $n = \pm 1$ sideband conversion efficiency–the ratio of the sideband power to the incident laser power. This conversion efficiency is comparable to that measured in coupled QW samples with a similar number of QWs.[29].

Nonlinear mixing in bulk crystals can be quite sensitive to the symmetry of the crystal lattice. Similarly, nonlinear mixing due to QW nonlinearities is quite sensitive to the QW symmetry. In these experiments, the inversion symmetry of the QW can be eliminated simply by applying a voltage. The results are shown in Fig. 4.4. The open circles and squares are the $n = +1$ and $n = +2$ sidebands, respectively, plotted as a function of voltage with fixed NIR frequency. (The

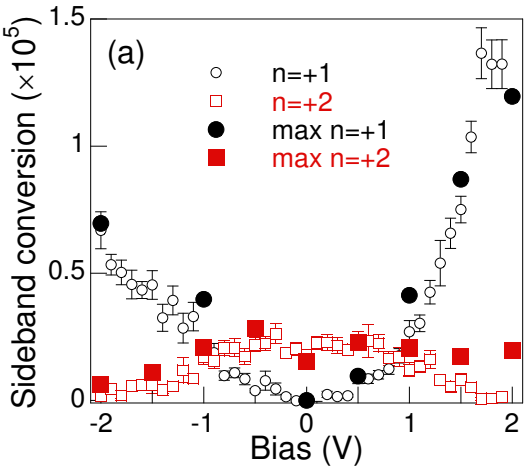

Figure 4.4: Sideband voltages scans of V5 at 19 K for $n = 1$ (circles) and $n = 2$ (squares) sidebands at $\hbar\omega_{NIR} = 1.530$ and 1.5325 eV, respectively. The solid symbols plot the sideband signal with the NIR laser always on the e1hh1X line. Taken with a NIR intensity of $\sim$30 W/cm^2.

significance of the solid markers will be explained later.) At zero bias, the $n = +1$ sideband was absent as $\chi^{(2)}$ processes were forbidden, while there was a significant $n = +2$ sideband, which came from a $\chi^{(3)}$ process. When a voltage was applied, the inversion symmetry was eliminated, so the $n = +1$ sideband appeared. The $n = +1$ sideband increased roughly proportional to V_{bias}^2, as expected from our $\chi^{(2)}$ model, and the $n = +2$ sideband remained relatively constant until it decreased at higher voltages. In principle, the two curves should be symmetric about zero bias, but the $n = +1$ sidebands in particular were weaker for negative voltages. This asymmetry is linked to the asymmetry of the reflectivity and PL, as discussed in the previous section. The lower sideband signal at higher negative voltages must

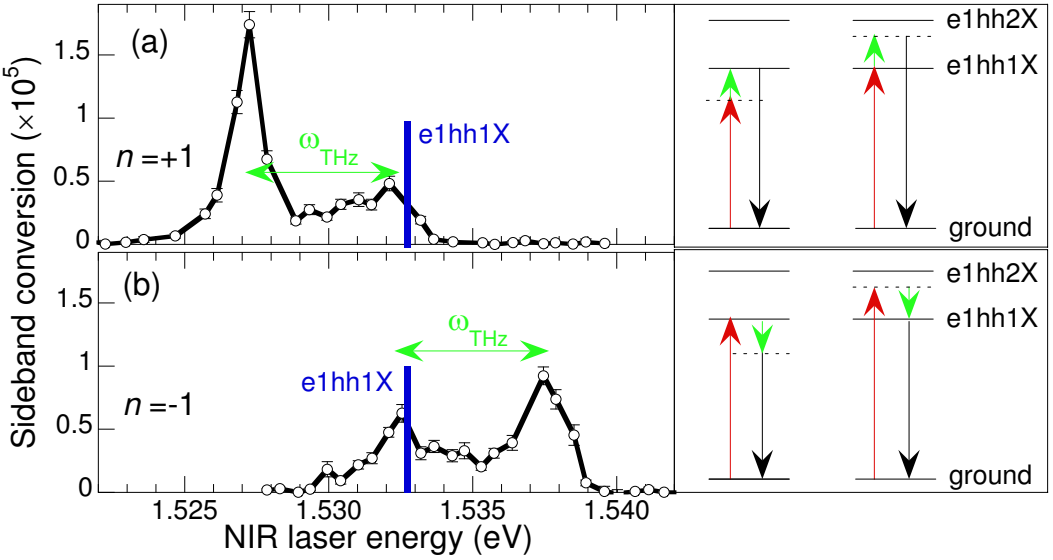

Figure 4.5: (a) $n = +1$ and (b) $n = -1$ sideband resonance spectra of V5 at 19 K taken with $\hbar\omega_{THz} = 5.5$ meV. The THz intensity was $\sim$30 kW/cm^2, the NIR intensity was $\sim$30 W/cm^2, and the bias was +1 V. The blue vertical lines indicate the e1hh1X position at +1 V, and the sideband energy level diagrams for the two resonances are displayed on the right.

have been due to the poor tuning seen in Fig. 4.2(c) for $V_{bias} <\sim -1.6$ V.

Figure 4.5 displays $n = \pm 1$ sideband resonance spectra, taken by measuring the sideband signal at $\omega_{NIR} \pm \omega_{THz}$, while scanning the NIR frequency. In each spectrum, there were two resonances: one in which ω_{NIR} was near e1hh1X and one in which $\omega_{sideband}$ was near e1hh1X. This means the two resonances were always separated by ω_{THz}. No resonance was clearly seen when ω_{NIR} or $\omega_{sideband}$ alone was near e1hh2X. The energy level diagrams for the resonances are shown to the right of the figure. When ω_{THz} was near the e1hh1X-e1hh2X transition, the higher energy resonance dominated. In this case the double resonance condition

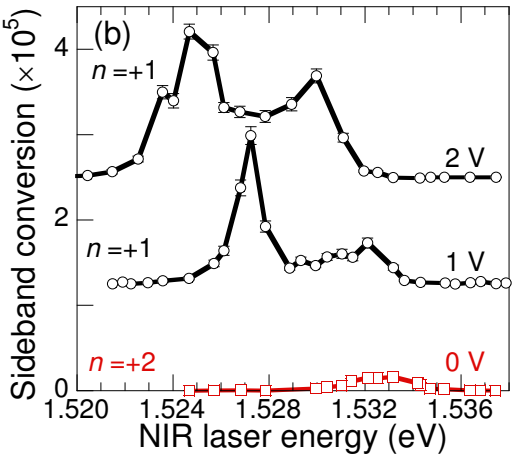

Figure 4.6: Sideband resonance spectra at 19 K with $\hbar\omega_{THz} = 5.5$ meV, a THz intensity of ∼30 kW/cm^2, and a NIR intensity of ∼30 W/cm^2. The $n = 2$ spectrum at $V_{bias} = 0$ V is shown with red, open squares and the $n = 1$ spectra with black, open circles at $V_{bias} = 1$ V and 2 V. The spectra are offset.

was achieved, in which ω_{NIR} was resonant with e1hh1X, and $\omega_{sideband}$ was resonant with e1hh2X. One might also expect resonances with e1lh1X, but these were only observed for low THz frequencies ($\hbar\omega_{THz} = 2.7$ meV).

When a voltage was applied to the sample, the sideband resonance spectra shifted according to the shift in the exciton energy position. Fig. 4.6 shows sideband resonance spectra taken at different bias voltages. At 0 V the $n = +2$ spectra is displayed because the $n = \pm 1$ sidebands were forbidden. The $n = +2$ sideband signal was relatively weak, and the only resonance occurred when $\hbar\omega_{NIR}$ was close to e1hh1X. At 1 and 2 V, the $n = +1$ spectra redshifted according to the QCSE. Many of these spectra were taken at different voltages, and the peak of the higher energy resonance at e1hh1X was plotted as a function of bias in Fig. 4.4

(solid symbols). This was performed because the sideband signal in a sideband voltage scan can sometimes decrease only because the voltage has shifted away the exciton resonance.

Sidebands were observed in this sample at many different THz frequencies from $\hbar\omega_{THz} = 2.7$ to 14.1 meV. $n = -1$ sideband resonance spectra at several of these THz frequencies are plotted in Fig. 4.7. As a function of ω_{THz} there appears to be a resonance for $\hbar\omega_{THz} = 10.4$ meV, quite close to the measured e1hh1X-e1hh2X spacing, ∼10.8 meV. However, the sideband signal was even stronger at $\hbar\omega_{THz} = 2.7$ meV. The intensity of the THz beam outside the sample did vary some with frequency (see caption), and the intensity at the QWs is hard to determine. However, the resonance near 10 meV and the strong low-frequency response are clear. Another trend in the figure involves the two NIR resonances discussed previously. The higher energy resonance blueshifted as the THz frequency increased, as this resonance occurred when $\omega_{NIR} = E_{hh1X} + \omega_{THz}$. The lower energy resonance stayed at the exciton energy, but was only significant at low THz frequencies. Similar behavior for the $n = +1$ sidebands has been observed, but the data quality was not very good. In that case, the lower energy resonance redshifted and became weaker as the THz frequency increased, while the higher energy resonance remained at the exciton energy.

One reason for the trouble with $n = +1$ sideband data involved the $n = \pm 1$

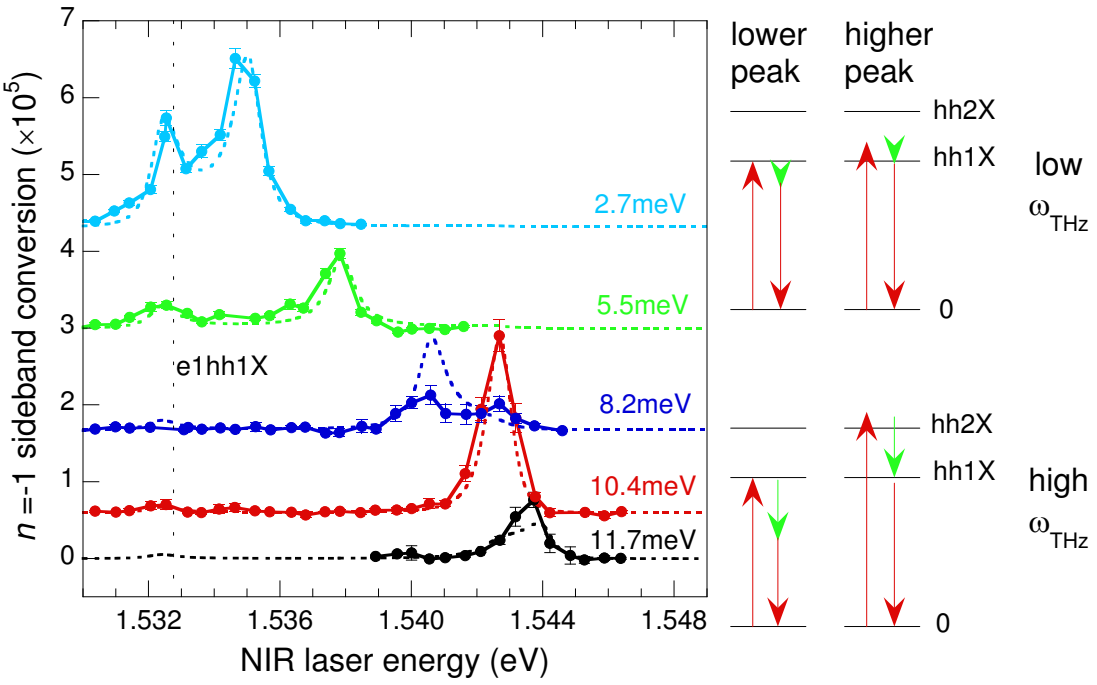

Figure 4.7: $n = -1$ sideband resonance spectra of V5 at 25 K (solid lines, circles), taken at a series of THz frequencies with a NIR intensity of ~30 kW/cm^2. The spectra are offset and labelled according to $\hbar\omega_{THz}$. The THz intensity outside the sample for $\hbar\omega_{THz}$ = 2.7, 5.5, 8.2, 10.4, and 11.7 meV was approximately 25, 30, 40, 55, and 55 kW/cm^2, respectively. The dashed lines represent $\left|\chi^{(2)}\right|^2$ as calculated in the 3 state model. The sideband energy level diagrams for the higher and lower resonances at high and low ω_{THz} are displayed on the right.

sideband dependence on NIR intensity, as shown in Fig. 4.8. The $n = +1$ sideband saturates at much lower NIR powers than the $n = -1$ sideband. This occurred because the NIR laser was right on the e1hh1X line for the $n = +1$ resonance (see Fig. 4.9(a)). The laser excited an exciton density of $\sim 2 \times 10^{10}$ cm^{-2} per QW at a NIR intensity of $\sim$30 W/cm^2 ($\sim$0.6 mW), assuming an exciton lifetime of $\sim$0.5 ns and 90% absorbance for all three QWs. Some exciton-exciton interactions and absorption bleaching were likely to occur at this carrier density, which was consistent with the saturation of the sideband signal. The interband absorption was much lower at the $n = -1$ resonance, so the $n = -1$ sideband saturated at much higher NIR intensities. This saturation effect had an influence on some of the sideband spectra measured. However, measurements taken with an order of magnitude lower NIR intensity did not yield results qualitatively different from those shown in Fig. 4.6 and 4.7.

For low NIR intensities, the $n = +1$ and $n = -1$ sideband resonance spectra were essentially identical except the $n = -1$ spectrum was shifted up by $\hbar\omega_{THz}$, as displayed in Fig. 4.9(a). This translation symmetry was no longer present when the NIR power was increased to 3 mW, as shown in Fig. 4.9(b). The $n = \pm 1$ resonances near e1hh1X appeared to be heavily saturated due to the strong absorption. Interestingly, at high THz intensities and low NIR power, the translation symmetry was still present.

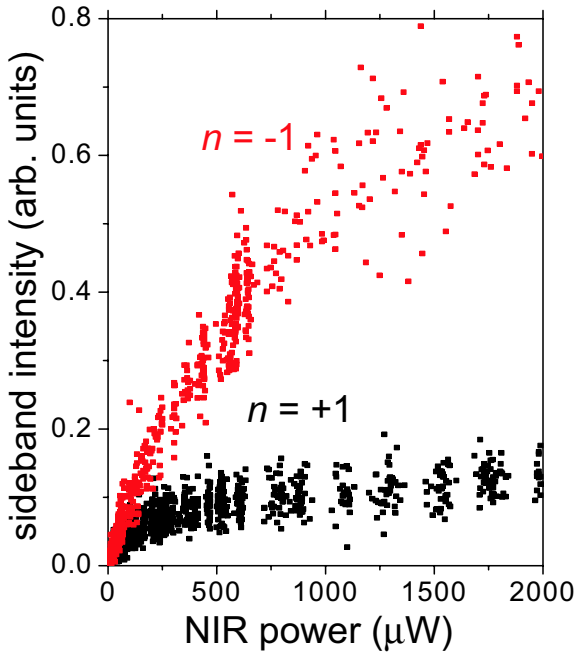

Figure 4.8: $n = +1$ (black) and $n = -1$ (red) sideband dependence on NIR power for V5 at 19 K, with $\hbar\omega_{THz} = 10.4$ meV. The sample was at $V_{bias} = +1V$, with a THz intensity outside the sample of $\sim$30 kW/cm^2. The $n = +1$ data was taken at the peak of the $n = +1$ sideband resonance at $\hbar\omega_{NIR} = 1.5328$ eV, right on the e1hh1X line. The $n = -1$ data was taken at the peak of the $n = -1$ sideband resonance at $\hbar\omega_{NIR} = 1.5436$ eV. 1 mW of NIR power corresponds to $\sim$50 W/cm^2 at the focus.

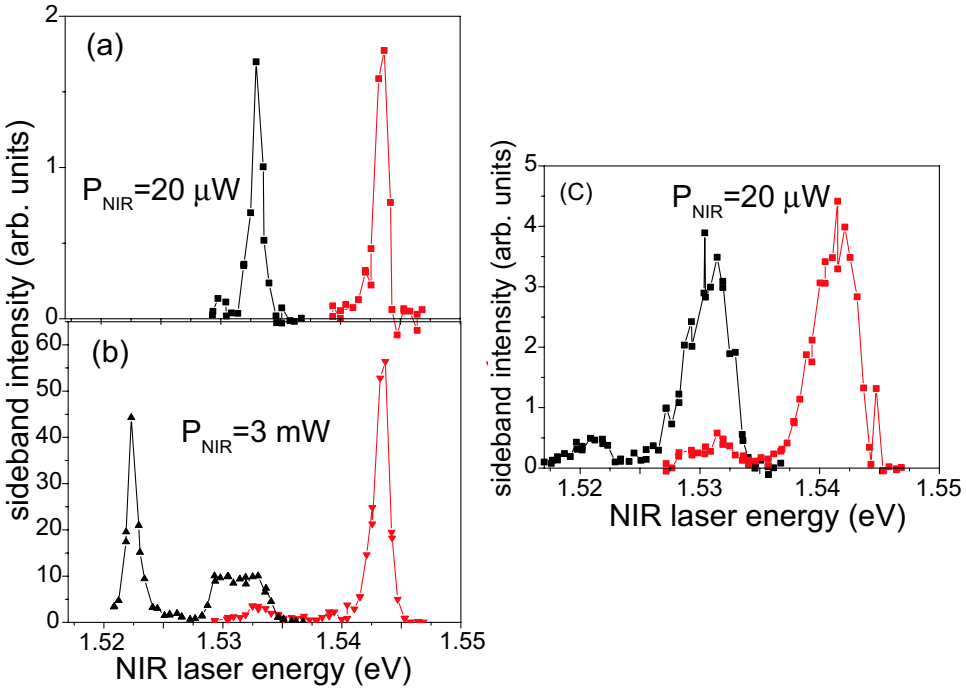

Figure 4.9: $n = +1$ (black) and $n = -1$ (red) sideband resonance spectra of V5 at 19 K taken at $\hbar\omega_{THz} = 10.4$ meV and $V_{bias} = +1$ V. (a) Low NIR power (20 μW) and low THz intensity ($\sim$30 kW/cm^2). (b) High NIR power (3 mW) and low THz intensity ($\sim$30 kW/cm^2). (c) Low NIR power (20 μW) and high THz intensity ($\sim$130 kW/cm^2).

Sideband measurements were also performed as a function of THz power in an attempt to observe non-perturbative effects, similar to the effects on interband absorption presented in Chapter 3. Fig. 4.10(a) displays sideband resonance spectra for several THz powers. The effect was similar to that observed in Fig. 3.6. The resonance redshifted and became broader at increasing THz powers. As with the changes in absorption of V5, these effects may have been partly due to in-plane THz fields and perhaps cavity effects that complicate interpretation. Fig. 4.10(b) shows the saturation of the peak sideband signal as a function of power and the linear behavior of the integrated signal. This indicates that the saturation was probably due to the broadening. Experiments in a gated InGaAs QW sample, similar to that discussed in Chapter 3, would be quite interesting as the in-plane fields and cavity effects would be eliminated.

4.4 Model and Discussion

For moderate THz intensities, sideband generation in this system can be well described by the nonlinear susceptibility. This model helps one better understand the nonlinear processes which give rise to the sidebands. The first step in developing the model is to characterize the exciton states of the QW. The exciton states can be estimated by using the variational wavefunction, Eq. (3.2). The assump-

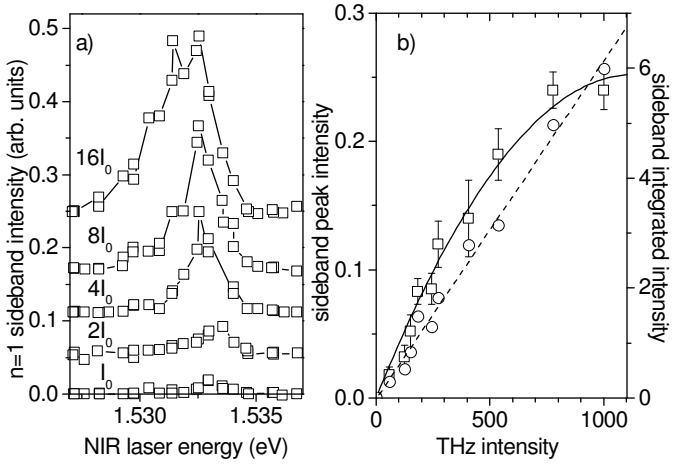

Figure 4.10: (a) $n = +1$ sideband resonance spectra of V5 at 19 K for a series of THz powers. The spectra are labelled by the THz power relative to the lowest power, with the highest power at ∼1 kW. The spectra were taken at $\hbar\omega_{THz} = 10.4$ and $V_{bias} = +1$ V. (b) $n = +1$ sideband peaks (open squares) and integrated signal (open circles) as a function of THz power. The curves are drawn as a guide to the eyes.

tions made using this approximation and their validity are discussed in Section 3.1.

4.4.1 QW Exciton states

The procedure we will use for calculating the QW exciton states is very similar to that described in Ref. [26]. First, the growth-direction wavefunctions in the presence of an electric field must be calculated, ignoring the Coulomb interaction. This is done by solving the Schrödinger equation

$$\left[-\frac{\hbar^2}{2m_e^*}\frac{\partial^2}{\partial z_e^2} + V_e(z_e) + eE_{bias}z\right]\varphi_{cm}(z_e) = E_{cm}\varphi_{cm}(z_e), \tag{4.4}$$

where E_{bias} is the applied electric field, and φ_{cm} is the mth growth direction wavefunction in the conduction band with energy E_{cm}. (A similar expression can be written for the hole wavefunctions.) This was solved by numerically integrating the differential equation and iterating E_{cm} until the solution decayed to zero in the barriers.

The variational parameter λ_{mn} was found by minimizing the expectation value of the energy of the wavefunction,

$$E(\lambda_{mn}) = E_{cm} + E_{vn} + \frac{\hbar^2}{2m^*_{eh}\lambda^2_{mn}} - \frac{e^2}{\pi\epsilon\lambda^2_{mn}} \int dz_e dz_h \left|\varphi_{cm}(z_e)\right|^2 \left|\varphi_{vn}(z_h)\right|^2 \int \rho d\rho \frac{e^{-2\rho/\lambda_{mn}}}{\sqrt{\rho^2+(z_e-z_h)^2}}. \quad (4.5)$$

The first two terms don't depend on λ_{mn}, the third term comes from the in-plane kinetic energy, and the fourth term comes from the Coulomb interaction. When this function was minimized, λ was found to be between 155 and 170 Å for for e1hh1X and e1hh2X depending on the electric field.

Fig. 4.11 displays some of the results of these calculations performed for e1hh1X and e1hh2X as a function of the electric field. Fig. 4.11(a) plots the e1, hh1, and hh2 energies as well as the binding energies of the two excitons. The energies of e1 and hh1 decrease with applied field as the wavefunctions move toward the lower energy side of the well. The hh2 wavefunction samples both sides of the well (for the fields shown) as it has higher energy, so its energy stays

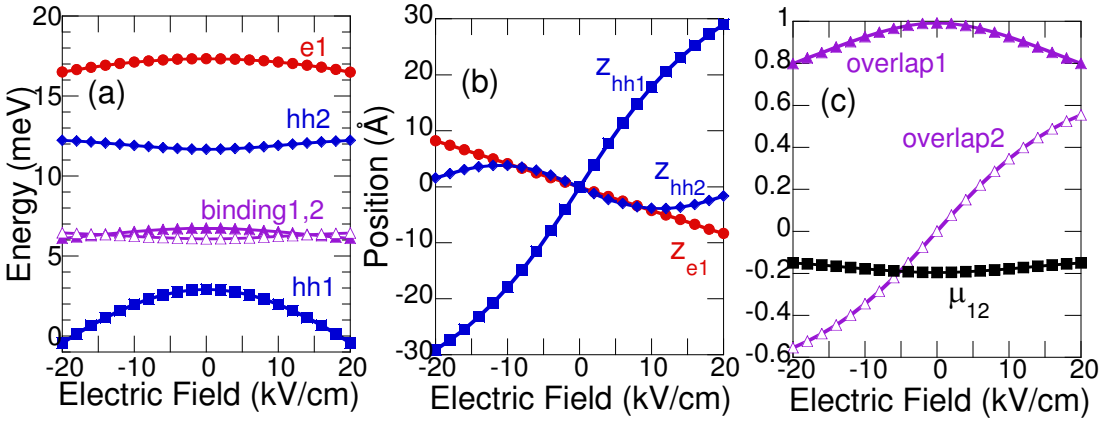

Figure 4.11: (a) Calculated electron (red circles) and hole (blue squares and diamonds) energies as a function of electric field. The calculated binding energies of e1hh1X and e1hh2X (solid and open purple triangles, respectively) are also plotted. (b) Expectation value of the growth direction position of the electron and hole states as a function of electric field. (c) Overlap integrals $\langle\varphi_{c1}|\varphi_{v1,2}\rangle$ for e1hh1X and e1hh2X, and the excitonic intersubband dipole moment divided by the well width. Calculations were performed using $m_e^* = 0.067$, $m_{hh}^* = 0.48$ (growth-direction), $m_{eh}^* = 0.037$ (in-plane reduced), $\epsilon = 12.4\epsilon_0$, a conduction band offset of 260 meV, and a valence band offset of 170 meV.

fairly constant and even increases a bit with field. The binding energies change little with field because the field is insufficient to significantly separate electrons and holes. This can be seen in Fig. 4.11(b), which displays the average growth-direction position for the electron and hole states. At 20 kV/cm the average e1-hh1 separation in the growth-direction is less than 40 Å, much less than the Bohr radius. The energies obtained for these calculations were used to model the e1hh1X energy position as a function of electric field, as shown in Fig. 4.2.

Fig. 4.11(c) displays parameters that determine the dipole matrix elements,

which are discussed further in the next section and are defined in Eqs. (4.9) and (4.10). The interband matrix elements are proportional to the overlap integrals, $I_{1,2} \equiv \langle \varphi_{c1} | \varphi_{v1,2} \rangle$. I_1 decreases with field as the electron and hole are separated, while I_2 increases with field as the symmetry is broken. The excitonic intersubband dipole moment, μ_{12} stays relatively constant.

4.4.2 $\chi^{(2)}$ model

The $n = 1$ sideband generation arises from the polarization at $\omega_{NIR}+\omega_{THz}$, which can be written as

$$P_i^{(2)}(\omega_{NIR} + \omega_{THz}) = 2 \sum_{jk} \epsilon_0 \chi_{ijk}^{(2)}(\omega_{NIR} + \omega_{THz}; \omega_{THz}, \omega_{NIR}) E_j(\omega_{THz}) E_k(\omega_{NIR}). \tag{4.6}$$

This expression is obtained by substituting the THz and NIR frequencies into Eq. (4.3). The sum over frequency pairs results in the factor of 2. An expression for $\chi^{(2)}$ can be taken from Ref. [51]:

$$\begin{aligned}
\chi_{ijk}^{(2)}(\omega_{NIR} + \omega_{THz}; \omega_{THz}, \omega_{NIR}) = \frac{N}{2\hbar^2 \epsilon_0} \sum_{mn\nu} (\rho_{mm}^{(0)} - \rho_{\nu\nu}^{(0)}) \\
\times \Bigg\{ \frac{\mu_{mn}^i \mu_{n\nu}^j \mu_{\nu m}^k}{(\omega_{nm} - \omega_{NIR} - \omega_{THz} - i\gamma_{nm})(\omega_{\nu m} - \omega_{NIR} - i\gamma_{\nu m})} \\
+ \frac{\mu_{mn}^i \mu_{n\nu}^k \mu_{\nu m}^j}{(\omega_{nm} - \omega_{NIR} - \omega_{THz} - i\gamma_{nm})(\omega_{\nu m} - \omega_{THz} - i\gamma_{\nu m})} \\
- \frac{\mu_{n\nu}^i \mu_{mn}^j \mu_{\nu m}^k}{(\omega_{\nu n} - \omega_{NIR} - \omega_{THz} - i\gamma_{\nu n})(\omega_{\nu m} - \omega_{NIR} - i\gamma_{\nu m})}
\end{aligned}$$

$$-\frac{\mu^i_{n\nu}\mu^k_{mn}\mu^j_{\nu m}}{(\omega_{\nu n}-\omega_{NIR}-\omega_{THz}-i\gamma_{\nu n})(\omega_{\nu m}-\omega_{THz}-i\gamma_{\nu m})}\Bigg\}. \tag{4.7}$$

In Eq. (4.7), $\rho^{(0)}_{mn}$ is the equilibrium density matrix; μ^i_{mn} is the dipole matrix element $\langle m|-ex^i|n\rangle$; $\omega_{mn}=(E_m-E_n)/\hbar$; and γ_{mn} represents the damping rate of the ρ_{mn} coherence. In atomic systems, N is the atomic density, so for a QW N is replaced by 1/Volume. For a growth-direction THz field ($j=\hat{z}$) and in-plane NIR field ($i=k=\hat{x}$), the sideband polarization is determined by $\chi^{(2)}_{xzx}$.

For the square QW, we will only include three states, $|0\rangle$ = ground state, $|1\rangle$ = e1hh1X, and $|2\rangle$ = e1hh2X. Higher exciton states can be ignored because they are weaker and off resonance with ω_{THz}. Light hole exciton states can be ignored because they should not couple to heavy hole excitons, and the lh1-lh2 spacing is much larger than ω_{THz}.

In this three-level system, most of the terms in Eq. (4.7) can be eliminated. First, highly nonresonant terms such as those with $(\omega_{01}-\omega_{NIR})$ in the denominator can be eliminated. Other terms are eliminated because only the ground state has an equilibrium population ($\rho^{(0)}_{00}=1$ and $\rho^{(0)}_{11}=\rho^{(0)}_{22}=0$). Finally terms can be eliminated because of vanishing dipole matrix elements. This leaves only four terms in $\chi^{(2)}_{xzx}$:

$$\chi^{(2)}_{xzx}(\omega_{NIR}+\omega_{THz};\omega_{THz},\omega_{NIR})=$$
$$\frac{1}{\hbar^2 Aw\epsilon_0}\sum_{n,\nu=1,2}\frac{\mu^x_{0n}\mu^z_{n\nu}\mu^x_{\nu 0}}{(\omega_{n0}-\omega_{NIR}-\omega_{THz}-i\gamma_{n0})(\omega_{\nu 0}-\omega_{NIR}-i\gamma_{\nu 0})}, \tag{4.8}$$

where A and w are the QW area and width, respectively. This expression for $\chi^{(2)}$ has been multiplied by 2 for the spin degeneracy. Having $\chi^{(2)}$ depend on the area seems strange, but the interband matrix elements are proportional to $\sqrt{A}$.[52]

$$\mu^x_{n0} = \sqrt{A}\langle u_{k=0,c}|ex|u_{k=0,v}\rangle(\frac{2}{\pi\lambda_n^2})^{1/2}I_n, \tag{4.9}$$

where I_n is the overlap integral $\langle\varphi_{c1}|\varphi_{vn}\rangle$. The intersubband matrix elements are

$$\mu^z_{n\nu} = e\langle\varphi_{vn}|z_h|\varphi_{v\nu}\rangle - e\delta_{n\nu}\langle\varphi_{c1}|z_e|\varphi_{c1}\rangle. \tag{4.10}$$

For $n \neq \nu$, the usual intersubband matrix element is recovered, while μ^z_{nn} represents the dipole moment between electron and hole.

The $\nu = 1$, $n = 2$ term in Eq. (4.8) represents an excitonic intersubband resonance, in which $\chi^{(2)}$ is strongest when $\omega_{sideband}$ and ω_{NIR} line up with e1hh2X and e1hh1X, respectively. This gives an indirect resonance when ω_{THz} is near the excitonic intersubband spacing. The $\nu = 2$, $n = 1$ term is nonresonant for $n = +1$ sidebands, but is resonant for $n = -1$ sidebands ($\omega_{THz} \rightarrow -\omega_{THz}$). The $\nu = n$ terms are resonant when both $\omega_{sideband}$ and ω_{NIR} line up with a single exciton line, making them strongest for $\omega_{THz} < \gamma_{n0}$. We interpret the $\nu = n$ terms as being due to the quasi-static modulation of the exciton susceptibility. Appendix E evaluates sideband generation from this quasi-static modulation, and the result is quite similar to the $\nu = n$ terms of Eq. (4.8).

The sideband intensity must in principle be determined using the coupled wave equations, derived from Maxwell's equations (see Appendix D). However, since the interaction length in these QW samples is small, $|\chi^{(2)}|^2$ provides a good qualitative description of the sideband resonances. $\chi^{(2)}$ was evaluated using Eq. (4.8) with $\hbar\gamma_{10} = 0.5$ meV, $\hbar\gamma_{20} = 1.0$ meV, $\langle u_{k=0,c}|ex|u_{k=0,v}\rangle = 4.9$ Å.[53] The value of γ_{10} was determined by the half-width-half-max of the linear absorption line. The value of γ_{20} was estimated to be larger since the e1hh2X absorption at $V_{bias} = 1$ V was quite small. In Fig. 4.7, $|\chi^{(2)}_{xzx}(\omega_{NIR} - \omega_{THz}; -\omega_{THz}, \omega_{NIR})|^2$ is plotted along with the experimental $n = -1$ sideband resonance spectra. The curves are normalized so that the peak experimental and model values match up for $\hbar\omega_{THz} = 10.4$ meV. The resonance positions agree pretty well, and the same trends are apparent. These trends are made even clearer by Fig. 4.12. The value of $|\chi^{(2)}(\omega_{NIR})|^2$ for $n = \pm 1$ sidebands is plotted in Fig. 4.12(a),(b) for several values of ω_{THz}, showing the shifting of the two NIR resonances more clearly. Fig. 4.12(c) plots the maximum of $|\chi^{(2)}(\omega_{NIR})|^2$ as a function of $\hbar\omega_{THz}$, displaying the strong sideband generation at low frequencies and the resonance at the excitonic intersubband spacing. Fig. 4.12(d) displays the maximum of $|\chi^{(2)}(\omega_{NIR})|^2$ as a function of electric field at $\hbar\omega_{THz} = 5.5$ meV. This curve can be compared to the experimental sideband voltage tuning in Fig. 4.6(a). The predicted saturation of the $n = \pm 1$ sidebands at higher voltages is due to the

decrease of μ_{01} and μ_{12} and the decreasing slopes of μ_{11} and μ_{02}, as shown in Fig. 4.11. Hints of this saturation have been observed experimentally, but they were not clear because of the strange tuning behavior at large bias voltages.

An expression for $\chi^{(3)}$ can be obtained in a similar manner as for $\chi^{(2)}$. The result is

$$\chi^{(3)}_{xzzx}(\omega_{NIR}+2\omega_{THz};\omega_{THz},\omega_{THz},\omega_{NIR}) = \frac{2}{3\hbar^3 A w \epsilon_0}\sum_{n,\nu,l=1,2} \frac{\mu^x_{0n}\mu^z_{n\nu}\mu^z_{\nu l}\mu^x_{l0}}{(\omega_{n0}-\omega_{NIR}-2\omega_{THz}-i\gamma_{n0})\,(\omega_{\nu 0}-\omega_{NIR}-\omega_{THz}-i\gamma_{\nu 0})} \times \frac{1}{(\omega_{l0}-\omega_{NIR}-i\gamma_{l0})}. \tag{4.11}$$

Equation (4.11) includes excitonic intersubband resonances and low frequency resonances as in Eq. (4.8) but has more terms. At zero bias, only the $n = l = 1, \nu = 2$ term is nonzero. This term is plotted for several THz frequencies in Fig. 4.13. The main resonance is on the e1hh1X line, but there is also a smaller resonance that starts near e1hh2X at zero frequency and shifts to lower energy as the THz frequency increases. This behavior is very similar to the THz-induced changes in exciton absorption in InGaAs QWs, as displayed in Fig. 3.12. However, there is no anticrossing as the $\chi^{(3)}$ calculation is perturbative. There is also a small resonance $2\omega_{THz}$ below the e1hh1X line similar to that seen in the $n = +1$ sidebands. We interpret these resonances as being due to replicas of the e1hh1X line induced by the strong THz field.[36]

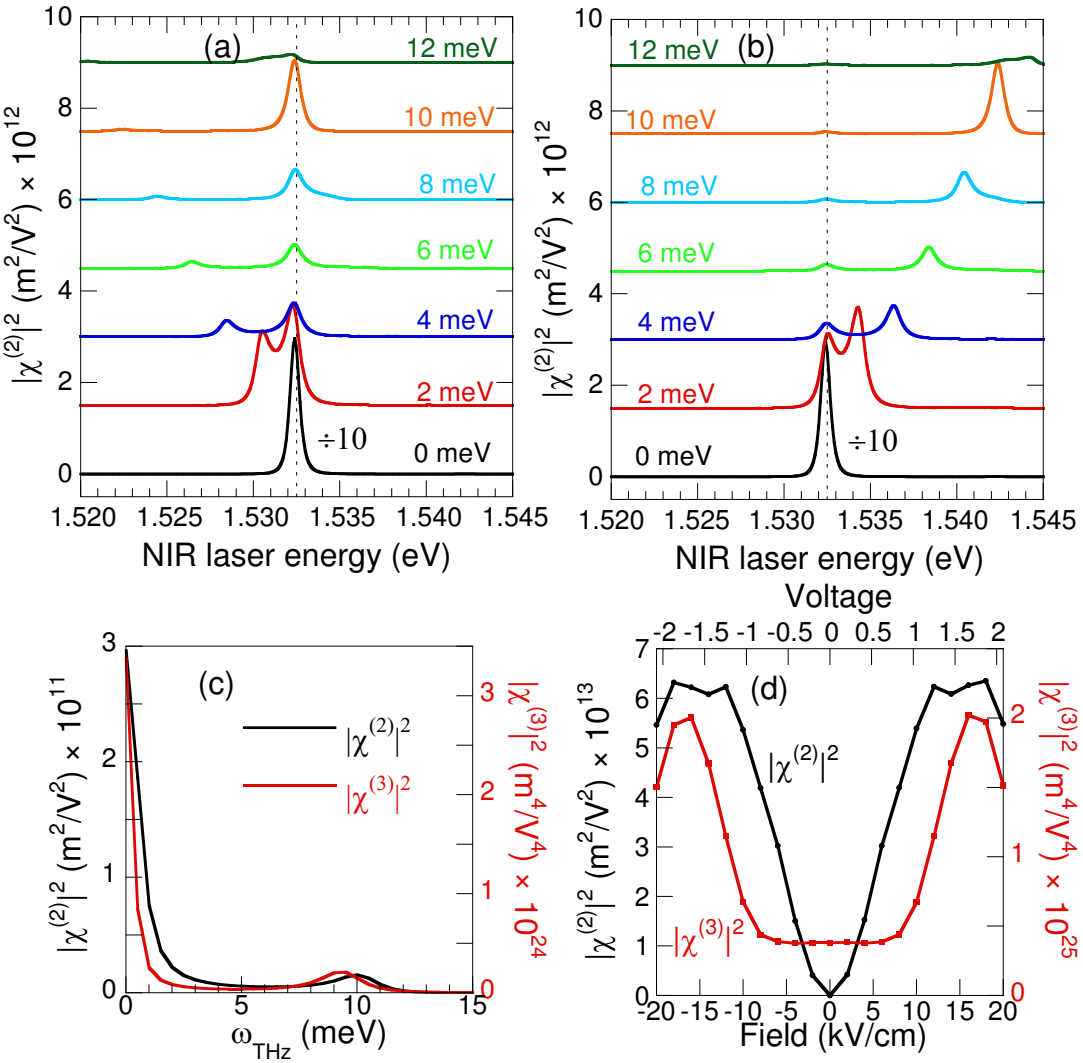

Figure 4.12: (a) $|\chi^{(2)}(\omega_{NIR})|^2$ as calculated from Eq. (4.8) for $n = +1$ and (b) $n = -1$ sidebands at a 10 kV/cm dc electric field. The calculations are plotted at a series of THz frequencies, offset and labelled according to $\hbar\omega_{THz}$. The dashed line indicates the e1hh1X position. The zero frequency curve is divided by 10 for clarity. (c) Calculated maximum of $|\chi^{(2)}(\omega_{NIR})|^2$ at 10 kV/cm (black) and $|\chi^{(3)}(\omega_{NIR})|^2$ at 0 kV/cm (red) as a function of $\hbar\omega_{THz}$. (d) Calculated maximum of $|\chi^{(2)}(\omega_{NIR})|^2$ (black) and $|\chi^{(3)}(\omega_{NIR})|^2$ (red) at $\hbar\omega_{THz} = 5.5$ meV as a function of DC electric field.

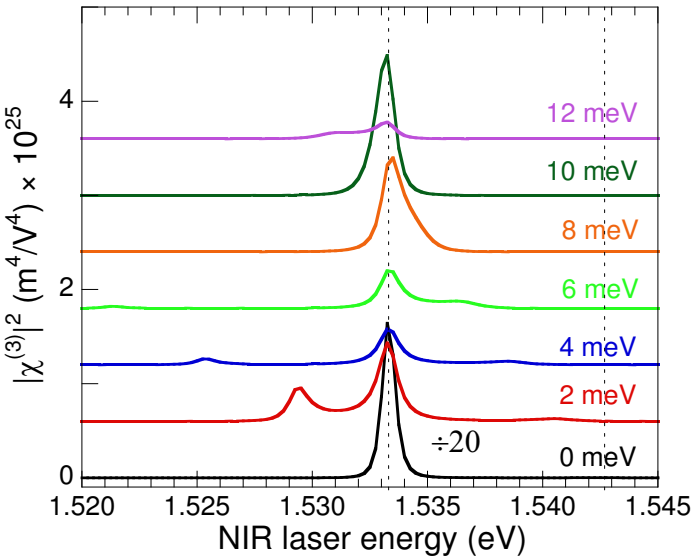

Figure 4.13: $|\chi^{(3)}(\omega_{NIR})|^2$ as calculated from Eq. (4.11) for $n = +2$ sidebands at a 0 bias. The calculations are plotted at a series of THz frequencies, offset and labelled according to $\hbar\omega_{THz}$. The dashed lines indicate the e1hh1X and e1hh2X calculated positions. The zero frequency curve is divided by 20 for clarity.

The effect of a dc electric field on the $n = \pm 2$ sidebands is not obvious because many more terms in $\chi^{(3)}$ become allowed as the symmetry is broken. The $n = +2$ sideband voltage tuning is displayed in Fig. 4.6(a), and the calculated maximum of $|\chi^{(3)}(\omega_{NIR})|^2$ is shown in Fig. 4.12. The relatively flat area for small voltages is likely due to competing effects. The matrix elements for the $n = l = 1, \nu = 2$ term are decreasing while other terms start to become allowed. The cause of the sharp increase of $|\chi^{(3)}|^2$ near 1.5 V is not understood or observed.

There is an obvious symmetry between the $n = \pm 1$ resonances shown in Fig. 4.12(a,b). The $n = -1$ resonance is simply a translation by ω_{THz} of the

$n = +1$ resonance. Looking at Fig. 4.3, this implies that if one instead sent the NIR laser in at the $n = +1$ sideband energy, the conversion efficiency to the $n = -1$ sideband (where the laser is in the figure) would be the same. This symmetry is guaranteed for lossless media, which have full permutation symmetry of the nonlinear susceptibility.[54] However, there is significant absorption when near exciton resonances in the QW system, so the full permutation symmetry is not guaranteed. From Fig. 4.9(a) and (c), the $n = \pm 1$ symmetry was present so long as the NIR beam was at low intensity, even when there were nonperturbative effects from the strong THz field. The generation of significant carriers when the laser was near the exciton absorption destroyed the symmetry, as seen in Fig. 4.9(b).

4.4.3 Conversion efficiency calculations

The conversion efficiency can be calculated relatively simply from $\chi^{(2)}$ and $\chi^{(3)}$ using Eq. (D.18) and (D.20). These equations were derived assuming a bulk nonlinear material, which is not the case in this system, but they should still give reasonable estimates. Figure 4.14 displays this calculated conversion efficiency for $n = \pm 1$ and $n = \pm 2$ sidebands for 6 QWs (equivalent to the double-pass through V5). A THz field of 3 kV/cm is used, close to the field expected in Fig. 4.7, but the calculated conversion is 2 orders of magnitude higher than that measured.

Of course there is significant uncertainty in these calculated conversion efficiencies due to uncertainties in the material parameters and the approximations made. One method of checking for errors in the model is to compare the calculated linear absorption to the measured absorption. Using the same general method in calculating the linear absorption as with the sidebands gives an absorption value less than half of that measured. This could be accounted for by the cavity enhancement. The higher measured absorption could signify that the interband oscillator strength (and, hence, the nonlinear susceptibility) has been underestimated in the calculations, making it unlikely that the model overestimates the conversion efficiency. Maslov and Citrin have performed more sophisticated calculations of the conversion efficiency for a single GaAs QW,[34] which also resulted in much higher conversion efficiencies than those measured. The discrepancy may be the result of a poor THz field at the QW position as discussed previously. Better THz coupling, as with an Al-coated sample, could yield far higher sideband conversion.

4.5 Conclusions

THz-optical mixing has been thoroughly studied and modelled in a square GaAs QW. This system is relatively simple, so this research provides a solid foundation for understanding THz-optical mixing in QWs. From an applied per-

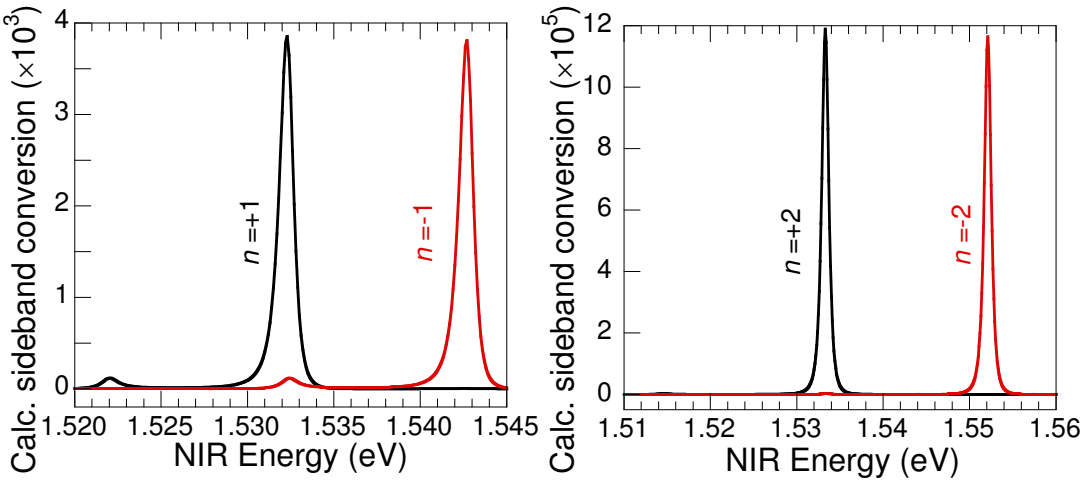

Figure 4.14: Calculated conversion efficiency for (a) $n = \pm 1$ and (b) $n = \pm 2$ sidebands at a THz field of 3 kV/cm. For $n = \pm 1$ sidebands, $\hbar\omega_{THz} = 10.4$ meV and $E_{bias} = 10$ kV/cm, while for $n = \pm 2$ sidebands, $\hbar\omega_{THz} = 9.4$ meV and $E_{bias} = 0$.

spective, this research is useful in further characterizing and improving all-optical wavelength conversion using THz EO modulation. The THz-optical mixing in this QW sample provides a voltage-controlled method of converting from one NIR wavelength to another. The conversion efficiency was measured and modelled as a function of NIR and THz frequency, bias voltage, and NIR and THz intensity. While the conversion efficiency was rather low in this sample, methods of improvement will be discussed in the next chapter.

This study also applies to fast QW modulators, used often in optical communications. These devices apply an oscillating electric field to a QW sample to modulate a NIR beam. The sideband measurements as a function of $\hbar\omega_{THz}$

as well as the modelling (see Fig. 4.12(c)) provide a connection between this low-frequency, quasi-static regime and THz modulation. It also establishes that improving modulation at high-frequencies can be achieved by tuning the excitonic intersubband transitions to the desired frequencies.

From a basic physics perspective, this research gives insight into two symmetries. First, the inversion symmetry of the QW was studied by applying a bias voltage. This symmetry completely controlled the generation of $n = \pm 1$ sidebands. Second, the symmetry between $n = \pm 1$ sidebands was observed. This symmetry was only expected for lossless media but was shown to occur in this system as long as the NIR intensity is low. The symmetry existed even for strong THz fields, which affected the exciton states.

Chapter 5

THz-optical mixing for wavelength conversion

This chapter will focus on research performed to improve THz-optical mixing for use in wavelength conversion. First, an introduction to wavelength conversion for optical communications will be given. Then, the multiple QW sample used to improve sideband conversion efficiency will be discussed along with the sideband results. These results demonstrate up to 0.2% conversion efficiency at 20 K with operation up to room temperature. Finally, analysis of the results will be presented along with a discussion of the suitability of this method for wavelength conversion.

5.1 Wavelength conversion

In a wavelength division multiplexed (WDM) optical communication network, data is carried over multiple wavelength "channels." It is necessary in an efficient network to switch data from one NIR wavelength to another when one wavelength channel is "busy" or to switch to a different communications band altogether. This can be accomplished by converting the modulated beam back into an an electrical signal, which is then used to modulate a beam at a new wavelength. This method tends to be slow and costly, so all-optical techniques are preferred.

All-optical wavelength conversion has been performed in many systems, including semiconductor optical amplifiers,[55, 56] semiconductor lasers,[57] optical fibers,[58] $LiNbO_3$,[59] and in bulk GaAs.[28] All-optical wavelength conversion using THz EO modulation has a few advantages over these methods. It is not limited in speed by gain and carrier dynamics, as are SOAs and lasers, and occurs in a system with strong nonlinearities that can be tuned by electric fields and band-gap engineering.

There are a number of other important factors to consider for effective wavelength conversion. First, the conversion efficiency from the input wavelength to the output wavelength should probably be greater than $\sim$1%. This output signal can be amplified to higher signal levels with little difficulty. The device should

also operate in the 1.3-1.5 μm range, where most optical communication networks operate. Sometimes the ∼850 nm range is used as well, particularly in radiation-hardened fiber. The device should probably operate at room temperature or at least within the range of a TE-cooler. Finally, for THz EO modulation, the device must use a compact THz source.

5.2 Sample design and characteristics

The sample used for this research was designed to improve the conversion efficiency and to demonstrate operation at room temperature. The sample (named SC4) consists of 50 periods of double GaAs QWs, nominally 100 and 120 Å wide and separated by a 25 Å $Al_{0.2}Ga_{0.8}As$ tunnel barrier (see inset of Fig. 5.1 and Appendix C). A large number of QWs was used to increase the interaction length, in an effort to increase the sideband conversion. Each pair of wells is separated by a 200 Å $Al_{0.3}Ga_{0.7}As$ barrier. The difference between the widths of the GaAs wells breaks inversion symmetry in the growth direction, allowing $n = \pm 1$ sidebands without a bias voltage. The tunnel splitting produces a spacing between electron subbands of ∼10 meV, well within the range of the FEL. These active QWs were grown in-between two doped gate QWs, but these gates were not contacted for the experiments discussed.

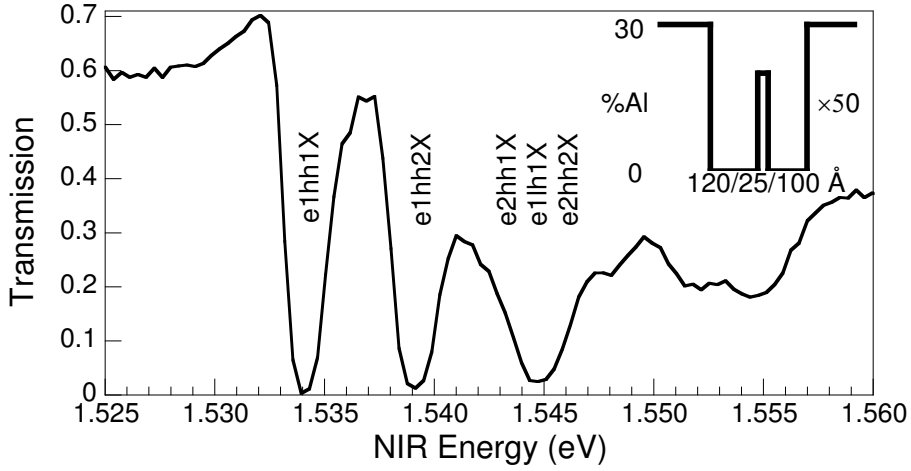

Figure 5.1: Transmission through SC4 at ∼20 K. The absorption lines are labelled by theory (see Ref. [30, 29]). The inset displays the conduction band profile of the QWs.

In the previous chapter, the QW sample was grown with a DBR behind the active QWs. However, the GaAs bandgap shifts strongly with temperature, while the DBR does not. In order to study the temperature dependence of the sideband generation, no DBR was grown. To allow transmission of the NIR beam, the sample was glued to sapphire and the semi-insulating GaAs substrate was etched away (See Appendix A for details). This left a 4-μm-thick epitaxial layer glued to sapphire, which included a 2.2-μm-active region, 0.7 μm of buffer layers, two doped gate QWs, and 1-μm-etch stop layer. The sample was then glued to another piece of sapphire so that the active region was in the middle of a dielectric waveguide. Figure 2.3 displays a diagram of the sample and the experimental geometry.

Figure 5.1 displays the transmission spectrum of the sample at low tempera-

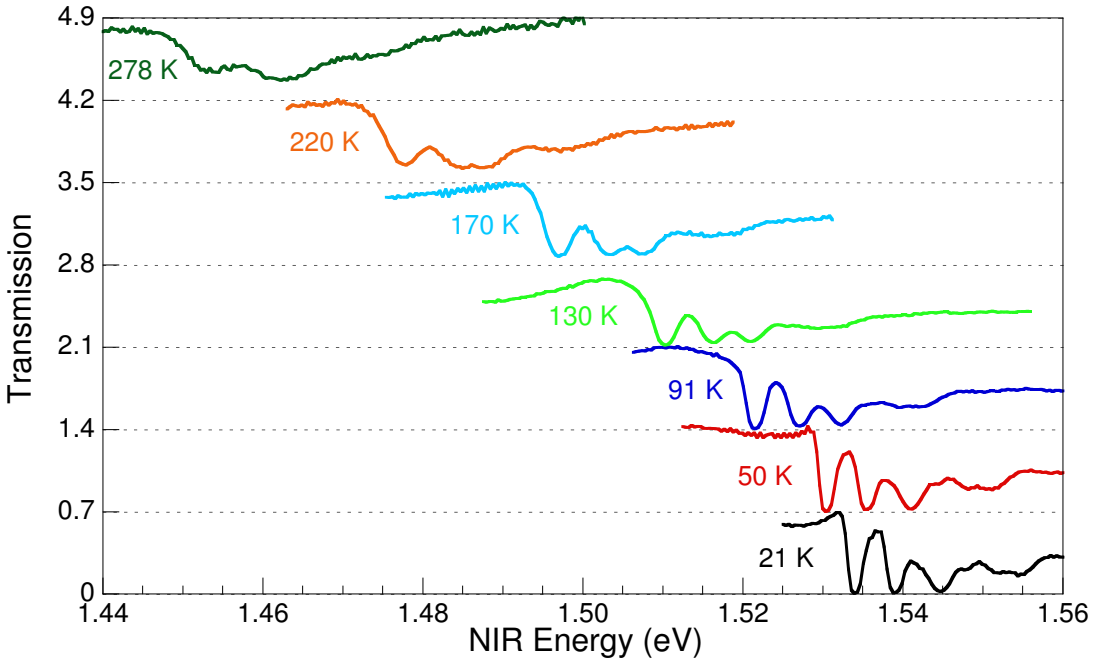

Figure 5.2: Transmission through SC4 at a series of temperatures from 21 K to 278 K. The curves are offset and labelled according to temperature.

tures. This spectrum is qualitatively similar to the PL spectrum measured in Ref. [29] since the QW structures are the same. The absorption lines in Fig. 5.1 are labelled according to calculations performed by Mark Su,[30] but there is some uncertainty in the upper states as there are so many nearly degenerate exciton states. The transmission of this sample was measured many times and was found to slowly redshift over the course of several months. This effect was likely due to strain in the thinned sample that changed over time and with thermal-cycling.

Figure 5.2 displays the transmission of SC4 at a series of temperatures from 21 K to 278 K. The absorption lines shifted to lower energies and became broader

at increasing temperatures as expected. There is also a decrease in the energy spacing between the second and third absorption lines. This effect could be due to changes in the hole effective mass with temperature.[4]

5.3 Results

Figure 5.3 shows a sideband spectrum of SC4 at low temperatures for $\hbar\omega_{THz} =$ 6.4 meV. With the laser at 1.54 eV, the $n = +1$ sideband was far stronger than the other sidebands with a conversion efficiency of ∼0.2%. This conversion efficiency was an order of magnitude higher than that using V5 or the sample used in Ref. [29]. The sideband spectrum was measured with an incident NIR intensity of ∼10 W/cm^2, so the sideband intensity was ∼20 mW/cm^2. The dependence on NIR intensity was linear for NIR intensities less than ∼50 W/cm^2. For a higher incident intensity of ∼160 W/cm^2, the sideband intensity saturated near 100 mW/cm^2. The increase in the saturation intensity compared to V5 in the previous chapter was likely due to the increase in QWs and the sharing of exciton oscillator strengths between the numerous exciton lines, resulting in fewer optically-excited carriers per well for a given intensity.

Sideband resonance spectra at $\hbar\omega_{THz} = 6.4$ meV are displayed in Fig. 5.4(b) for several THz powers, with a transmission spectrum above in (a) for comparison.

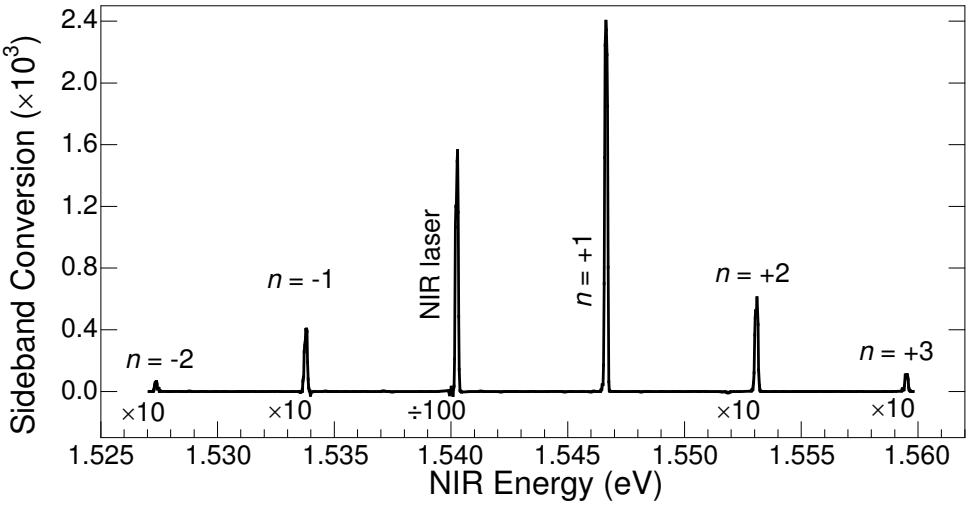

Figure 5.3: Transmitted sideband spectrum of SC4 at 20 K, taken at $\hbar\omega_{THz} = 6.4$ meV (1.5 THz). The transmitted beam at ω_{NIR} is divided by 100 and the $n = +3, +2, -1, -2$ sidebands are multiplied by 10 for clarity. The THz power was $\sim$1 kW and the NIR power was 0.2 mW.

(The dependence on power will be discussed later.) For each spectrum there was a sideband resonance at $\sim$1.537 eV (which appears to be split), in which the incident NIR frequency was resonant with e1hh2X and the sideband was nearly resonant with the upper absorption line. The splitting was actually due to the strong absorption of both the incident NIR beam and the sideband when on resonance. This will be modelled in the next section using a coupled wave equation model.

A complete discussion of the sideband resonances will not be given here as the resonances are already described for this QW structure in Ref. [29]. The resonances can be better understood by examining Fig. 5.5, which displays a sideband resonance map taken from Ref. [29]. The map was taken with $\hbar\omega_{THz} =$

8.2 meV, but the resonances were similar at $\hbar\omega_{THz} = 6.4$ meV. The resonances were labelled according to the exciton states involved in the sideband generation. The lowest resonance, e1hh1X-e2hh1X involved a change in the electron state, but the others involved changes in both electron and hole states. Taking a "slice" through Fig. 5.5 at 0 V should give a sideband resonance spectrum similar to that of SC4, so the main resonance in Fig. 5.4 should correspond to e1hh2X-e2hh1X. The resonance spectrum for SC4 seems to be shifted down in energy compared to that in Fig. 5.5, but this was expected since the exciton states in SC4 were at lower energies than those in Ref. [29]

Changes in the absorption due to strong THz fields modified the sideband resonances. Fig 5.6(a) displays the NIR transmission with and without a strong THz field. The absorption features redshifted, broadened, and absorbed less strongly when the THz field was on. The effects decreased as the THz field decreased but were qualitatively similar, as were changes measured at $\hbar\omega_{THz} = 5.5$ meV. This behavior was comparable to that observed in V5 with sapphire, as in Fig. 3.6. These changes were also manifest in the sideband resonance spectra in Fig. 5.4. The resonance spectrum redshifted, broadened, and the dip due to absorption became less significant at higher THz powers. This was due to the peak broadening and the decrease in absorption at these powers.

Some of the changes in transmission persisted after the FEL pulse was turned

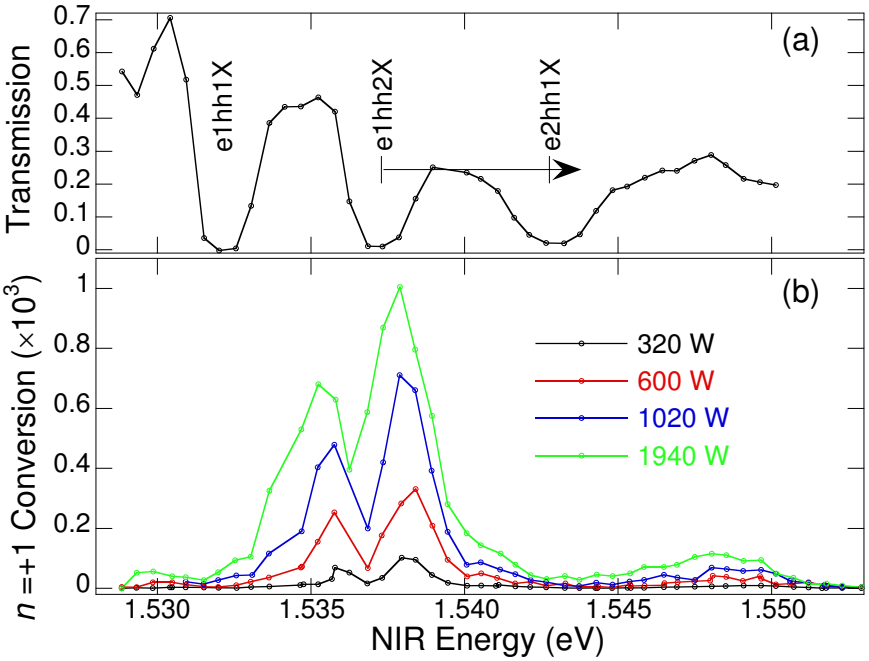

Figure 5.4: (a) Transmission spectrum of SC4 at 19.5 K using the Ti:sapphire laser. The arrow illustrates that the THz field is close to resonance with the e1hh2X-e2hh1X transition. (b) $n = +1$ sideband resonance spectra of SC4 at 19.4 K taken at a series of THz powers with $\hbar\omega_{THz} = 6.4$ meV. The spectra are labelled according to the THz power. The NIR power was ∼0.3 mW for (a) and (b).

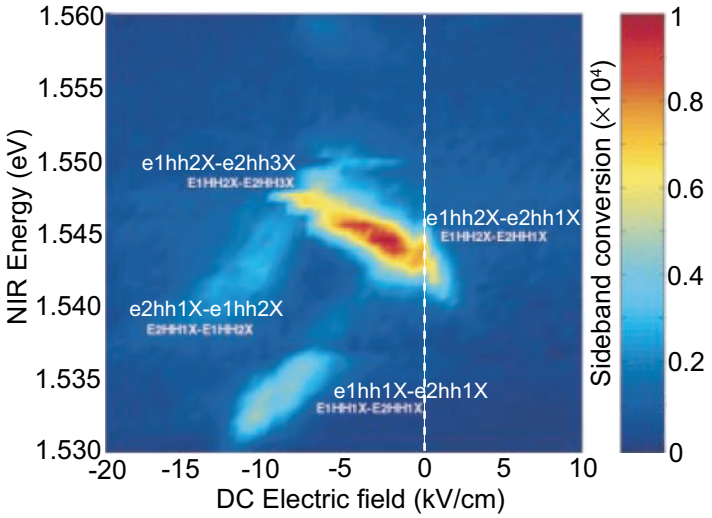

Figure 5.5: Sideband resonance map of a sample with the same QW structure as SC4 taken from Ref. [29]. The THz frequency was $\hbar\omega_{THz} = 8.2$ meV. The resonance labels have been rewritten above the originals for clarity. The white, vertical line designates the 0 V spectrum.

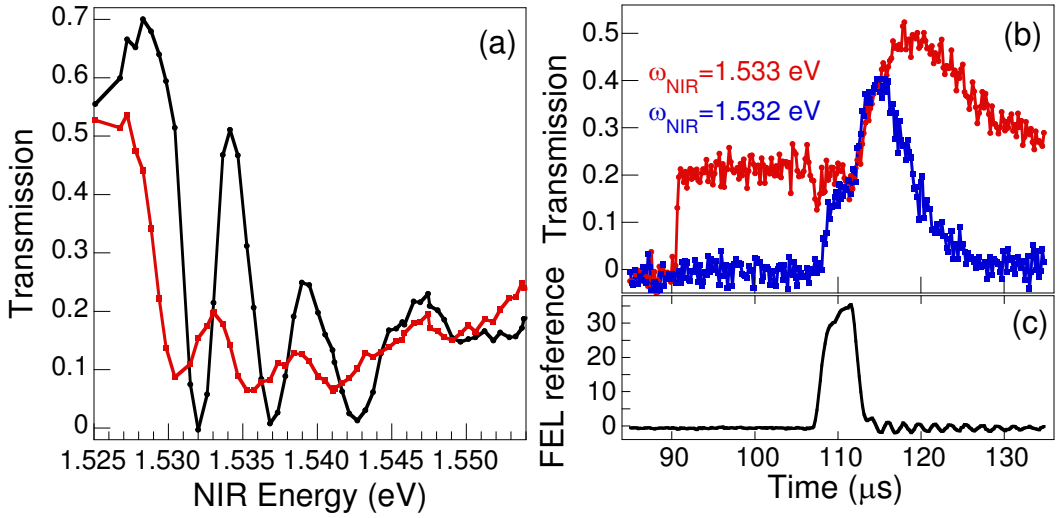

Figure 5.6: (a) Transmission through SC4 at 20 K with the THz field at $\hbar\omega_{THz} = 6.4$ meV (red) and without the THz field (black). The THz power was ~2 kW. (b) Transmission as a function of time at $\hbar\omega_{NIR} = 1.532$ eV (blue) and $\hbar\omega_{NIR} = 1.533$ eV (red). (c) THz reference signal vs. time.

off, as displayed in Fig. 5.6(b) and (c). This indicated that the sample was heated during the FEL pulse. The heating effects could not be well-separated from the strong-field effects, making a detailed understanding of the changes in transmission impossible. The persistent heating effect did not come from photogenerated carrier heating as the effect had very little dependence on NIR power. Heating of carriers from residual extrinsic doping, or of the GaAs or sapphire lattice directly by the THz field could be the cause. This persistent effect was strong in samples with substrates removed, like the one studied here. Poor thermal conduction from the epitaxial layer to the sapphire likely makes any heating effects more noticeable.

Sidebands were also measured as a function of temperature. Figure 5.7 displays sideband resonance spectra at a series of temperatures from 20 K to 240 K, and Fig. 5.8 shows a room temperature sideband resonance spectrum. The sideband resonance shifted to lower NIR energies with increasing temperatures, following the shifts in the absorption lines. The sideband signal also decreased with increasing temperature, but the magnitude of the decrease varied from one day to another. This variation was likely due to thermal cycling, which also produced irreversible changes in the optical spectrum. However, compared to 20 K, the sideband conversion of this sample decreased by not more than a factor of 3 at 100 K and by not more than a factor of 10 at 200 K. The decrease in conversion was primarily due to the increasing exciton linewidths, indicating increasing

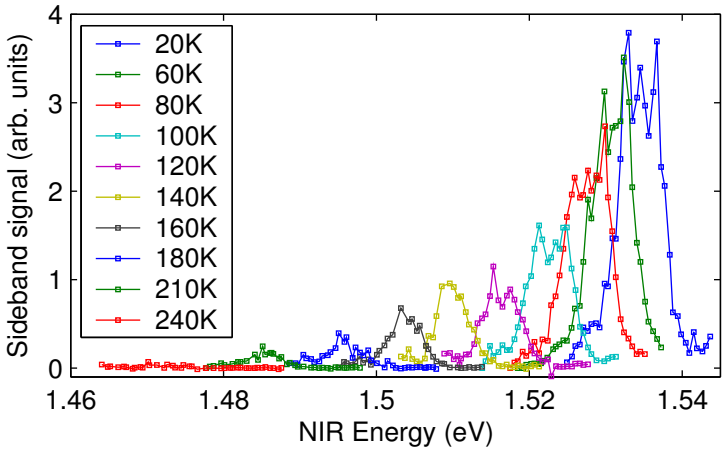

Figure 5.7: $n = +1$ sideband resonance spectra of SC4 at a series of temperatures using $\hbar\omega_{THz} = 6.4$ meV. The THz power was ∼1 kW, and the NIR power was ∼0.2 mW. The spectra have been corrected for variations in the laser power and the PMT response.

dephasing and decreasing peak nonlinear susceptibility. The decreased spacing between e1hh2X and e2hh1X for higher temperatures, as seen in Fig. 5.2, may have had an impact as well. For this reason, the room temperature resonance spectrum was taken with a lower THz frequency. Additionally, while the sapphire is transparent to THz frequencies at low temperatures, it is absorbing ($\alpha \sim 3$ cm^{-1}) at high temperatures.[60] This could have decreased the THz field in the sample at higher temperatures.

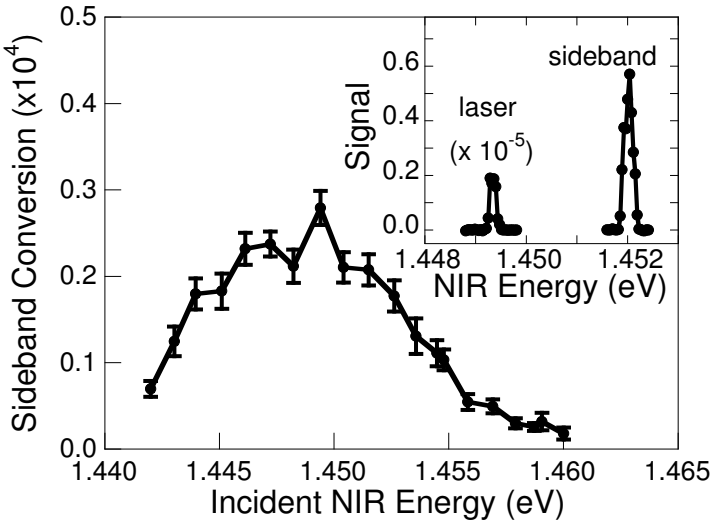

Figure 5.8: $n = +1$ sideband resonance spectrum of SC4 at 295 K using $\hbar\omega_{THz} = 2.7$ meV. The THz power was ∼6 kW, and the NIR power was ∼3.2 mW. The inset graph displays the sideband spectrum with $\hbar\omega_{NIR} = 1.4493$ eV.

5.4 Analysis

The purpose of using a sample with 50 QWs was to improve the sideband conversion efficiency for wavelength conversion, but there was some question as to how well this would work due to the increase in QW absorption. In order to analyze the effect of absorption on the sideband generation, the coupled wave equations were used to propagate the sideband and incident laser through the sample as a function of wavelength and thickness. Strictly speaking, these equations apply to a bulk nonlinear medium, but they are often used successfully with QWs.[33, 61] The equations are derived in Appendix D and include the nonlinear susceptibility and absorption loss. If phase-matching is ignored and the absorption of the

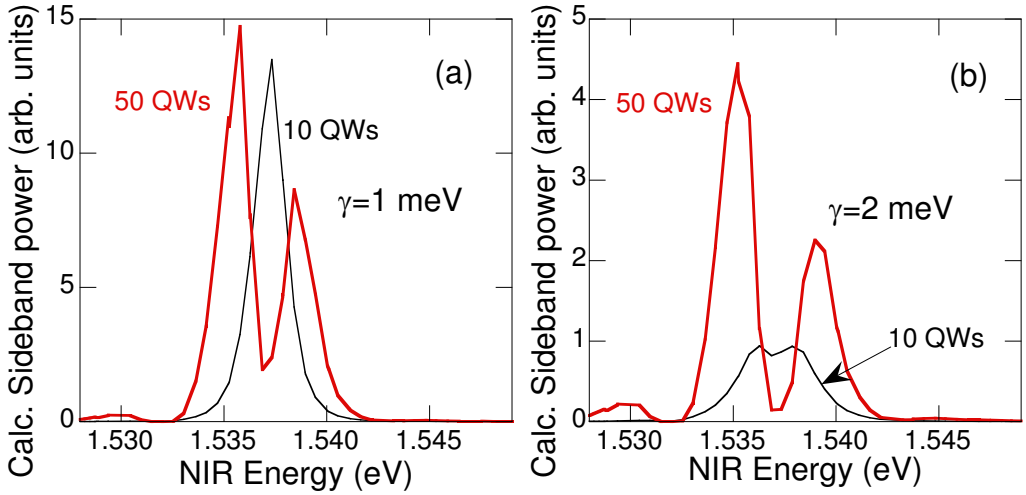

Figure 5.9: Simulated sideband signal taking into account absorption for 10 QWs (black) and 50 QWs (red) at (a) $\hbar\gamma = 1$ meV and (b) $\hbar\gamma = 2$ meV. The sideband signal units are arbitrary but are the same for (a) and (b). The absorption was obtained from a transmission spectrum, which gave a value of $\sim$1.5 μm^{-1} on the e1hh2X line.

sideband and the incident NIR beam are assumed to be the same, Eq. (D.18) can be simplified to $\tilde{E}_{SB}(z) \propto z\exp(-\alpha z)$, which has a maximum at $z = \alpha^{-1}$ (z is the position in the sample in the propagation direction). This means that the sideband signal should decrease when the NIR transmission drops below 13.5%.

Fig. 5.9 displays the simulated sideband resonance spectra for two values of z, taking into account absorption. The black lines correspond to 10 QWs (as in previous work) and the red lines correspond to 50 QWs (as in SC4). The spectra were obtained using Eq. (D.18) ignoring phase-mismatch and using an excitonic intersubband resonance term from Eq. (4.8) ($\nu = 1$, $n = 2$) for $\chi^{(2)}$. The absorption $\alpha(\omega)$ was obtained from a transmission spectrum of SC4. Fig. 5.9(a)

used $\gamma = 1$ meV in $\chi^{(2)}$, while (b) used $\gamma = 2$ meV. The large dip in the sideband resonance at the e1hh2X line ($\hbar\omega_{NIR} = 1.537$ eV) is apparent in both. On the absorption line, the calculated sideband signal decreased with a larger interaction length, but the off-resonance value increased. Whether or not the peak sideband signal increased with interaction length in this model depended on the value of γ used in $\chi^{(2)}$. For $\gamma = 1$ meV, Fig. 5.9 shows that the peak value stayed roughly the same, while for $\gamma = 2$ meV, the peak increased by a factor of $\sim$5. This difference occurred because $\chi^{(2)}$ fell off more quickly away from the exciton line using the smaller value of γ, making off-resonance sideband generation less effective. The $\gamma = 1$ meV graph is likely more accurate because the half-width-half-max of the NIR absorption was $\sim$1 meV, and the simulated sideband resonance more closely matches the experimental curves in Fig. 5.4. This implies that increasing the number of QWs to 50 *may* not have increased the sideband conversion efficiency very much due to the strong absorption on resonance. Other factors, such as the THz coupling, may have had a significant effect.

The more sophisticated model of $\chi^{(2)}$ developed in Chapter 4 can be used along with Eq. (D.18) (including phase-mismatch) to simulate the sideband signal for square QWs. The results are displayed in Fig. 5.10. In this case, the sideband signal continues to increase even for 600 QWs and there is no splitting. This is in part because there is only significant NIR absorption at the e1hh1X line. For

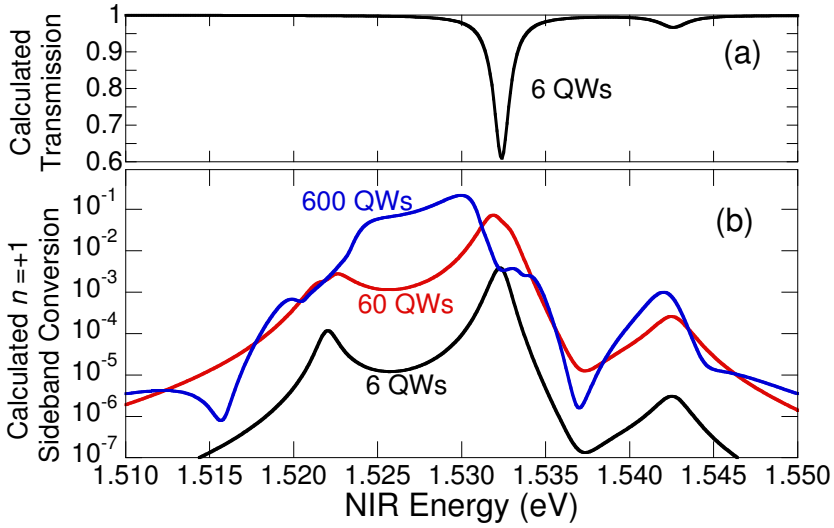

Figure 5.10: (a) Calculated transmission spectrum of a 6 square QW sample at $E_{bias} = 10$ kV/cm. (b) Simulated $n = +1$ sideband conversion (log scale) from a square QW for 6 QWs (black), 60 QWs (red) and 600 QWs (blue). $E_{THz} = 3$ kV/cm and $\hbar\omega_{THz} = 10.4$ meV. The model used to calculate conversion efficiency in V5, shown in Fig. 4.14 was used.

$\alpha(\omega_{SB}) = 0$, Eq. (D.18) gives $\tilde{E}_{SB}(z) \propto 1 - \exp(-\alpha(\omega_{NIR})z)$, which leads only to sideband saturation for large interaction lengths. For a sample with more than 600 QWs, the peak sideband signal does saturate and even decreases as absorption at the sideband energy becomes significant. A more realistic model of the inter-band absorption may cause this saturation to occur for fewer QWs. Nevertheless, multiple square QW structures appear to show promise for improving sideband conversion efficiency.

5.5 Summary

THz-optical mixing in a GaAs multi-quantum well sample has been studied for application to wavelength conversion. Sidebands were generated with a conversion efficiency up to 0.2%. This efficiency should be sufficient to be regenerated to full power by optical amplifiers, and is also comparable to efficiencies achieved in wavelength converters based on SOAs[56] or semiconductor lasers.[57] By comparison, a 4-μm-thick $LiNbO_3$ sample in the same experimental conditions should have a conversion efficiency of $\sim 3\times 10^{-8}$, assuming an EO coefficient of 9.6 pm/V.[62].

The improvement in conversion efficiency over previous work is partly attributed to the increased number of QWs. However, modelling of the sideband generation with the coupled wave equations demonstrated that the strong interband QW absorption in this sample may have caused the peak sideband signal to saturate. Other factors, such as the THz coupling, may have had more of an effect in improving the sideband conversion.

Our device operated from 20 K up to room temperature, but had significantly decreased conversion efficiency at higher temperatures. This could be overcome by improving the THz coupling and perhaps by using a square QW sample. This device could easily be made voltage-controlled, as the devices in Chapter 4, and could be implemented in InGaAs wells on InP for operation at 1.55 μm. Recently

developed THz quantum cascade lasers[63] have, inside their cavities, THz fields comparable to the several kV/cm fields used for these experiments.[64] Thus, all-semiconductor THz EO wavelength converters with integrated THz sources may be achieved in the future.

Chapter 6

THz-optical mixing in doped quantum wells

All of the previous research on THz-optical mixing has focused on undoped QWs. The interband spectra of undoped QWs are simpler, and the sample design is easier. There has also been an expectation that sideband generation should be much weaker in doped QWs due to Pauli blocking of interband transitions and wider linewidths. This chapter presents a detailed study of THz-optical mixing in n-doped GaAs QWs and compares the results to those in undoped QWs.

Sideband generation in doped QWs was comparable in strength to that in undoped QWs but was quite different in other ways. Excitonic effects were largely screened by the electron gas, and the THz field could drive real, electronic, in-

tersubband transitions. When the THz frequency was near the intersubband transition frequency, only one broad sideband resonance occurred, as opposed to the many sharp excitonic intersubband resonances in the undoped samples. This indicates that THz-optical mixing in doped QWs is primarily sensitive to electronic intersubband transitions and can be used to probe the coherent dynamics of electrons, particularly in strongly driven systems. The results can be explained qualitatively by a nonlinear susceptibility model.

6.1 Sample design and characteristics

Sample design and characterization was challenging for the doped QW samples. Typically for intersubband absorption experiments, the cleanest design is to only grow a single, doped QW. The charge density in the QW can then be varied (and measured) by applying a voltage to a Schottky gate. A single, doped QW sample was grown, but the interband absorption and sideband generation were too small to measure. A number of multiple doped QW samples were grown, which were less simple to understand and characterize but much more successful for sideband generation. Each consists of 10 periods of double GaAs QWs, with the same QW structure as SC4 (100 and 120 Å wide wells separated by a 25 Å $Al_{0.2}Ga_{0.8}As$ tunnel barrier). The focus of this chapter will be on a doped sample called SC9 and

an undoped reference sample called SC5. Figure 6.1 displays the layer structure of SC9. (SC5 has the same basic structure but with no doping near the active wells. See Appendix C for complete structures.) In the undoped sample, each pair of wells is separated by a 410 Å $Al_{0.3}Ga_{0.7}As$ barrier. In the doped sample, each pair of wells is separated by a 920 Å barrier, with Silicon δ-doping at the center. Having a significant spacer between the doping layer and the QW prevents localization of charge in the QW by impurities. The spacing between wells also maximizes interaction with the NIR beam, as described in Section 2.1.2. All of these active QWs were grown in-between two doped, 70 Å wide gate QWs, with a DBR underneath.

The charge density in the doped sample was measured by capacitance-voltage (CV) measurements. The CV sample was fabricated by etching ∼5000 Å over the whole sample, etching a large mesa, annealing Indium contacts to the active QW layers, and depositing an Al Schottky gate over the mesa. (See Section 2.2.3) Figure 6.2 displays the CV curve, which had a series of steps. All of the active QWs were shorted together by the In contact, but the QW closest to the gate screened the other QWs. Once the closest QW was depleted, the capacitance to the next QW was measured, and so on. The steps occurred due to the greater distance between the gate and the next QW. The charge density in each well was determined by integrating the capacitance over each plateau and dividing by the

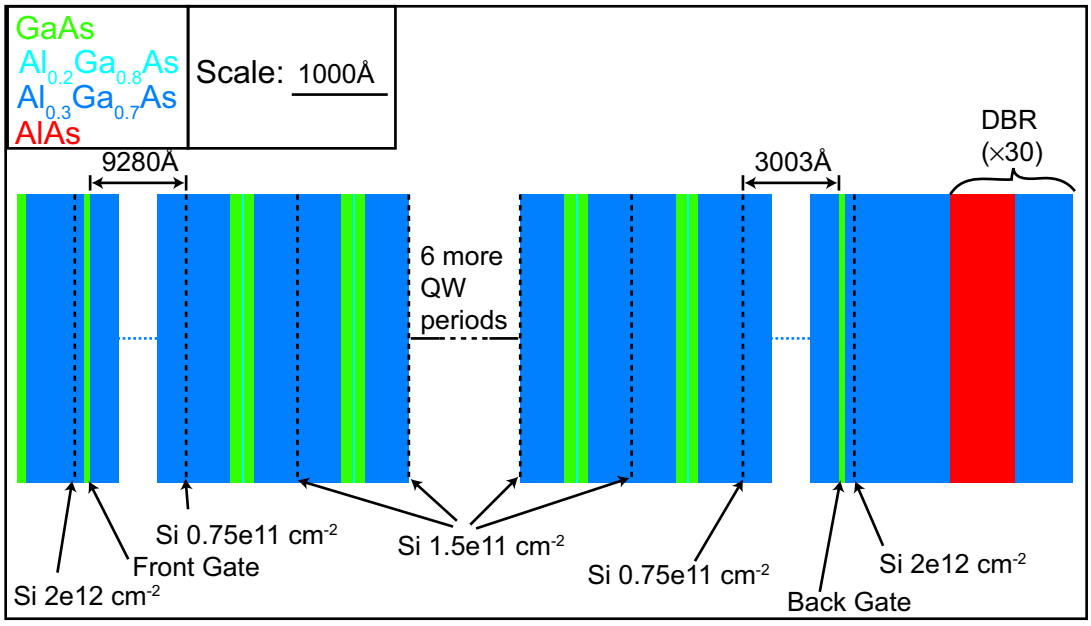

Figure 6.1: Sample structure of SC9.

gate area. The result was $\sim 1.2\times10^{11}$ e/cm^2 for each well except the first. The fact that the first step occurred so close to 0 V indicated that the closest QW was significantly depleted by surface states. This depletion should not have been an issue when the front gate QW was present. However, even with the front gate QW, the charge density in the outer QWs was almost certainly different than the inner QWs based on simulations.

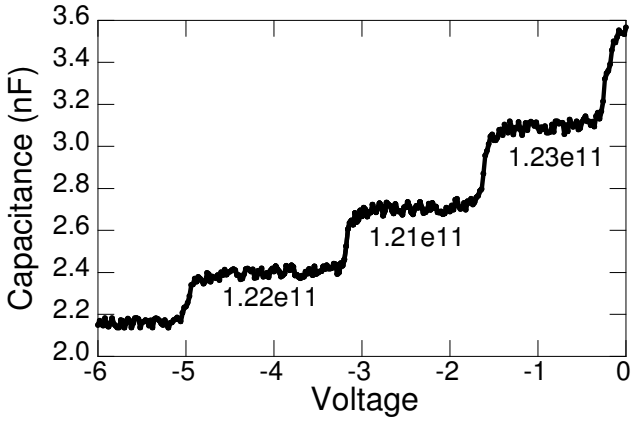

Figure 6.2: Capacitance-voltage measurement on SC9, displaying the sequential depletion of the active QWs. The numbers indicate the calculated charge density (e/cm^2) in each QW.

6.1.1 Interband characteristics

The PL and reflectivity of the two samples are shown in Fig. 6.3. In the undoped sample (Fig. 6.3(a)) there was sharp PL from the lowest state, ehh1X, and a number of sharp exciton absorption lines, similar to the spectrum observed in Ref. [29]. The lines are labelled by theory.[30] In the doped sample (Fig. 6.3(b)), the absorption was much broader as continuum absorption played more of a role due to exciton screening.[65] Assigning transitions to the resonances was not practical due to this broadening, but the lowest energy absorption must still have been due to the $hh1 \rightarrow e1$ transition. The PL was also much broader as electrons from the Fermi energy to the bottom of the conduction band could recombine with holes. This filling of the conduction band also resulted in a small blueshift of the

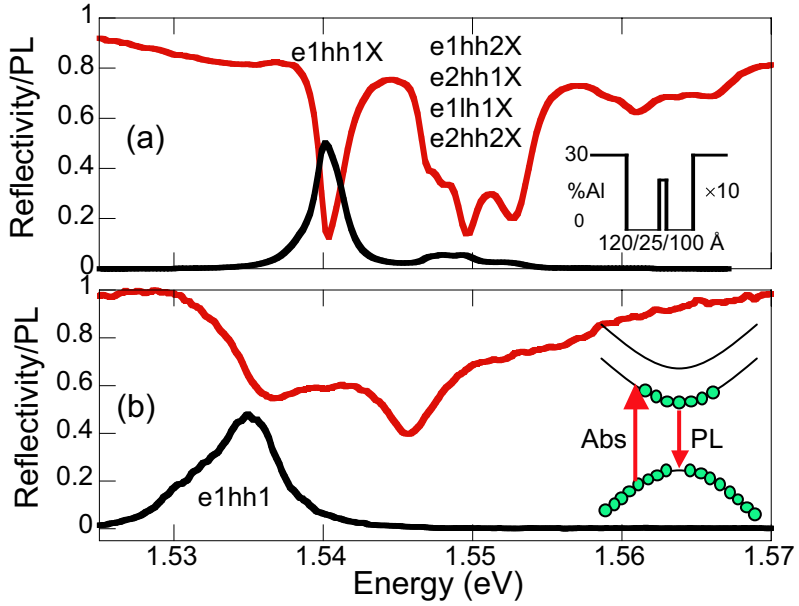

Figure 6.3: PL (black) and reflectivity (red) of the (a) undoped sample SC5 and (b) doped sample SC9 at zero bias taken at ∼11 K. For PL, the samples were excited at 777 nm with an intensity of ∼9 W/cm^2 for the undoped sample and ∼30 W/cm^2 for the doped sample, and both were normalized to 0.5. The inset in (a) displays the QW profile, and the inset in (b) is a diagram illustrating the shift between absorption and PL in the doped sample.

absorption edge relative to the PL. The diagram inset in Fig. 6.3(b) illustrates this effect. The obvious shift in PL between the doped and undoped samples may have been due to band gap renormalization.[66]

Figure 6.4 displays reflectivity maps for the undoped and doped samples, taken by measuring the reflectivity at a series of gate voltages. The gate voltage was pulsed in this measurement and in sideband measurements to avoid heating and tunnelling of carriers between wells. The map for the undoped sample was qualitatively similar to the PL map in Ref. [29] and shows the tuning of the exciton

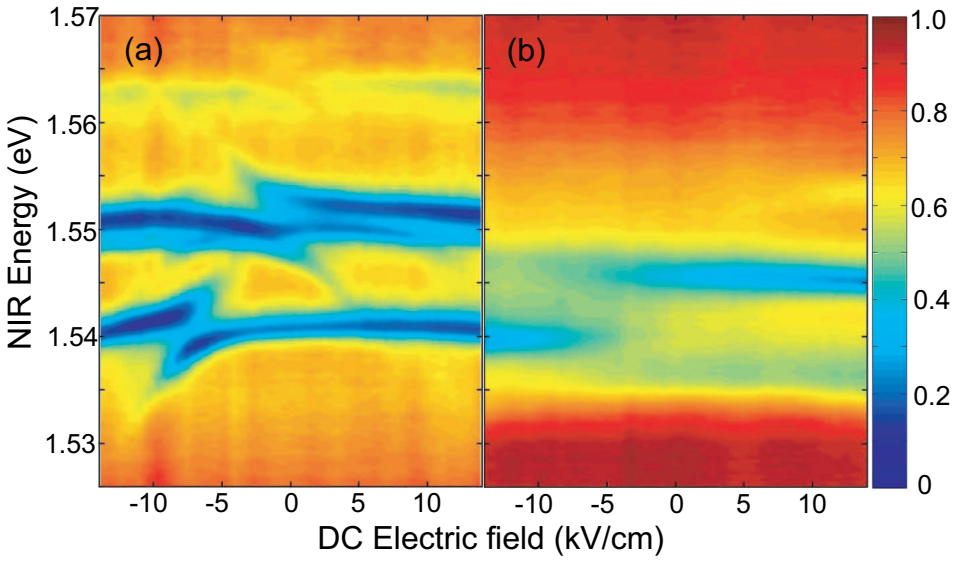

Figure 6.4: Reflectivity maps of (a) the undoped sample SC5 at ∼11 K and (b) the doped sample SC9 at ∼12 K obtained by taking reflectivity scans at a series of gate voltages. The reflectivity for each point is represented on a color scale, displayed on the right. Spectra were taken using an LED.

levels. In the doped sample, the interband absorption strength changed with electric field, but the interband energies changed very little. Screening of the electric field by the electron gas was likely the cause.

6.1.2 Intersubband characteristics

In the doped sample, the intersubband absorption was measured as a function of dc electric field using FTIR spectroscopy. These measurements required a reference spectrum in order to eliminate the instrument response. The reference is typically obtained by depleting the QW, but this was not possible for a 10 QW

sample. Instead, a large positive voltage was applied between the front and back gates, which was predicted to decrease the intersubband absorption and shift it to much higher energies. The results are displayed in Fig. 6.5. Fig. 6.5(a) displays FTIR transmission spectra for a series of voltages, normalized by a spectrum at +3.0 V. The absorption was fairly strong, as expected for 10 QWs, but was relatively broad ($\sim$1.5 meV) and seemed to consist of more than one absorption line. The absorption frequency at +2.0 V did not shift very far out of the way, making it unlikely that the +3.0 V spectrum was a very good reference. Another issue was that the spectra were not entirely reproducible. Shifts and changes in shape would occur, depending on how long the voltage was applied. One possibility is that electrons were not entirely localized to the QWs. Small "puddles" of charge might form and move in response to the field, or electrons might tunnel from one well to another. This behavior was not observed in PL/reflectivity or in sideband measurements, probably because the voltage was pulsed for only $\sim$60 μs. These types of measurement with biased multiple QWs have been performed,[67, 68] presumably without such difficulties. Perhaps following designs from these references would give improvements. Despite these measurement problems, we did obtain the approximate intersubband absorption frequency and found that it changed with applied voltage. The approximate energy of the intersubband absorption is plotted in Fig. 6.5(b) as a function of the applied field (solid dots). (The absorp-

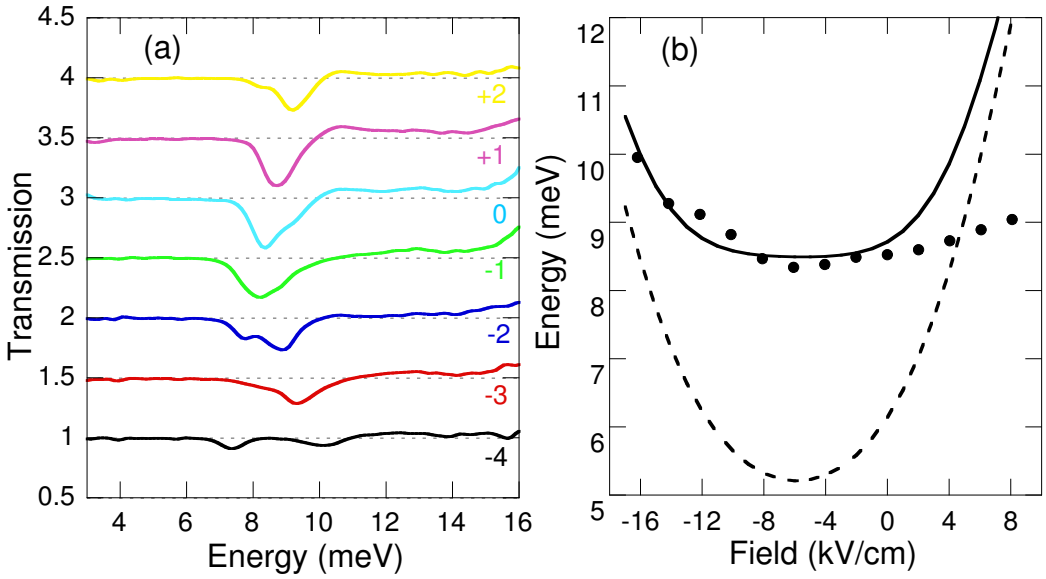

Figure 6.5: (a) FTIR transmission spectra of SC9 for a series of gate voltages, offset and labelled according to the gate voltage. An FTIR spectrum at +3.0 V was used as the reference. (b) Intersubband absorption frequency vs. dc electric field. The circles represent the frequencies determined experimentally. The solid line and the dashed line represent the calculated dressed and bare intersubband frequencies, respectively.

tion dip at ∼7.5 meV for the -4 V spectrum was ignored as it did not seem to tune with voltage.)

Coulomb interaction and collective excitations

With the significant charge density in these relatively wide QWs, the Coulomb interaction between electrons strongly modifies the potential well along with the subband energies.[7] The Coulomb interaction can be taken into account in the Schrödinger equation by including a Hartree term, V_H, and an exchange-correlation

term, V_{xc}, which are both functions of the electron density, $n(z)$. The Schrödinger equation can then be written as

$$\left[-\frac{\hbar^2}{2m^*}\frac{d^2}{dz^2} + V(z) + V_H(n_0(z)) + V_{xc}(n_0(z))\right]\varphi_n(z) = E_n\varphi_n(z), \tag{6.1}$$

where

$$n_0(z) = \sum_i n_i \left|\varphi_i(z)\right|^2. \tag{6.2}$$

The areal electron concentration of the ith subband, n_i, is determined by Fermi statistics. Equation (6.1) must be solved self-consistently with Poisson's equation,

$$\frac{\partial^2\Phi}{\partial z^2} = \frac{e}{\epsilon}n(z), \tag{6.3}$$

where $V_H = -e\Phi$. This self-consistent calculation was performed for the QW structure of SC9 for a series of dc electric fields using a program written by Brian Galdrikian. The intersubband spacing from these calculations is plotted in Fig. 6.5(b) (dashed line). In these calculations, the tunnel barrier was made 12% wider to better fit the experimental data. The $Al_{0.3}Ga_{0.7}As$ and $Al_{0.2}Ga_{0.8}As$ conduction band offsets used were 300 meV and 200 meV, respectively.

The Coulomb interaction also modifies the dynamics of the QW, such that a driving field induces collective excitations of the electron gas. The frequency of this collective excitation, called the "dressed" frequency, is said to be depolarization shifted from the "bare" intersubband frequency. The dressed frequency

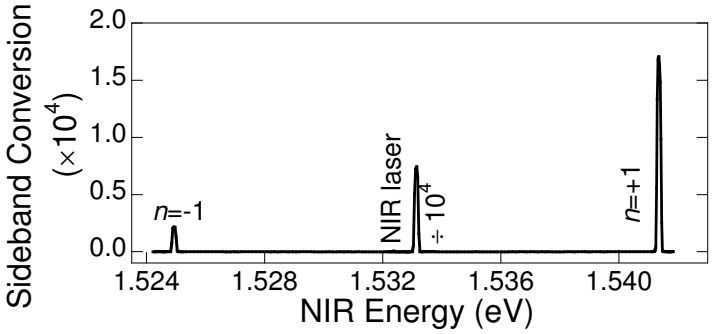

Figure 6.6: Sideband spectrum of SC9 taken at ∼11 K with $\hbar\omega_{THz} = 8.2$ meV at ∼730 kW/cm^2. The NIR laser signal is divided by $\sim 1 \times 10^4$. $E_{bias} = 5.8$ kV/cm.

was calculated in Brian Galdrikian's program as well, and is plotted in Fig. 6.5(b) (solid line), along with the measured absorption. The measured absorption should match up with the dressed frequency. The disagreement between the two at positive voltages is not well understood, but the sample is still tuning at these voltages.

6.2 Sideband results

Sidebands were measured on the undoped and doped samples with ITO-coated glass pressed onto the sample frontside, in the geometry displayed in Fig. 2.1(b). Fig. 6.6 shows a typical sideband spectrum for the doped sample, with $\hbar\omega =$ 8.2 meV, quite close to the intersubband absorption frequency. The conversion efficiency was measured to be $\sim 1.7 \times 10^{-4}$. This was the same order of magnitude conversion efficiency as in the undoped sample. Higher order sidebands ($n = \pm 2$) were extremely small under these conditions.

Sideband generation was strongest for both samples when the NIR and THz frequencies were resonant with interband and intersubband transitions, respectively. The resonant structure can be examined by plotting sideband resonance maps. The $n = +1$ sideband resonance maps are displayed in Fig. 6.7 for (a) the undoped and (b) doped samples. Scanning E_{bias} varies the intersubband frequency, bringing it into resonance with ω_{THz}, while scanning ω_{NIR} brings it into resonance with interband transitions. There were several sharp excitonic resonances for the undoped sample, quite similar to those in Ref. [29] (see Fig. 5.5) since the QW structures are identical. The lower-energy resonance only involves a change in electron state while the other resonances involve hole transitions. In the doped sample, only the resonance involving electron transitions remained significant. The resonance was much broader in NIR frequency as it involved continuum states instead of exciton states, and was broader in E_{bias} as the intersubband tuning is screened somewhat by the electron gas.

Figure 6.8 displays the dependence of the $n = +1$ sideband signal on (a) the NIR intensity and (b) the THz intensity. For the doped sample, the sideband intensity when on resonance at $\hbar\omega_{NIR} = 1.531$ eV increased linearly with NIR intensity up to the highest NIR intensity available ($\sim$1500 W/cm^2). While at $\hbar\omega_{NIR} = 1.537$ eV, saturation began at $\sim$100 W/cm^2. This difference occurred because the sideband resonance in the doped sample was just below the absorption

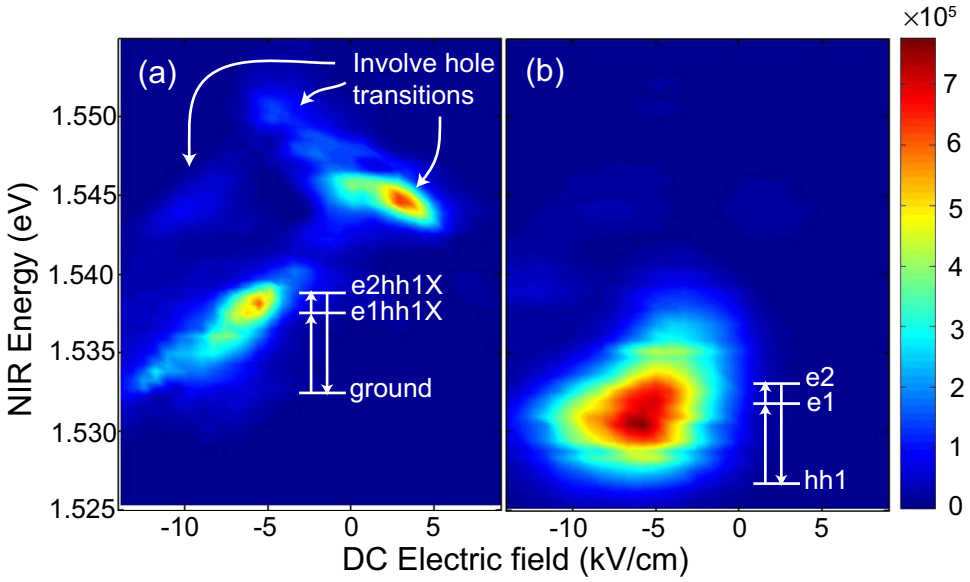

Figure 6.7: The $n = +1$ sideband resonance maps of (a) the undoped and (b) doped samples at $\hbar\omega_{THz} = 8.2$ meV. The sideband conversion for each point is represented on a color scale, displayed on the right. The maps were taken at ∼12 K with a THz intensity of ∼18 kW/cm^2 and a NIR intensity of ∼25 W/cm^2.

edge, so very few carriers were generated. While at $\hbar\omega_{NIR} = 1.537$ eV, the interband absorption is strong. Sidebands in the undoped sample saturate near $\sim$100 W/cm^2 on resonance since the absorption is quite strong on the sideband resonance. As a function of THz intensity, both undoped and doped samples began to saturate at $\sim$80 kW/cm^2. This is a surprisingly high saturation intensity for the doped sample since resonant intersubband absorption has been shown to start saturating at only $\sim$1 W/cm^2.[69]

Valuable information can be obtained by measuring the sideband signal as a function of ω_{THz}. Figure 6.9(a) displays the $n = +1$ sideband resonance spectra at a series of THz frequencies. These spectra were taken with $E_{bias} = -5.8$ kV/cm, where the intersubband absorption was measured to be at $\sim$8.3 meV (see Fig. 6.5(b)). The resonance scan at 8.2 meV was closest to this frequency and had only a single resonance centered below the PL peak, despite the many interband absorption features at higher energies, shown in Fig. 6.9(b). Resonance scans near 8.2 meV and at higher ω_{THz} had only one significant resonance that redshifted as ω_{THz} increased. For lower ω_{THz}, there were several resonances at higher NIR energies. The inset of Fig. 6.9(a) plots the peak of each sideband resonance scan as a function of ω_{THz}, showing the resonance at the intersubband absorption frequency and a significant low frequency response. This behavior is similar to that observed in the undoped square well sample (see Fig. 4.12(c),

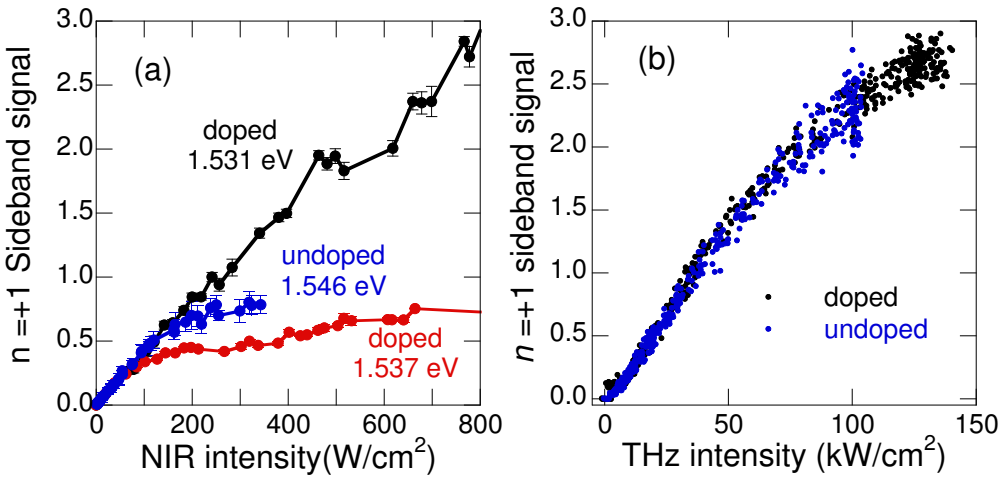

Figure 6.8: (a) Dependence of the $n = +1$ sideband signal on the NIR intensity. The black and red curves are for the doped sample at $\hbar\omega_{NIR} = 1.531$ eV (on the sideband resonance) and $\hbar\omega_{NIR} = 1.537$ eV (strong interband absorption), respectively. The blue curve is for the undoped sample on resonance at $\hbar\omega_{NIR} = 1.546$ eV. The doped sample was at -1.4 V (pulsed) at ∼12 K, and the undoped sample was at 0 V at 21 K. (b) Dependence of the $n = +1$ sideband signal on the THz intensity (estimated just outside the sample). The black and blue curves are for the doped and undoped samples, respectively. The doped sample was at -1.4 V (pulsed) at 15 K, with $\hbar\omega_{NIR} = 1.531$ eV. The undoped sample was at -0.8V (pulsed) at ∼11 K, with $\hbar\omega_{NIR} = 1.538$ eV. The THz frequency was 8.2 meV for both samples. In both (a) and (b) the graphs were all normalized to the same value at low intensities.

page 106). These trends show the interplay between sidebands due to the collective excitations of the electron gas and those due to interband processes.

6.3 PL Quenching

Sideband generation is a measure of the coherent response of the QW to the THz field. The incoherent response was probed by measuring the change in PL when the THz field was present. The effect at $\hbar\omega_{THz} = 8.2$ meV is displayed in Fig. 6.10(a). The electron gas was heated up by the THz beam, quenching the PL and shifting the Fermi distribution as seen in similar systems.[70, 11] Figure 6.10(b) displays the percent change in the integrated PL as a function of the THz frequency. A single resonance near the intersubband absorption is visible, as would be expected when the dominant heating mechanism is intersubband absorption.

6.4 Model and Discussion

A qualitative understanding of THz-optical mixing in the doped sample can be obtained from a $\chi^{(2)}$ model. We will only consider three subbands: hh1, e1, and e2. This approximation makes sense since the sideband resonance spectra with $\omega_{THz} > 5.5$ meV have one dominant resonance near the e1-hh1 transition. We will

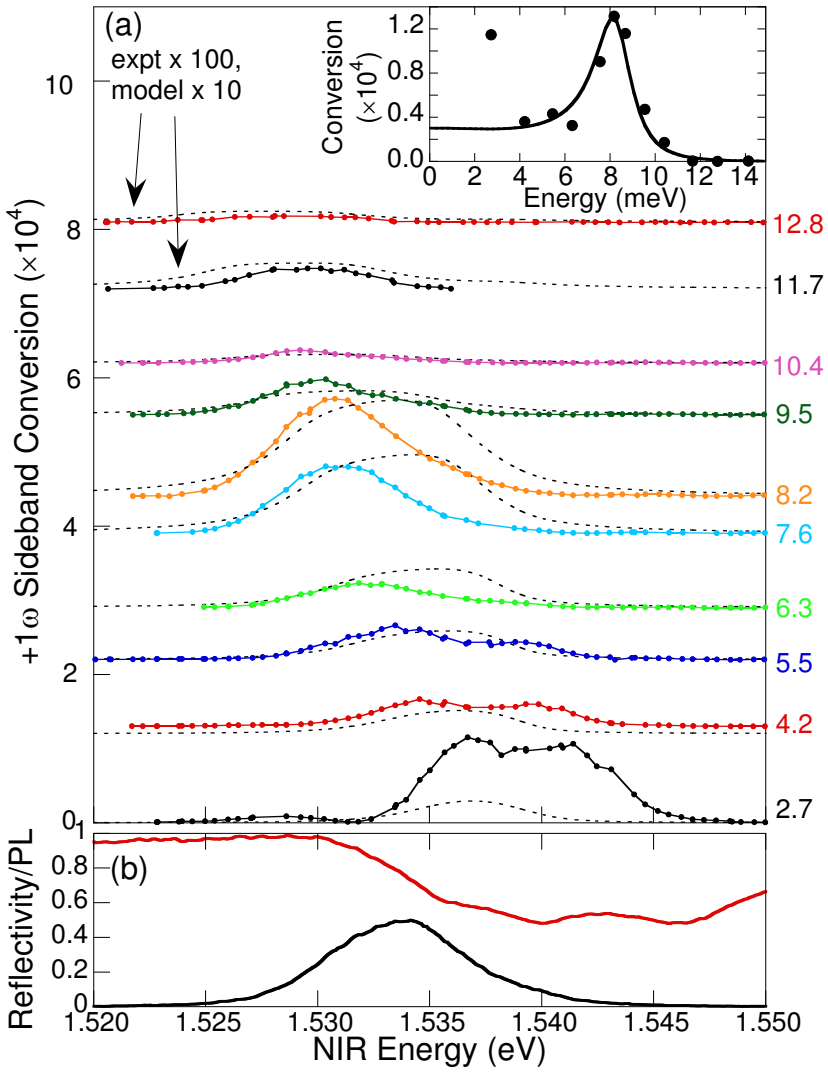

Figure 6.9: (a) The $n = +1$ sideband resonance spectra (solid dots and lines) of the doped sample for a series of THz frequencies, all with intensities near 40 kW/cm^2. The temperature was between 11 and 16 K, and E_{bias} was at -5.8 kV/cm. The NIR intensity was ∼30 W/cm^2 except for $\hbar\omega_{THz} = 11.7$ meV and 12.8 meV, where the intensity was raised to ∼240 W/cm^2. The spectra are vertically offset and labelled according to ω_{THz}. $\chi^{(2)}$ model calculations (dashed lines) are plotted for comparison. Experimental (calculated) spectra at $\omega_{THz} = 11.7$ and 12.8 meV are multiplied by 100 (10) for clarity. The inset graph plots the maximum of each resonance spectrum (solid circles) as a function of ω_{THz} along with the model values (solid line). (b) Low-temperature reflectivity and PL of the doped sample at $E_{bias} = 5.8$ kV/cm for comparison.

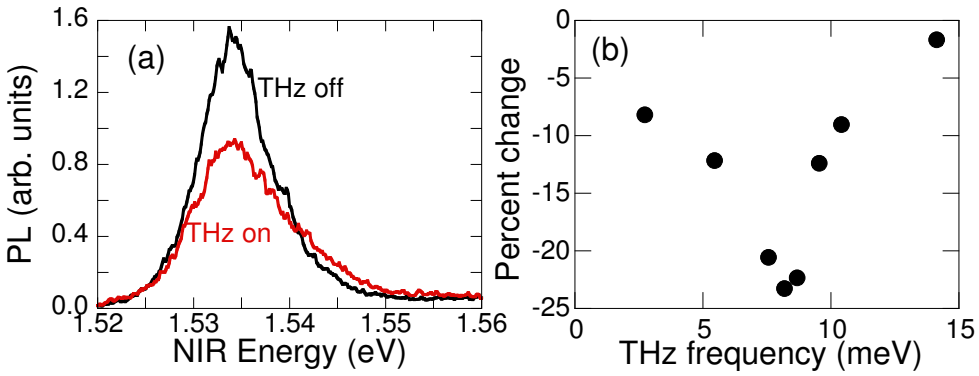

Figure 6.10: (a) Low-temperature PL of the doped sample with (red line) and without (black line) the THz field. The THz intensity was ∼40 kW/cm^2 at $\hbar\omega_{THz} = 8.2$ meV. (b) Percent change in the integrated PL of the doped sample at $E_{bias} = 5.8$ kV/cm with the THz field on at an intensity of ∼40 kW/cm^2. The PL was generated with the excitation laser at 763 nm, ∼200 W/cm^2. The dc electric field was 5.8 kV/cm.

also assume the electrons are non-interacting with singe-particle wavefunctions

$$\psi(\vec{x}) = \frac{1}{\sqrt{A}} e^{i\vec{k}\cdot\vec{x}} \varphi(z), \tag{6.4}$$

and energies

$$E_n(k) = E_n + \frac{\hbar^2 k^2}{2m^*}, \tag{6.5}$$

where A is the sample area and $\vec{k}$ is the in-plane wavevector. This type of model has been applied to doped GaAs QWs previously.[61] The expression for $\chi^{(2)}$ in Chapter 4, Eq. (4.7), can be modified for this system to include an integral over the in-plane momentum.

$$N \to \frac{1}{wA} \sum_k \to \frac{2\pi}{w} \int_0^\infty k dk N(k) \to \frac{1}{\pi w} \int_0^\infty k dk. \tag{6.6}$$

N is the number of states per unit volume, and $N(k)$ is the density of states in k-space per unit volume in real space. In two dimensions $N(k) = 2/(2\pi)^2$, accounting for spin-degeneracy. As in Chapter 4, many terms in the expression for $\chi^{(2)}$ can be eliminated, leaving

$$\chi^{(2)}_{xzx}(\omega_{NIR}+\omega_{THz};\omega_{THz},\omega_{NIR}) = \frac{\mu^x_{1n}\mu^z_{n\nu}\mu^x_{\nu 1}}{2\pi\hbar^2\epsilon_0 w}\sum_{n,\nu=2,3}\int_0^\infty kdk$$
$$\frac{\rho_{11}(k)-\rho_{\nu\nu}(k)}{(\omega_{n1}(k)-\omega_{NIR}-\omega_{THz}-i\gamma_{n1})(\omega_{\nu 1}(k)-\omega_{NIR}-i\gamma_{\nu 1})} -$$
$$\frac{\rho_{\nu\nu}(k)-\rho_{nn}(k)}{(\omega_{n1}(k)-\omega_{NIR}-\omega_{THz}-i\gamma_{n1})(\omega_{n\nu}(k)-\omega_{THz}-i\gamma_{n\nu})}. \tag{6.7}$$

The indices 1, 2, and 3 represent the hh1, e1, and e2 subbands respectively, $\omega_{mn}(k) = (E_m(k) - E_n(k))/\hbar$, and $\rho_{mm}(k)$ is the equilibrium occupation function of the mth subband at wavevector k. The interband matrix elements can be written as

$$\mu^x_{\nu 1} = \langle u_{k=0,c}|ex|u_{k=0,v}\rangle\langle\varphi_\nu|\varphi_1\rangle, \tag{6.8}$$

and the intersubband matrix elements can be written as

$$\mu^z_{n\nu} = e\langle\varphi_n|z_e|\varphi_\nu\rangle - e\delta_{n\nu}\langle\varphi_1|z_h|\varphi_1\rangle. \tag{6.9}$$

One could write the intersubband matrix elements in the usual form, $\langle\varphi_n|z_e|\varphi_\nu\rangle$, but then additional terms in Eq. (6.7) with $\langle\varphi_1|z_h|\varphi_1\rangle$ would appear, giving the same result.

The first term in Eq. (6.7) contains interband population differences and interband resonant denominators, and will be nonzero even without doping. This term is quite similar to that in Eq. (4.8) for undoped QWs and is considered an interband term. When $n \neq \nu$, the first term is in resonance when ω_{NIR} and $\omega_{sideband}$ match up with interband transitions, giving an indirect intersubband resonance. When $n = \nu$, the first term can only be in resonance for $\omega_{THz} < \gamma_{\nu 1}$, and it only involves one interband matrix element and the electron-hole dipole moment, $\mu^z_{\nu\nu}$. The $n = \nu$ first term is interpreted as resulting from the quasi-static modulation of the interband absorption. The second term requires an intersubband population difference and has one intersubband resonant denominator, so it will be considered an intersubband term. Near the intersubband transition, this second term is significantly larger than the others for a Fermi energy of several meV, ($E_F =$ $\sim$4.2 meV for the doped sample).

Equation (6.7) can be evaluated simply by approximating $\rho_{mm}(k)$ by zero-temperature equilibrium occupation functions: $\rho_{11}(k) = 1$, $\rho_{22}(k) = \theta(k_F - k)$, and $\rho_{33}(k) = 0$. The value of k_F is determined by the Fermi energy, $E_F = \hbar^2 k_F^2 / 2m^*$. Using this approximation, we obtain

$$\chi^{(2)}_{xzx}(\omega_{NIR} + \omega_{THz}; \omega_{THz}, \omega_{NIR}) = \frac{\mu^x_{1n}\mu^z_{n\nu}\mu^x_{\nu 1} m_r}{2\pi\hbar^3 \epsilon_0 w} \sum_{n,\nu=2,3}$$
$$\frac{1}{(\omega_{n\nu} - \omega_{THz} - i\gamma_{n1} + i\gamma_{\nu 1})} \ln\left[\frac{\omega_{n1} + \omega'_F \delta_{\nu 2} - \omega_{NIR} - \omega_{THz} - i\gamma_{n1}}{\omega_{\nu 1} + \omega'_F \delta_{\nu 2} - \omega_{NIR} - i\gamma_{\nu 1}}\right] -$$

$$\frac{n-\nu}{(\omega_{n\nu}-\omega_{THz}-i\gamma_{n\nu})}\ln\left[\frac{\omega_{n1}+\omega'_F-\omega_{NIR}-\omega_{THz}-i\gamma_{n1}}{\omega_{n1}-\omega_{NIR}-\omega_{THz}-i\gamma_{n1}}\right], \quad (6.10)$$

where m_r is the in-plane electron-hole reduced mass, $\omega'_F = \hbar k_F^2/2m_r$, and $\omega_{n\nu} = \omega_{n\nu}(k=0)$. A simple correction to Eq. (6.10) can be made to include the effect of collective intersubband modes. For the intersubband term, the bare intersubband frequency $\omega_{n\nu}$ can be replaced with the dressed frequency $\omega^*_{n\nu}$. This replacement should not be made in the interband term because the resonant denominator in Eq. (6.7) is interband. Using this correction, Eq. (6.10) was evaluated using dipole matrix elements calculated for an empty well and with interband and intersubband γ's of 2 meV and 1 meV, respectively, which gave the best fit. The 2D band gap was also adjusted to fit the lower edge of the measured PL at 1.532 eV. The intensity of the $n = +1$ sideband is proportional to $\left|\chi^{(2)}\right|^2$, which is plotted next to the experimental data in Fig. 6.9(a). The maxima are plotted as a function of ω_{THz} in the inset.

The model accurately predicts the strong resonance near the dressed intersubband frequency and the significant signal at low frequencies. It also predicts the redshift of the NIR resonance as ω_{THz} increased. However, the signal at $\omega_{THz} = 2.7$ meV was significantly stronger than predicted, and the signal above $\omega_{THz} = 10.4$ meV was much weaker than predicted. It may be that comparing the spectra with the same intensity outside the sample introduced this type of

error as the intensity coupled to the QW layers may depend on ω_{THz}. The extra resonances at low ω_{THz} were likely due to higher states, similar to those in Fig. 6.7(a), which are not considered in the model. These become important when ω_{THz} is off resonance, causing the intersubband term in Eq. (6.7) to be small. Finally, the widths and positions of the NIR resonances near $\omega_{THz} = 8.3$ meV were quite different from the model and cannot be improved by adjusting the γ's. A more sophisticated model, including many-body effects, may be necessary to fully explain these results.

Figure 6.11 displays the maximum of $\left|\chi^{(2)}(\omega_{NIR})\right|^2$ as a function of ω_{THz} and shows the contributions of the interband and intersubband terms, as well as the total. Clearly, the intersubband terms dominate, but the interband term is significant for low ω_{THz}. Interestingly, the interband and intersubband terms seem to cancel one another above the intersubband resonance, giving a sharp decrease. The peak value of $\left|\chi^{(2)}\right|$ is an order of magnitude lower than that of the undoped square well modelled in Chapter 4 at the excitonic intersubband resonance. However, the conversion efficiency of the doped sample is higher than that of the undoped square QW. Part of this discrepancy is due to the larger number of wells in the doped sample, and part may be due to inaccuracies in the models and the parameters used.

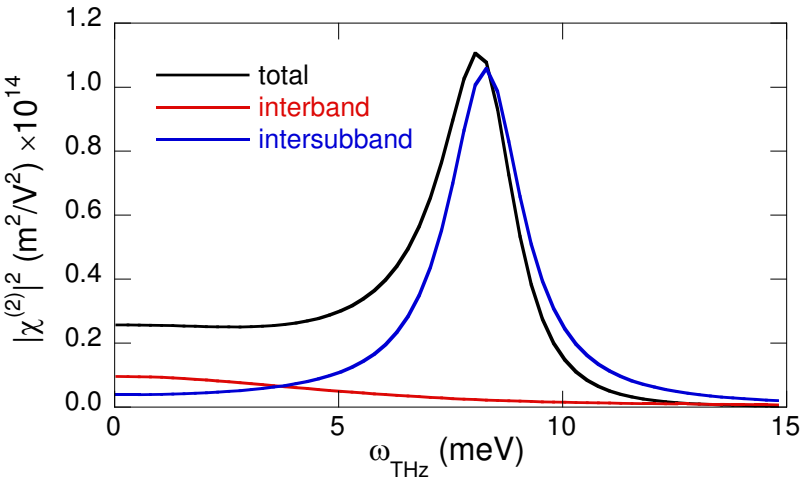

Figure 6.11: Calculated maximum of $|\chi^{(2)}(\omega_{NIR})|^2$ at 5.8 kV/cm using Eq. (6.10) as a function of $\hbar\omega_{THz}$. The red and blue curves were calculated just including the interband or intersubband term, respectively, while the black curve plots is the total.

6.5 Conclusion

THz-optical mixing has been measured for the first time in doped QWs, showing strikingly different resonant behavior than in undoped QWs. The most important distinction is that sidebands in doped QWs are primarily sensitive to the collective excitations of the electron gas, as demonstrated by the large resonance at the dressed intersubband frequency. This fact allows the use of THz-optical mixing to probe intersubband dynamics. Using NIR light as opposed to FIR light has the advantage of being able to probe very small areas, to use mature NIR optics, detectors, spectrometers, and to target specific QWs based on their interband transitions. These benefits are similar to those of Raman scattering,[71] but

sideband generation is uniquely suited to probe the *coherent* response of electrons to THz driving. Exciting effects have been predicted for doped QWs in strong THz fields,[3] which will be discussed in the next chapter. THz-optical mixing in doped QWs also shows some promise for wavelength conversion as it saturates at relatively high NIR intensities. The $\chi^{(2)}$ model provides a good qualitative understanding of THz-optical mixing and reproduces many of the experimental trends.

Chapter 7

Probing nonlinear dynamics in doped QWs

A significant motivation for measuring THz-optical mixing in doped QWs has been to use sideband generation as a probe of the dynamics of strongly driven electrons in QWs. Doped QWs have an effective nonlinearity due to the Coulomb interaction that is predicted to give rise to exciting, novel effects such as period-doubling bifurcations and optical bistability when driven with a strong THz field.[3, 72, 73] From sideband experiments in doped QWs, we know that the sidebands are generated by the collective dynamics of electrons, making sidebands a potential probe of these exciting nonlinear effects.

This chapter will discuss nonlinearity in doped QWs and some of the effects

predicted, and will then describe experiments performed in the doped double QW sample, SC9, to measure period-doubling bifurcations. Experiments in a triple QW structure, specially designed for nonlinear effects, will also be discussed. So far, no evidence of period-doubling bifurcations or other nonlinear effects has been observed. But this chapter will provide an introduction to how such effects may be observed in the future.

7.1 Nonlinear dynamics in QWs

The source of nonlinearity in doped QWs is the Coulomb interaction. This can be seen by examining Eq. (6.1) in Section 6.1.2, which includes the Coulomb interaction and exchange-correlation in the Schrödinger equation. In this mean-field approximation, the Hamiltonian is a function of the charge density, which is related to $|\varphi(z)|^2$. The eigenstates can still be found with this nonlinearity by iteratively adding charge to the well, computing the Hartree and exchange-correlation potentials, and finding the modified wavefunctions. In the presence of a driving field at frequency ω, the time-varying form of Eq. (6.1) can be written as

$$\left[-\frac{\hbar^2}{2m^*}\frac{\partial^2}{\partial z^2} + V(z) + V_H(n_0(z)) + \delta V(z,t) + eEz\sin(\omega t)\right]\xi(z,t) = i\frac{\partial}{\partial t}\xi(z,t), \tag{7.1}$$

and Poisson's equation becomes

$$\frac{\partial^2}{\partial z^2}\left[V_H(n_0(z)) + \delta V(z,t) + eEz\sin(\omega t)\right] = -\frac{e^2}{\epsilon}n(z,t). \tag{7.2}$$

In Eqns (7.1) and (7.2), the exchange-correlation potential has been ignored, E is the driving field amplitude, and $\delta V(z,t)$ is a dynamic screening term. The dynamic screening results in the depolarization shift, in which radiation is absorbed at a collective excitation frequency instead of the single particle frequency. The depolarization shift depends on the subband populations, and is highest when most electrons are in the lower subband. Experiments have demonstrated that the depolarization shift decreases with intensity as the upper subband is populated.[69]

Intensity-dependent absorption can lead to optical bistability, in which absorption at a given frequency and intensity depends on the system's past. Approaching a given intensity from high or low intensity gives two different values for the absorption. Optical bistability in the THz range has been predicted in doped QWs for two or three-subband systems.[73] More exotic effects such as period-doubling bifurcations to chaos and Hopf-bifurcations have been predicted as well.[3, 72, 73] The observation of chaos in a manifestly quantum system would be quite exciting.

7.1.1 Period-doubling bifurcations

Most of the effort on observing nonlinear dynamical effects was focused on period-doubling bifurcations since they should be simpler to observe than Hopf bifurcations. A period-doubling bifurcation occurs in a driven QW system when the electron polarization starts to oscillate at half of the drive frequency. This is illustrated in Fig. 7.1, which plots the response of a driven system before and after a period-doubling bifurcation. Before the bifurcation, the system responds at multiples of the drive frequency, so that if one sampled the response once every drive cycle, the same value would be obtained each time (after an initial transient). After the bifurcation, the system also responds at half of the drive frequency, so that two different values are obtained when sampling every drive cycle. When the different values sampled are plotted as a function of THz field for a driven QW system, the result can be Fig. 7.2,[3] which shows period-doubling bifurcations into chaos. For small amplitudes, only a single point is sampled, indicating a periodic solution. For somewhat larger amplitudes, there are hysteresis loops which indicate optical bistability. For amplitudes just above 1.6 (see inset graph) the number of points sampled bifurcates several times until there is a mass of points at $\sim$1.67, indicating chaos. A much more in-depth treatment of period-doubling bifurcations and nonlinear dynamics in general can be found in Ref. [74].

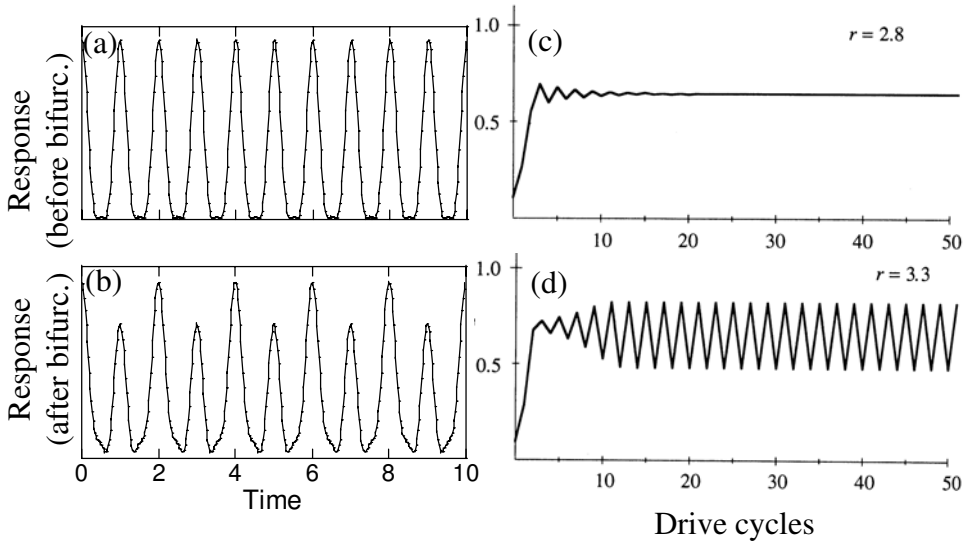

Figure 7.1: Response of a driven system before (a), (c) and after (b), (d) a period-doubling bifurcation. The response of the system as a function of time is plotted in (a) and (b), and the response sampled once every drive cycle is plotted in (c) and (d). The plots in (c) and (d) are taken from Ref. [74].

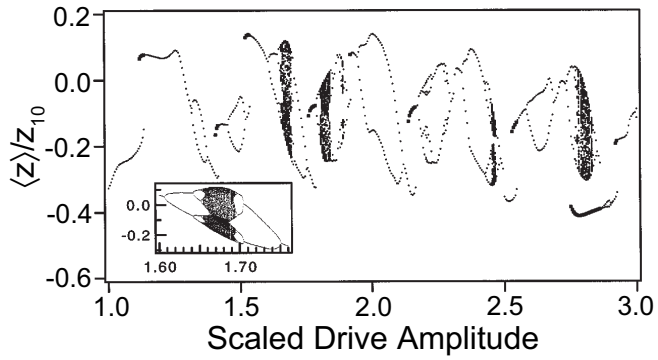

Figure 7.2: Bifurcation diagram taken from Ref. [3], sampling the expectation value of z vs. the drive amplitude. z is proportional to the intersubband polarization. The inset graph is an expanded view of the leftmost bifurcation to chaos.

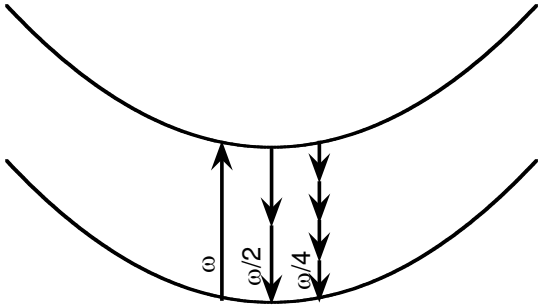

Figure 7.3: Comparison of period-doubling bifurcations to downconversion in a two subband system.

One can imagine a period-doubling bifurcation in this system as being similar to parametric down-conversion, as displayed schematically in Fig. 7.3. Both processes result in converting a higher frequency to a lower frequency, and both have resonances. Period-doubling bifurcations tend to occur when the drive frequency is resonant with the bare intersubband frequency ω_{10} or with $2\omega_{10}$.[73] A major difference between period-doubling bifurcations and down-conversion is that bifurcations only occur at a critical field and continue to bifurcate into chaos.

There are a number of conditions that must be met in order for the bifurcations to occur, which have been discussed in Ref. [3, 72, 73]. First, there must be a significant depolarization shift as it is the source of the nonlinearity. Also, the driving field must be strong ($\mu_{10}E \sim \hbar\omega_{10}$), the damping must not be too large, and the well must be asymmetric. The charge density must be within a certain range as well. In Ref. [3] Galdrikian *et. al.* simulated a 310 Å wide well with an

off-center, 50 Å wide tunnel barrier. The tunnel barrier was 65 meV high, giving two subbands spaced by 6.25 meV. The charge density used was 1.5×10^{11} cm^{-2}, giving a depolarization shift of $\alpha = 1.3$. The dressed frequency ω_{10}^{*} is related to the bare frequency ω_{10} by $\omega_{10}^{*} = \omega_{10}\sqrt{1+\alpha}$, when only the lower subband is populated. Period-doubling bifurcations occurred in this system when driven at $\omega_{drive} = \omega_{10}/3$ (in further publications bifurcations occurred with other drive frequencies as well) with drive field amplitudes of ∼15 kV/cm. In comparison to the power emitted by the QW at ω_{drive}, the power at $\omega_{drive}/2$ was an order of magnitude lower.

In Ref. [73] Batista *et. al.* made further progress on the two subband system and also simulated a 310 Å wide, asymmetric, triple QW structure. In this three-subband system, the sheet density was 3.0×10^{11} cm^{-2}, and the bare intersubband frequency between the lowest subband and the third subband was $\omega_{20} \sim 20$ meV. By driving this system at ω_{20}, period-doubling bifurcations occurred for significantly lower drive amplitudes (∼5 kV/cm) than in the two subband system. One interpretation is that this lowering occurred partly because the resulting oscillation at half the drive-frequency was near-resonance with ω_{10}. Experimental attempts were made to observe period-doubling bifurcations in both two and three subband systems.

7.2 Searching for period-doubling in SC9

Considering the success of SC9 for studying sideband generation in doped QWs, this sample was used to attempt to observe period-doubling bifurcations using sidebands. Before discussing the details of these attempts, we must first discuss how well this sample met the conditions for period-doubling bifurcations. The sample SC9 is asymmetric and has a significant charge density, $\sim 1.2 \times 10^{11}$ cm^{-2}, that is within the range described in Ref. [73] (0.5 to 6.0 $\times 10^{11}$ cm^{-2} for a 310 Å QW). This leads to a significant depolarization shift, which is plotted in Fig. 7.4(b) as a function of dc electric field. The depolarization shift peaks at -6 kV/cm, but the asymmetry ζ is zero at this field. The asymmetry parameter is defined as $|\mu_{11} - \mu_{00}|/\mu_{10}$. The best dc electric field appears to be near -11 or 0 kV/cm, where both α and ζ are a little bigger than 1. The intersubband matrix element is $\sim$58 Å at these points, comparable to that in Ref. [3]. Based on these characteristics, SC9 is well-suited for observing period-doubling bifurcations.

While no theoretical work has been done to establish that bifurcations can be measured using sideband measurements, it is apparent from Chapter 6 that sidebands are sensitive to the intersubband polarization. If this polarization begins to oscillate at half the THz drive frequency, a sideband at $\omega_{NIR} + \omega_{THz}/2$ should appear. Figure 7.5 illustrates the expected $n = +1/2$ sideband.

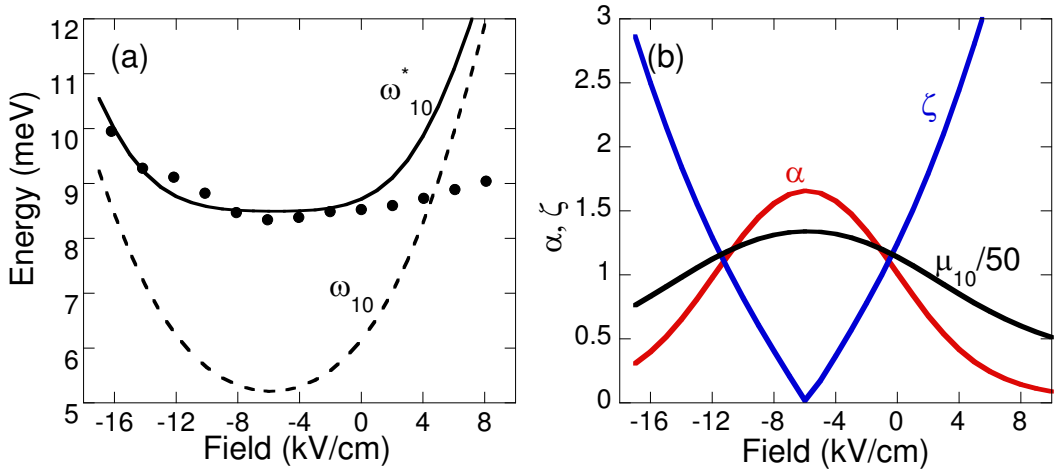

Figure 7.4: (a) Intersubband absorption frequency vs. dc electric field. The circles represent the frequencies determined experimentally. The solid line and the dashed line represent the calculated dressed and bare intersubband frequencies, respectively. (b) Calculated dipole matrix element $\mu_{10}/50$ Å (black), depolarization shift α (red), and asymmetry ζ (blue) as a function of dc electric field. The calculations were performed using Brian Galdrikian's program.

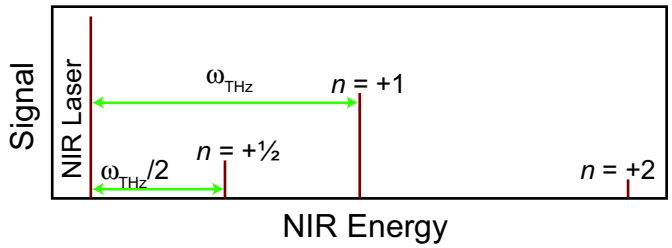

Figure 7.5: Illustration of the expected $n = +1/2$ sideband.

There are many parameters that can be varied looking for period-doubling bifurcations in the sidebands: the NIR laser frequency, THz frequency, THz power, dc electric field, and the sideband detection frequency. Fortunately, the range over which some of these parameters should be varied to detect the bifurcations can be limited. First of all, for period-doubling bifurcations, the sideband detection frequency can be set at $\omega_{NIR}+\omega_{THz}/2$. (For Hopf bifurcations, the exact frequency of the subharmonic is unknown.) Second, the proper NIR laser frequency should be determined by the $n = +1$ sideband resonance spectra. The idea is that the $n = +1/2$ resonance for drive frequency ω_{THz} should be at a similar position as the $n = +1$ resonance for drive frequency $\omega_{THz}/2$. While this assumption may not be fully correct, the NIR resonances are sufficiently broad for $n = +1$ sidebands that measurements at 1 or 2 NIR frequencies should be enough. Finally, period-doubling bifurcations are most likely to occur when driving at twice the bare intersubband frequency, which should be between 10 and 14 meV, based on the results of the simulations shown in Fig. 7.4(a).

Period-doubling bifurcations were searched for by performing $n = +1/2$ sideband voltage scans (-16.7 to +8 kV/cm) at $\hbar\omega_{THz}$ = 10.4, 11.3, 11.7, 12.8, and 14.1 meV. These experiments were performed using the same sample as in Chapter 6, with ITO-coated glass pressed onto the sample. The frequency range over which bifurcations should occur can be relatively narrow ($<$ 10 % of ω_{10}), but

the value of ω_{10} tunes with the dc electric field, so the entire range from 10 to 14 meV should have been well-covered. For each THz frequency, one or two voltage scans were performed at different NIR frequencies, chosen to minimize chances of missing the resonance. Voltage scans were measured using the highest available power (from ∼1800 W at $\hbar\omega_{THz}$ = 10.4 meV to ∼500 W at 11.3 meV) and at a power 50-60% lower when the max power was relatively high (>∼1 kW). This reduction in power was performed just in case the THz intensity was too high. For the highest power of ∼1800 W, the THz field inside the sample should have been ∼15 kV/cm, including reflection losses. This field should be high enough to observe period-doubling bifurcations, according to theory, but no $n = +1/2$ sidebands were observed. $n = +1/2$ sidebands an order of magnitude smaller than the $n = +1$ sideband could have been easily detected for all of the THz frequencies used, so it seems unlikely that the signal was missed.

7.3 Searching for period-doubling in a triple well

7.3.1 Sample characteristics

The triple QW design was taken from Ref. [73] and is shown in Fig. 7.6(a). (See Appendix C for the complete structure.) The triple QW consists of three GaAs wells, 92, 88, and 78 Å wide, separated by two $Al_{0.2}Ga_{0.8}As$ tunnel barriers 26 Å

wide. This asymmetric triple QW gives rise to three subbands spaced in the THz range. The tunnel barriers were made higher in energy than in Ref. [73] in order to decrease the intersubband spacing to be within the range of the FEL. The doping was designed to give 3×10^{11} cm^{-2} per well, as in Ref. [73]. By using Galdrikian's QW simulation program, the bare intersubband frequencies were $\omega_{10} = 4.7$ meV and $\omega_{20} = 13.9$ meV. With the high charge density present, the second subband was partially occupied ($\sim$72% 1st subband, $\sim$28% 2nd subband). This meant that intersubband transitions were allowed from both of the lower 2 subbands. The depolarization shifted frequencies were calculated to be $\omega^*_{10} = 8.1$ meV, $\omega^*_{21} = 9.13$ meV, and $\omega^*_{20} = 13.9$ meV. The dipole matrix element μ_{20} was almost zero with no bias, so the $0 \rightarrow 2$ transition was not allowed.

The sample, called TripleQW2, contained 10 of these triple QWs in the same structure as in SC9 (see Fig. 6.1), including the doped gate QWs and the DBR. The spacing between well centers was kept the same to again increase interaction with the NIR radiation. Figure 7.6(b) displays the PL, PLE, and reflectivity of TripleQW2. The PLE was measured by detecting PL on the lower energy side of the PL peak at $\sim$1.536 eV while scanning the NIR laser. This measurement probed the absorption, and in this case was cleaner than the reflectivity, which was influenced by the DBR and the periodic placement of QWs. As in SC9, there was a shift between the PL and the absorption due to Pauli blocking of the filled

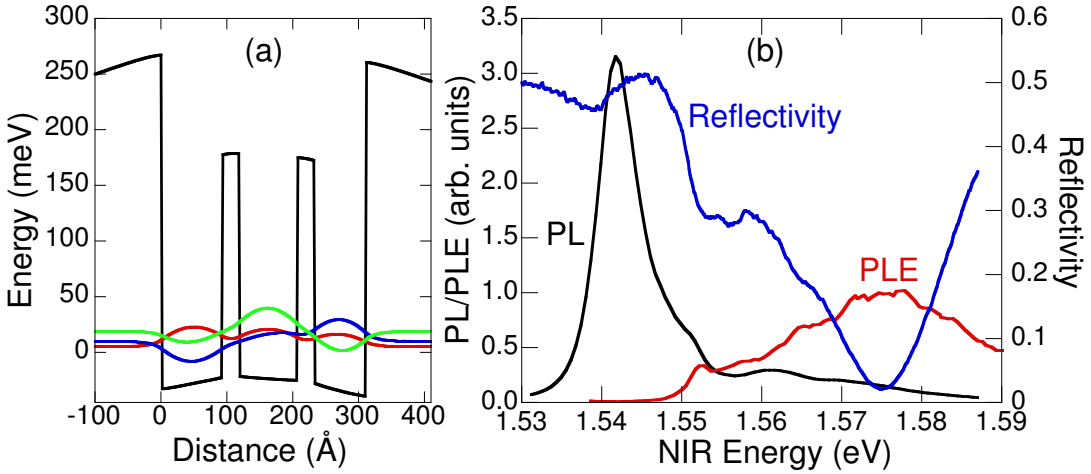

Figure 7.6: (a) Conduction band profile of TripleQW2, including the self-consistent potential due to the Coulomb interaction. The envelope functions of the three lowest subbands are shown, offset according to their energies. (b) PL (black), PLE (red) and reflectivity (blue) of TripleQW2 at ∼11 K. The PL was taken with the NIR laser at 755 nm, ∼0.8 mW. The PLE was taken by measuring the PL at ∼1.536 eV, and the reflectivity was taken using "white" light from a lamp.

states, and the PL and absorption features were quite broad. Due to the large number of electron and hole states expected in this QW structure and the large linewidths, assignments to particular interband transitions in this spectrum was impractical.

Intersubband absorption measurements were performed on this sample using FTIR transmission spectroscopy. However, there were significant problems with the reference spectrum used for normalization. The application of a strong dc electric field across the sample did not give a useful reference. Instead, the first few wells were depleted as a reference. This gave some strange results for the intersubband absorption, but there was clearly significant absorption at ∼10 meV and ∼13.6 meV.

7.3.2 Sideband measurements

Figure 7.7 displays the $n = +1$ sideband resonance spectra at a series of THz frequencies. These spectra were taken with $E_{bias} = 0$ kV/cm at ∼11 K. There was a strong signal at the lowest THz frequency ($\hbar\omega_{THz} = 2.7$ meV) as in SC9, and there was a strong signal from $\hbar\omega_{THz} = 6.3$ to 10.4 meV. The complete resonant structure cannot be obtained from these few spectra, but the sideband signal does appear to be strong near the expected intersubband resonances, ω_{10}^* and ω_{21}^*, at 8.1 meV and 9.1 meV, respectively.

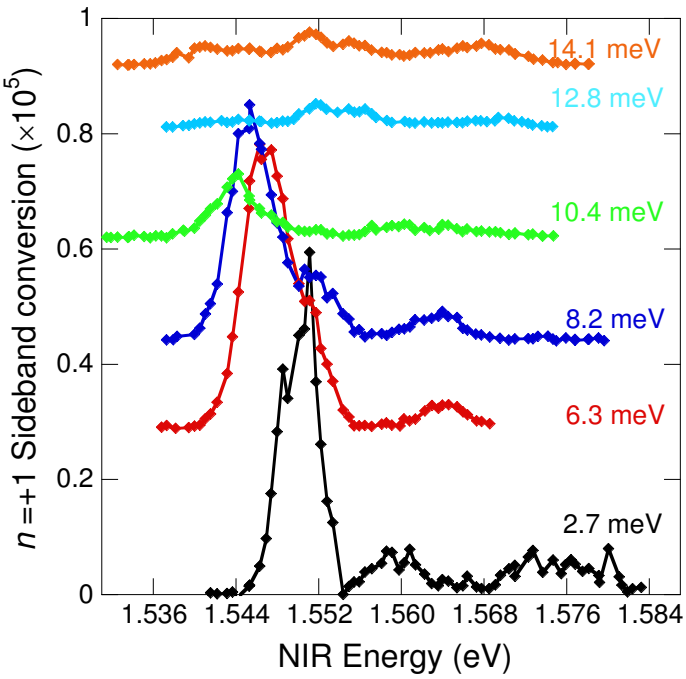

Figure 7.7: The $n = +1$ sideband resonance spectra of the triple QW sample at $E_{bias} = 0$ kV/cm for a series of THz frequencies, all with intensities near 40 kW/cm^2. The temperature was ∼11 K. The spectra are vertically offset and labelled according to ω_{THz}.

Period-doubling bifurcations were searched for by performing $n = +1/2$ sideband voltage scans (-6.3 to +6.3 kV/cm) at $\hbar\omega_{THz} = 10.4$, 12.8, and 14.1 meV. These frequencies were near ω_{20}, where the period-doubling bifurcations were expected to occur. The THz intensities were comparable to those used in period-doubling experiments on SC9. No $n = +1/2$ sidebands were observed, but it could certainly be argued that the parameter-space was not well covered.

7.4 Conclusion

There are a number of exciting nonlinear effects predicted for doped QWs driven by a strong THz field, including optical bistability, period-doubling bifurcations, and Hopf bifurcations. THz-optical mixing provides an good method of observing these effects due to the maturity of NIR optics, detectors, and spectrometers, and the ability to probe very small areas. The experiments described in this chapter have looked specifically for period-doubling bifurcations in a double and triple QW, both of which should have the necessary characteristics for observing such effects. No bifurcations were observed, although further experiments should be done to explore more of the parameter-space. One possible reason that the bifurcations were not observed is that THz field at the QW positions might not have been as high as expected from the intensity outside the sample. A good

improvement would be to grow a doped QW sample with InGaAs QWs in order to use the geometry shown in Fig. 2.1(a), which seemed to provide a stronger THz field at the QW positions.

Chapter 8

Conclusions

8.1 Summary

This dissertation has explored the effects of a growth-direction THz field on the interband optical properties of (In)GaAs QWs. The effect of a strong THz field on the linear absorption of $In_{0.06}Ga_{0.94}As$ QWs was particularly dramatic. When the THz field was resonant between two heavy-hole exciton states, a splitting was observed, indicating strong coupling of the states by the THz field. This effect is related to Autler-Townes splitting and electromagnetically-induced-transparency. For somewhat lower THz fields, THz-optical mixing was studied in a similar GaAs QW whose symmetry could be changed by applying a dc electric field. Sidebands generation was fully characterized and modelled in this relatively simple square

QW system, giving a much greater physical understanding of THz-optical mixing.

These results have implications for optical communications in terms of high-frequency QW modulation and wavelength conversion. Experiments on sideband generation in a multiple asymmetric coupled QW sample continued toward these applications by studying the suitability of THz-optical mixing for all-optical wavelength conversion. These experiments demonstrated improved sideband conversion efficiency and room temperature operation.

THz-optical mixing was measured for the first time in n-doped QWs and was shown to be quite different from that in the undoped QWs. The resonant behavior of the sidebands demonstrates that mixing in doped QWs is primarily sensitive to electronic intersubband transitions instead of excitonic intersubband transitions. This fact allows the use of THz-optical mixing to probe intersubband dynamics. This method was used to attempt to observe exciting nonlinear effects in strongly driven doped QWs.

8.2 Future Directions

The measurement of THz-dressed states in undoped QWs opens up many possibilities for further experiments. Experiments are already underway to measure the effect of breaking inversion symmetry on these THz-dressed states. Also,

strong THz field effects beyond the Rabi-splitting regime may be studied, in which the Rabi energy is comparable to the THz photon energy. In this strong-field regime, replicas of the exciton states are expected to appear, shifted by multiples of the THz frequency. Another potential experiment is to study dynamic localization in a superlattice driven by a strong THz field.[75]

The improvements in the InGaAs sample also suggest that the THz field at the QW positions can be substantially improved using this new THz-coupling geometry. This may yield a dramatic increase in the sideband conversion efficiency that could make this technique more useful technologically and scientifically.

Finally, the observation of THz-optical mixing in doped QWs along with improvements in THz-coupling could make the observation of nonlinear effects such as period-doubling effects possible using THz-optical mixing.

Bibliography

[1] J. Shah. *Ultrafast spectroscopy of semiconductors and semiconductor nanostructures.* Springer, New York, 1996.

[2] S. H. Autler and C. H. Townes. Stark effect in rapidly varying fields. *Phys. Rev.*, 100(2):703–22, Oct 1955.

[3] B. Galdrikian and B. Birnir. Period doubling and strange attractors in quantum wells. *Phys. Rev. Lett.*, 76:3308, 1996.

[4] E. H. Li. Material parameters of InGaAsP and InAlGaAs systems for use in quantum well structures at low and room temperatures. *Physica E*, 5:215–273, 2000.

[5] J. H. Davies. *The Physics of Low-Dimensional Semiconductors, an Introduction.* Cambridge University Press, 1998.

[6] R. Dingle, W. Weigmann, and C. H. Henry. Quantum states of confined carriers in very thin $Al_xGa_{1-x}As$-GaAs-$Al_xGa_{1-x}As$ heterostructures. *Phys. Rev. Lett.*, 33(14):827–830, Sept 1974.

[7] M. Helm. The basic physics of intersubband transitions. *Semiconductors and Semimetals*, 62:1–99, Sept 2000.

[8] Q. Wu and X. C. Zhang. Design and characterization of traveling-wave electrooptic terahertz sensors. *IEEE J. Sel. Topics Quantum Electron.*, 2(3):693–700, Sept 1996.

[9] S. M. Quinlan, A. Nikroo, M. S. Sherwin, M. Sundaram, and A. C. Gossard. Photoluminescence from $Al_xGa_{1-x}As$/GaAs quantum wells quenched by intense far-infrared radiation. *Phys. Rev. B*, 45(16):9428–31, Apr 1992.

[10] J. Černe, A. G. Markelz, M. S. Sherwin, S. J. Allen, M. Sundaram, A. C. Gossard, P. C. van Son, and D. Bimberg. Quenching of excitonic quantum-well photoluminescence by intense far-infrared radiation: Free-carrier heating. *Phys. Rev. B*, 51(8):5253–62, Feb 1995.

[11] N. G. Asmar, J. Černe, A. G. Markelz, E. G. Gwinn, M. S. Sherwin, K. L. Campman, and A. C. Gossard. Temperature of quasi-two-dimensional electron gases under steady-state terahertz drive. *Appl. Phys. Lett.*, 68(6):829–31, Feb 1996.

[12] J. Černe, J. Kono, M. S. Sherwin, M. Sundaram, A. C. Gossard, and G. E. W. Bauer. Terahertz dynamics of excitons in GaAs/AlGaAs quantum wells. *Phys. Rev. Lett.*, 77(6):1131–34, Aug 1996.

[13] J. Černe, J. Kono, T. Inoshita, M. Sherwin, M. Sundaram, and A. C. Gossard. Near-infrared sideband generation induced by intense far-infrared radiation in gaas quantum wells. *Appl. Phys. Lett.*, 70(26):3543–5, June 1997.

[14] J. Kono, M. Y. Su, T. Inoshita, T. Noda, M. S. Sherwin, S. J. Allen, Jr., and H. Sakaki. Resonant terahertz optical sideband generation from confined magnetoexcitons. *Phys. Rev. Lett.*, 79(9):1758–61, Sept 1997.

[15] K. Johnsen and A.-P. Jauho. Quasienergy spectroscopy of excitons. *Phys. Rev. Lett.*, 83(6):1207–10, Aug 1999.

[16] S. Hughes and D. S. Citrin. Dynamic FranzKeldysh effect: excitonic versus free-carrier excitation schemes. *Opt. Lett.*, 24(15):1068–70, Aug 1999.

[17] D. S. Citrin and S. Hughes. Circularly polarized dynamic Franz-Keldysh effect. *Phys. Rev. B*, 60(19):13272–5, Nov 1999.

[18] S. Hughes and D. S. Citrin. Dynamic FranzKeldysh effect: perturbative to nonperturbative regime. *Opt. Lett.*, 25(7):493–5, Apr 2000.

[19] K. B. Nordstrom, K. Johnsen, S.J. Allen, A.-P. Jauho, B. Birnir, J. Kono, T. Noda, H. Akiyama, and H. Sakaki. Excitonic dynamical Franz-Keldysh effect. *Phys. Rev. Lett.*, 81(2):457–60, Jul 1998.

[20] A. H. Chin, J. M. Bakker, and J. Kono. Ultrafast electroabsorption at the transition between classical and quantum response. *Phys. Rev. Lett.*, 85(15):3293–6, Oct 2000.

[21] A. H. Chin, J. Kono, and G. S. Solomon. Absence of exciton quenching in the presence of strong fields at high frequencies. *Phys. Rev. B*, 65:121307(R), Mar 2002.

[22] A. P. Jauho and K. Johnsen. Dynamical Franz-Keldysh effect. *Phys. Rev. Lett.*, 76(24):4576–9, Jun 1996.

[23] C. J. Dent, B. N. Murdin, and I. Galbraith. Phase and intensity dependence of the dynamical Franz-Keldysh effect. *Phys. Rev. B*, 67:165312, Apr 2003.

[24] H. Weman, G. M. Treacy, H. P. Hjalmarson, K. K. Law, J. P. Bergman, J. L. Merz, and A. C. Gossard. Impact ionization of free and bound excitons in AlGaAs/GaAs quantum wells. *Semicond. Sci. Technol.*, 7:B517–9, 1992.

[25] E. E. Mendez, G. Bastard, L. L. Chang, L. Esaki, H. Morkoc, and R. Fischer. Effect of an electric field on the luminescence of GaAs quantum wells. *Phys. Rev. B*, 26(12):7101–4, Dec 1982.

[26] D. A. B. Miller, D. S. Chemla, T. C. Damen, A. C. Gossard, W. Wiegmann, T. H. Wood, and C. A. Burrus. Band-edge electroabsorption in quantum well structures: The quantum-confined stark effect. *Phys. Rev. Lett.*, 53(22):2173–6, Nov 1984.

[27] C. Phillips, M. Y. Su, M. S. Sherwin, J. Ko, and L. Coldren. Generation of first-order terahertz optical sidebands in asymmetric coupled quantum wells. *Appl. Phys. Lett.*, 75(18):2728–30, Nov 1999.

[28] M. A. Zudov, J. Kono, A. P. Mitchell, and A. H. Chin. Time-resolved, nonperturbative, and off-resonance generation of optical terahertz sidebands from bulk GaAs. *Phys. Rev. B*, 64:121204(R), Sep 2001.

[29] M. Y. Su, S. G. Carter, M. S. Sherwin, A. Huntington, and L. A. Coldren. Voltage-controlled wavelength conversion by terahertz electro-optic modulation in double quantum wells. *Appl. Phys. Lett.*, 81(9):1564–6, Aug 2002.

[30] M. Y. Su. *Terahertz Electro-Optics of Excitonic Intersubband Excitations in Double Quantum Wells*. PhD thesis, University of California, Santa Barbara, 2002.

[31] D. S. Citrin. Doubly resonant terahertz sideband generation in quantum wells: Optical signatures of terahertz-dressed subbands. *Phys. Rev. B*, 60(19):13695–701, Nov 1999.

[32] A. V. Maslov and D. S. Citrin. Optical absorption and sideband generation in quantum wells driven by a terahertz electric field. *Phys. Rev. B*, 62(24):16686–91, Dec 2000.

[33] A. Shimizu, M. Kuwata-Gonokami, and H. Sakaki. Enhanced second-order optical nonlinearity using inter- and intra-band transitions in low-dimensional semiconductors. *Appl. Phys. Lett.*, 61(4):399–401, Jul 1992.

[34] A. V. Maslov and D. S. Citrin. Enhanced optical/THz frequency mixing in a biased quantum well. *Solid State Comm.*, 120:123–7, 2001.

[35] M. Y. Su, S. G. Carter, M. S. Sherwin, A. Huntington, and L. A. Coldren. Strong-field terahertz optical mixing in excitons. *Phys. Rev. B*, 67:125307, 2003.

[36] A. V. Maslov and D. S. Citrin. Optical absorption of thz-field-driven and dc-biased quantum wells. *Phys. Rev. B*, 64:155309, 2001.

[37] A. V. Maslov and D. S. Citrin. Numerical calculation of the terahertz field-induced changes in the optical absorption in quantum wells. *IEEE J. Sel. Top. Quantum Electron.*, 8(3):457–63, 2002.

[38] A. Liu and C. Z. Ning. Exciton absorption in semiconductor quantum wells driven by a strong intersubband pump field. *J. Opt. Soc. Am. B*, 17(3):433–9, 2000.

[39] G. Snider. 1D Poisson. `<http://www.nd.edu/~gsnider/>`.

[40] The low-temperature indices of refraction were estimated at 3.625 for GaAs, 3.372 for 30% AlGaAs , and 2.975 for AlAs.

[41] T. Bauer, J. S. Kolb, T. Löffler, E. Mohler, H. G. Roskos, and U. C. Pernisz. Indiumtinoxide-coated glass as dichroic mirror for far-infrared electromagnetic radiation. *J. Appl. Phys.*, 92:2210–12, 2002.

[42] J. B. Williams. *Dissipation of THz frequency intersubband plasmons in quantum wells*. PhD thesis, University of California, Santa Barbara, 2000.

[43] A. Mysyrowicz, D. Hulin, A. Antonetti, A. Migus, W. T. Masselink, and H. Morkoç. "Dressed Excitons" in a multiple-quantum-well structure: Evidence for an optical stark effect with femtosecond response time. *Phys. Rev. Lett.*, 56(25):2748–51, Jun 1986.

[44] D. Frölich, R. Wille, W. Schlapp, and G. Weimann. Optical quantum-confined stark effect in GaAs quantum wells. *Phys. Rev. Lett.*, 59(15):1748–1751, Oct 1987.

[45] R. Shimano and Makoto Kuwata-Gonokami. Observation of Autler-Townes splitting of biexcitons in CuCl. *Phys. Rev. Lett.*, 72(4):530–33, Jan 1994.

[46] G. B. Serapiglia, E. Paspalakis, C. Sirtori, K. L. Vodopyanov, and C. C. Phillips. Laser-induced quantum coherence in a semiconductor quantum well. *Phys. Rev. Lett.*, 84(5):1019–22, Jan 2000.

[47] M. Phillips, Hailin Wang, I. Rumyantsev, N. H. Kwong, R. Takayama, and R. Binder. Electromagnetically induced transparency in semiconductors via biexciton coherence. *Phys. Rev. Lett.*, 91(18):183602, Oct 2003.

[48] J. H. Shirley. Solution of the Schrödinger equation with a hamiltionian periodic in time. *Phys. Rev.*, 138(4B):B979–87, May 1965.

[49] R. W. Boyd. *Nonlinear Optics*, chapter 5, pages 214–225. Academic, San Diego, 1992.

[50] M. Naganuma, T. Ishibashi, and Y. Horikosh. The electric field induced photoluminescence properties of GaAs/Al_xGa_{1-x}As quantum-well structures grown by molecular-beam epitaxy. *J. Appl. Phys.*, 62(2):644, July 1987.

[51] R. W. Boyd. *Nonlinear Optics*, chapter 3, page 137. Academic, San Diego, 1992.

[52] C. Weisbuch and B. Vinter. *Quantum Semiconductor Structures*, chapter 3, page 64. Academic Press, San Diego, 1991.

[53] A. V. Kuznetsov, G. D. Sanders, and C. J. Stanton. Wave-packet dynamics in quantum wells. *Phys. Rev. B*, 52:12045, 1995.

[54] R. W. Boyd. *Nonlinear Optics*, chapter 1, pages 34,35. Academic, San Diego, 1992.

[55] D. Nesset, T. Kelly, and D. Marcenac. All-optical wavelength conversion using SOA nonlinearities. *IEEE Commun. Mag.*, 36:56, 1998.

[56] M. L. Mašanović, V. Lal, J. S. Barton, E. J. Skogen, D. J. Blumenthal, and L. A. Coldren. Monolithically integrated mach-zehnder interferometer wavelength converter and widely-tunable laser in InP. *IEEE Photonics Technol. Lett.*, 15:1117, 2003.

[57] A. Hsu and S. L. Chuang. Wavelength conversion by dual-pump four-wave mixing in an integrated laser modulator. *IEEE Photonics Technol. Lett.*, 15:1120, 2003.

[58] K. Torii and S. Yamashita. Efficiency improvement of optical fiber wavelength converter without spectral spread using synchronous phase/frequency modulations. *J. Lightwave Technol.*, 21:1039, 2003.

[59] M. Asobe, O. Tadanaga, H. Miyazawa, Y. Nishida, and H. Suzuki. Multiple quasi-phase-matched $LiNbO_3$ wavelength converter with a continuously phase-modulated domain structure. *Opt. Lett.*, 28:558, 2003.

[60] E. V. Loewenstein, D. R. Smith, and R. L. Morgan. Optical constants of far infrared materials. 2: Crystalline solids. *Appl. Opt.*, 12(2):398, Feb 1973.

[61] A. Neogi, Y. Takahashi, and H. Kawaguchi. Interband difference-frequency generation by means of resonant intersubband transitions in asymmetric quantum wells. *J. Opt. Soc. Am. B*, 14(3):570, Mar 1997.

[62] R. W. Boyd. *Nonlinear Optics*, chapter 10, page 404. Academic, San Diego, 1992.

[63] R. Kohler, A. Tredicucci, F. Beltram, H. E. Beere, E. H Linfield, A. G. Davies, D. A. Ritchie, R. C. Iotti, and F. Rossi. Terahertz semiconductor-heterostructure laser. *Nature (London)*, 417:156, May 2002.

[64] D. S. Citrin (private communication).

[65] C. Delalande, J. Orgonasi, J. A. Brum, G. Bastard, M. Voos, G. Weimann, and W. Schlapp. Optical studies of a GaAs quantum well based field-effect transistor. *Appl. Phys. Lett.*, 51(17):1346, Oct 1987.

[66] D. A. Kleinman and R. C. Miller. Band-gap renormalization in semiconductor quantum wells containing carriers. *Phys. Rev. B*, 32(4):2266, Aug 1985.

[67] A. Harwit and J. S. Harris. Observation of stark shifts in quantum well intersubband transitions. *Appl. Phys. Lett.*, 50(11):685, Mar 1987.

[68] Y. J. Mii, R. P. G. Karunasiri, K. L. Wang, M. Chen, and P. F. Yuh. Large stark shifts of the local to global state intersubband transitions in step quantum wells. *Appl. Phys. Lett.*, 56(20):1986, May 1990.

[69] K. Craig, B. Galdrikian, J. N. Heyman, A. G. Markelz, J. B. Williams, M. S. Sherwin, K. Campman, P. F. Hopkins, and A. C. Gossard. Undressing a collective intersubband excitation in a quantum well. *Phys. Rev. Lett.*, 76(13):2382–5, Mar 1996.

[70] R. Romestain and C. Weisbuch. Optical detection of cyclotron resonance in semiconductors. *Phys. Rev. Lett.*, 45:2067, 1980.

[71] G. Abstreiter, R. Merlin, and A. Pinczuk. Inelastic light scattering by electronic excitations in semiconductor heterostructures. *IEEE J. Quantum Electron.*, QE-22:1771, 1986.

[72] A. A. Batista, B. Birnir, and M. S. Sherwin. Subharmonic generation in a driven asymmetric quantum well. *Phys. Rev. B*, 61:15108, 2000.

[73] A. A. Batista, P. I. Tamborenea, B. Birnir, M. S. Sherwin, and D. S. Citrin. Nonlinear dynamics in far-infrared driven quantum-well intersubband transitions. *Phys. Rev. B*, 66:195325, 2002.

[74] S. H. Strogatz. *Nonlinear dynamics and chaos.* Perseus, Cambridge, Massachusetts, 1994.

[75] M. Holthaus. Collapse of minibands in far-infrared irradiated superlattices. *Phys. Rev. Lett.*, 69:351, 1992.

[76] J. S. Blakemore. Semiconducting and other major properties of gallium arsenide. *J. Appl. Phys.*, 53:R123–81, 1982.

Appendix A

Sample processing details

Since the devices used in this research were relatively large, the sample processing was relatively straightforward. The recipes presented in this appendix worked well for such devices, but may not be fully optimized for processing much smaller devices.

A.1 Standard process

The following recipes are presented in the order that they were performed in processing the standard gated THz-EO devices (see Section 2.2.1).

A.1.1 Cleaning

Regular cleaning consists of soaking in Acetone, Methanol, and DI for about 1 minute each in that order. Then blow-dry with N_2. If the cleaning is done in Aluminum dishes, the sample must be rinsed under the DI faucet afterward or some type of film may remain on the sample. This film seems to always be present on the surface of DI when in these Aluminum dishes. Glassware doesn't seem to have this problem. For a more thorough cleaning, the solvent cleaning can be done with ultrasound.

A.1.2 Single-layer photolithography

A single-layer photoresist (PR) can be used for etches or for very thin depositions.

	Step	Notes
1	Solvent clean	
2	Dehydration Bake ∼110 °C 1 m	Typically skip if sample dry
3	Apply AZ4110 with dropper	avoid PR over sample edge
4	Spin 5500 rpm 30 s	
5	Bake ∼95 °C 1 m	
6	Expose 7.5 mW for 25 s	no filter
7	Develop in AZ400K:DI (1:4) for 45 s	light agitation by hand
8	DI rinse ∼15 s, dry	
9	Bake ∼110 °C 1 m	hard bake

A.1.3 Wet etch

The wet etch used is $NH_4OH:H_2O_2:H_2O$ (10.5:1.8:150). This etch is supposed to give ∼100 Å/s, but I have found that the rate is somewhat variable, between 80 and 100 Å/s. Perhaps this is because the etch is sensitive to Al concentration. Obtaining the desired etch depth is accomplished by making several etches and measuring the depth each time with the Dektak.

	Step	Notes
1	Measure PR height	Use Dektak, keep track of position
2	Etch in $NH_4OH:H_2O_2:H_2O$	assume 100 Å/s
3	DI rinse ∼15 s, dry	
4	Measure etch depth (subtract PR height)	same position as step 1
5	Repeat steps 2-4 until correct depth	use etch rate calc. from first etch.
6	Solvent clean	
7	Measure etch depth	

A.1.4 Bi-layer photolithography

A bi-layer PR is used for deposition of Ni/Ge/Au/Ni/Au ohmic contacts, Aluminum gates, and for other relatively thick depositions.

	Step	Notes
1	Solvent clean	
2	Dehydration Bake ∼110 °C 1 m	Typically skip if sample dry
3	Apply OCG825 with dropper	avoid PR over sample edge
4	Spin 4000 rpm 1 m	
5	Bake ∼95 °C 1 m	
6	Flood Expose 7.5 mW for 10 s	no filter
7	Apply AZ4110 with dropper	avoid PR over sample edge
8	Spin 5500 rpm 30 s	
9	Bake ∼95 °C 1 m	
10	Expose 7.5 mW for 25 s	no filter
11	Develop in AZ400K:DI (1:4) for 45 s	light agitation by hand
12	DI rinse ∼15 s, dry	
13	Bake ∼110 °C 1 m	hard bake

A.1.5 Ohmic contact (Ni/Ge/Au/Ni/Au) deposition

Ni/Ge/Au/Ni/Au (50/177/350/100/2000 Å) is deposited using E-beam#3.

A.1.6 Liftoff

After metal deposition, the sample is soaked in Acetone until liftoff. This may take many hours unassisted. Liftoff occurs more quickly if the sample is sprayed with Acetone (air bubbles in the spray makes this even faster). Ultrasound may be used briefly as well.

A.1.7 Rapid Thermal Anneal

The sample is annealed in the rapid thermal annealer at 430 °C for 30 s in the presence of forming gas. This causes the Ge/Au to melt and diffuse into the sample, forming ohmic contact to doped wells.

A.1.8 Low-temperature IV check

The IV of the devices can be checked using the cleanroom probe station and curve tracer. It is often a good idea to check these at 77 K to determine which devices will work at low-temperatures. The sample is placed on an Aluminum ring (or disk) in a foam cup with the top cut off. The probes are raised with respect to the sample stage using the lever on the left (shove cleanroom wipes in the slot), due to the increased height of the sample. Liquid N_2 can then be slowly poured in by moving aside the microscope. If there is shorting between the front and back gates, it often helps to cleave off the end of the sample. (See Section 2.2.1 and Fig. 2.7.)

A.1.9 Cleaving thin strips

First, a relatively deep groove is scribed on the edge of the sample frontside. The sample is turned over and a glass rod is used to apply pressure along the

desired cleave line, starting from where the groove on the other side is positioned. The rod may need to shifted a bit to find the right place.

A.1.10 Cleaving Sapphire

A nice edge is obtained by scribing (using a fiber-optic scribe) a deep groove on the edge of a piece of sapphire. The sample is turned over and pressure is applied with a glass rod. Thin pieces are made by scribing along the length of the sapphire and then by using the glass rod. Getting nice pieces requires practice.

A.1.11 Cutting ITO-coated glass

Glass does not cleave, so it must be scribed along the whole length. The scribing should be done on the glass side, not the ITO side.

A.1.12 Clipping on Sapphire or ITO

Both the QW sample and the sapphire/ITO should be quite clean. First, glue QW sample to sample mount, then immediately press sapphire/ITO on with tweezers. Slide around until interference fringes are visible. Then carefully clip down. The clip should not be pressing down over the edge of the sample mount.

A.1.13 Wire bonding

The wire bonding can be done by pressing small pieces of Indium onto the contact pads with a dental tool and then by pressing gold wire into the Indium. The other end of the wire is Indium soldered to pins attached to the sample mount. The ends of the wire can be cut off using a sharp scalpel.

A.2 Other Recipes

A.2.1 Al metallization

Al metallization is performed using either a shadow-mask or bi-layer photolithography. Either E-beam#3 or the thermal evaporator may be used.

A.2.2 Indium contacts

Indium contacts can be deposited just by pressing small pieces of Indium onto the sample. The Indium must be cleaned by scraping the oxide layer off with a scalpel followed by a solvent clean. The sample is then annealed at 400 °C for 1 minute in the strip annealer with 1 T Forming Gas.

A.2.3 Substrate Removal

The substrate can be selectively etched away if a stop-etch layer of high Al concentration is grown beneath the sample structure. The following recipe is for a slow etch using Citric acid, which gave the best results. Better, faster recipes may exist.

	Step	Notes
1	Mix 100 g Citric acid monohydrate with 100 ml DI at ∼40 °C	Mix until clear
2	Mix in 34 ml H_2O_2	
3	Glue sample frontside to host substrate	press and slide around to get interference fringes.
4	Wax sample onto slide	substrate facing out
5	Etch while stirring ∼20 hrs	wait for shiny surface
6	DI rinse	

Appendix B

Terahertz intensity measurements

This appendix explains how the THz intensity and power were measured for these experiments. The intensity inside the sample at the QW positions was actually the value of interest, but this could not be measured directly. Instead the intensity at the THz focus was calculated, and this value was typically used to compare spectra at different THz frequencies. Obtaining the THz intensity at the focus consisted of measuring the power before the OAP and measuring the THz spot size.

B.1 THz power

The THz power was measured with the Thomas Keating Terahertz Absolute Power/Energy Meter, known as the Thomas Keating. This meter is a photo-acoustic detector that uses a closed air-cell and a pressure transducer. The THz beam heats up a thin metal film in the air-cell, generating sound waves. One of the nice features of the Thomas Keating is that it can be calibrated by electrical heating of the metal film. This was performed by sending a voltage pulse to the metal film and measuring the detector response. The Thomas Keating output responds on a few ms timescale, so the response represented the total energy of the pulse. The Joule heating in the film was $U = V^2\Delta t/R$, where U is the heat generated, V is the voltage of the pulse, R is the film resistance, and Δt is the length of the pulse. The energy of the pulse was made comparable to the energy in a THz pulse from the FEL, and the pulses were generated with the same repetition rate as the the FEL. The calibration obtained was 1 mV peak output signal corresponded to $\sim$14.8 μJ absorbed. For measurements of THz power, one must take into account the transmission through the TPX windows and the fact that only $\sim$50% of the THz power is absorbed in the metal film. The energy incident on the Thomas Keating is then

$$U_{incident} = \frac{2U_{absorbed}}{T_{TPX}}, \tag{B.1}$$

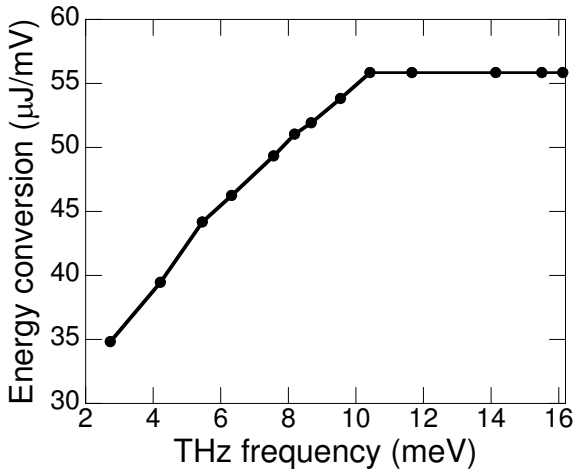

Figure B.1: Conversion factor from peak Thomas Keating signal (in mV) to incident THz pulse energy (in μJ) as a function of THz frequency.

where T_{TPX} is the transmission of TPX.

Based on a graph of the TPX transmission vs. THz frequency provided in the Thomas Keating manual, the conversion from the peak Thomas Keating voltage to incident THz energy was calculated and is plotted vs. THz frequency in Fig. B.1. The THz power was measured by placing the Thomas Keating before the OAP with the TPX window at Brewster's angle. The THz beam diameter was only $\sim$1.5 inches, so the entire beam fit in the detector window without any focusing. The power was calculated by dividing the pulse energy by the FWHM of the THz pulse as measured with the reference pyro. The pyro was used throughout THz EO measurements to monitor the power and could be calibrated using the Thomas Keating for each THz frequency used. The power sent to the reference pyro varied

THz freq. (meV)	Wavenumber (cm^{-1})	Typ. Power (kW)
2.7	22	2.1
4.2	34	0.38
5.5	44	0.45
6.3	51	1.5
7.6	61	1.3
8.2	66	1.9
8.7	70	1.1
9.5	77	0.86
10.4	84	1.9
11.7	94	1.2
12.8	103	0.86
14.1	114	1.4
15.5	125	0.58
16.1	130	0.57

Table B.1: Typical THz powers measured just before cryostat.

with THz frequency because of the frequency response of the beamsplitter. The typical power for a number of THz frequencies is listed in Table B.1.

B.2 THz spot size

The spot size of the THz beam at the focus was measured by mounting an aperture on an xyz stage near the THz focus, as determined by the FEL alignment laser. A pyro was placed behind the aperture, typically 200 μm in diameter, and the signal was peaked up until the aperture was at the focus. The aperture was scanned vertically and horizontally while measuring the pyro signal. (The size

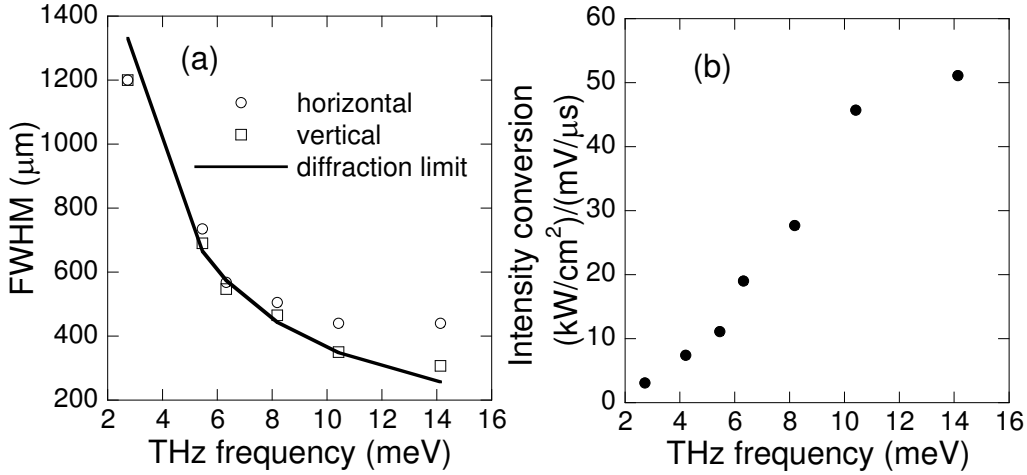

Figure B.2: (a) Measured FWHM of the THz focus horizontal (open circle) and vertical (open square). The solid line represents the diffraction limit assuming f/2.4 optics. (b) Calculated conversion factor from mV on Thomas Keating per μs to intensity in kW/cm^2 as a function of THz frequency.

of the NIR focus was determined this way as well.) The horizontal and vertical widths are displayed in Fig. B.2(a), along with the diffraction limited spot size for f/2.4 optics. The focus seems to be diffraction limited for $\hbar\omega_{THz} < \sim$8 meV. Past this frequency, astigmatism from the OAP appears to cause the spot to be more wide horizontally. At $\hbar\omega_{THz} = 2.7$ meV, the f/# was likely smaller than f/2.4 due to the increased beam diameter. From these measurements, the THz intensity at the focus was calculated by dividing the power by the area using the average of the horizontal and vertical FWHM for the diameter. The resulting conversion factor is plotted in Fig. B.2(b).

Appendix C

Sample information

Table C.1 summarizes the properties of the different samples used, and Fig. C.1 illustrates the experimental geometries used for each sample. The detailed layer structure for each sample follows these.

Sample	# active QWs	QW type	Gate QWs	DBR	Exp. Geom.
V5	3	150 Å square GaAs QWs, undoped	Y	Y	a
InTest5	10	143 Å square 6% InGaAs QWs, undoped	N	N	b
SC4	50	120/25/100 Å GaAs QWs, undoped	Y	N	c
SC9	10	120/25/100 Å GaAs QWs, doped $\sim 1.2 \times 10^{11}$ cm^{-2}	Y	Y	a
SC5	10	120/25/100 Å GaAs QWs, undoped	Y	Y	a
Triple QW2	10	Triple GaAs QWs doped $\sim 3 \times 10^{11}$ cm^{-2}	Y	Y	a

Table C.1: Summary of sample properties. The letters a, b, and c in the last column represent parts (a), (b), and (c) of Fig. C.1.

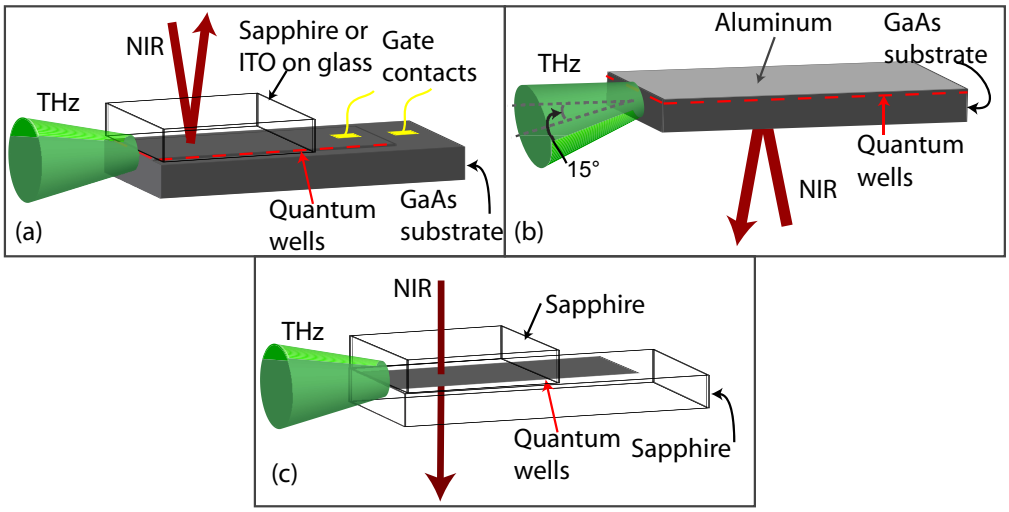

Figure C.1: Experimental geometries used for THz EO experiments.

C.1 V5

Sample V5 (030404B) was grown by Andrew Huntington on 4/4/03. It consists of 3 150 Å undoped GaAs QWs in-between 2 doped gate QWs, with a DBR behind.

thickness (Å)	layer	
100	GaAs	
600	30% AlGaAs	
	1×10^{12} Si δ-doping	
100	30% AlGaAs	
80	GaAs	Front gate
500	30% AlGaAs	
3766	30% AlGaAs	
300	30% AlGaAs	
150	GaAs	
300	30% AlGaAs	
150	GaAs	Active QWs
300	30% AlGaAs	
150	GaAs	
300	30% AlGaAs	
3970	30% AlGaAs	
500	30% AlGaAs	
80	GaAs	Back gate
100	30% AlGaAs	
	1×10^{12} Si δ-doping	
100	30% AlGaAs	
1600	30% AlGaAs	
682	99% AlGaAs	DBR
600	30% AlGaAs	($\times$ 30)
	S. I. GaAs substrate	

C.2 InTest5

Sample InTest5 (040806A) was grown by Chad Wang on 8/6/04. It consists of 10 undoped $In_{0.065}Ga_{0.935}As$ QWs with $Al_{0.3}Ga_{0.7}As$ barriers.

thickness (Å)	layer	
500	GaAs	
200	30% AlGaAs	
150	6.5% InGaAs	x-ray data: 6.4% In, 143 Å
300	30% AlGaAs	x-ray data: 30% Al, 295 Å
	$\times$ 10	
	S. I. GaAs substrate	

C.3 SC4

Sample SC4 (021212E) was grown by Micah Hanson on 12/12/02. It consists of 50 undoped asymmetric, coupled, GaAs QWs in-between two doped gate QWs, with a 1 μm stop-etch layer behind.

thickness (Å)	layer	
100	GaAs	
300	30% AlGaAs	
100	30% AlGaAs doped 2×10^{18} cm^{-3}	
100	30% AlGaAs	
70	GaAs	Front gate
2800	30% AlGaAs	
120	GaAs	
25	20% AlGaAs	
100	GaAs	Active wells
200	30% AlGaAs	($\times$ 50)
2700	30% AlGaAs	
70	GaAs	Back gate
100	30% AlGaAs	
100	30% AlGaAs doped 1×10^{18} cm^{-3}	
1000	30% AlGaAs	
10000	70% AlGaAs	Stop etch
	S. I. GaAs substrate	

C.4 SC9

Sample SC9 (040517A) was grown by Micah Hanson on 5/17/04. It consists of 10 doped asymmetric, coupled, GaAs QWs in-between two doped gate QWs, with a DBR behind.

thickness (Å)	layer	
100	GaAs	
500	30% AlGaAs	
	2×10^{12} Si δ-doping	
100	30% AlGaAs	
70	GaAs	Front gate
9280	30% AlGaAs	
	1.5×10^{11} Si δ-doping	half this for first layer
460	30% AlGaAs	
120	GaAs	
25	20% AlGaAs	Active QWs
100	GaAs	($\times$ 10)
460	30% AlGaAs	
	0.75×10^{11} Si δ-doping	
3003	30% AlGaAs	
70	GaAs	Back gate
100	30% AlGaAs	
	2×10^{12} Si δ-doping	
1000	30% AlGaAs	
675	AlAs	DBR
595	30% AlGaAs	($\times$ 30)
	S. I. GaAs substrate	

C.5 SC5

Sample SC5 (030405A) was grown by Andrew Huntington on 4/05/03. It consists of 10 undoped asymmetric, coupled, GaAs QWs in-between two doped gate QWs, with a DBR behind.

thickness (Å)	layer	
100	GaAs	
500	30% AlGaAs	
100	30% AlGaAs doped 2×10^{18} cm^{-3}	
100	30% AlGaAs	
70	GaAs	Front gate
5341	30% AlGaAs	
205	30% AlGaAs	
120	GaAs	
25	20% AlGaAs	Active QWs
100	GaAs	($\times$ 10)
205	30% AlGaAs	
2539	30% AlGaAs	
70	GaAs	Back gate
100	30% AlGaAs	
100	30% AlGaAs doped 1×10^{18} cm^{-3}	
1000	30% AlGaAs	
679	AlAs	DBR
597	30% AlGaAs	($\times$ 30)
	S. I. GaAs substrate	

C.6 TripleQW2

Sample TripleQW2 (040816A) was grown by Micah Hanson on 8/16/04. It consists of 10 doped, triple, GaAs QWs in-between two doped gate QWs, with a DBR behind.

thickness (Å)	layer	
100	GaAs	
500	30% AlGaAs	
	2×10^{12} Si δ-doping	
100	30% AlGaAs	
70	GaAs	
9280	30% AlGaAs	
	3×10^{11} Si δ-doping	half this for first layer
427.5	30% AlGaAs	
92	GaAs	
26	20% AlGaAs	
88	GaAs	Active QWs
26	20% AlGaAs	($\times$ 10)
78	GaAs	
427.5	30% AlGaAs	
	1.5×10^{11} Si δ-doping	
3003	30% AlGaAs	
70	GaAs	Back gate
100	30% AlGaAs	
	2×10^{12} Si δ-doping	
1000	30% AlGaAs	
672.5	AlAs	DBR
592.8	30% AlGaAs	($\times$ 30)
	S. I. GaAs substrate	

Appendix D

Coupled Wave Equations Derivation

The coupled wave equations for sum-frequency generation can be derived from Maxwell's equaions for a medium with no free charge:

$$\nabla \cdot \vec{D} = 0 \tag{D.1}$$

$$\nabla \cdot \vec{B} = 0 \tag{D.2}$$

$$\nabla \times \vec{E} = -\frac{\partial \vec{B}}{\partial t} \tag{D.3}$$

$$\nabla \times \vec{H} = \frac{\partial \vec{D}}{\partial t} \tag{D.4}$$

The constituent relations can be written as

$$\vec{B} = \mu_0 \vec{H} \tag{D.5}$$

$$\vec{D} = \epsilon_0 \vec{E} + \vec{P} = \epsilon \vec{E} + \vec{P}^{nonlin}, \tag{D.6}$$

where $\epsilon/\epsilon_0 = 1 + \chi^{(1)}$. Taking the curl of Eq. A.3 and substituting in Eq. A.4 and A.6 gives

$$\nabla \times \nabla \times \vec{E} = \nabla(\nabla \cdot \vec{E}) - \nabla^2 \vec{E} = -\mu_0 \epsilon(\omega) \frac{\partial^2 \vec{E}}{\partial t^2} - \mu_0 \frac{\partial^2 \vec{P}^{nonlin}}{\partial t^2}. \tag{D.7}$$

For an isotropic medium, $\nabla \cdot \vec{E} = 0$ (not so valid for QWs), Eq. A.7 can be simplified to

$$\nabla^2 \vec{E} - \frac{\epsilon(\omega)}{\epsilon_0 c^2} \frac{\partial^2 \vec{E}}{\partial t^2} = \frac{1}{\epsilon_0 c^2} \frac{\partial^2 \vec{P}^{nonlin}}{\partial t^2}. \tag{D.8}$$

This is the wave equation with a source.

For an electromagnetic wave of frequency ω travelling in a nonlinear medium in the $\vec{k}$-direction, the cartesian components of the electric field and polarization at steady-state can be written as

$$E_i(\vec{r}, t) = \mathrm{Re}\left\{ \tilde{E}_i(\vec{r}) e^{i(\vec{k}\cdot\vec{r} - \omega t)} \right\} \tag{D.9}$$

$$P_i^{nonlin}(\vec{r}, t) = \mathrm{Re}\left\{ \tilde{P}_i(\vec{r}) e^{i(\vec{k}'\cdot\vec{r} - \omega t)} \right\}, \tag{D.10}$$

where $\tilde{E}_i(z)$ and $\tilde{P}_i(z)$ are envelope functions. Plugging these expressions into Eq. (D.8) gives

$$\left(-k^2 \tilde{E}_i + 2i(\vec{k} \cdot \nabla)\tilde{E} + \nabla^2 \tilde{E}_i + \frac{\epsilon(\omega)\omega^2 \tilde{E}_i}{\epsilon_0 c^2} \right) e^{i(\vec{k}\cdot\vec{r} - \omega t)} = -\frac{\omega^2 \tilde{P}_i}{\epsilon_0 c^2} e^{i(\vec{k}'\cdot\vec{r} - \omega t)} \tag{D.11}$$

Since $k^2 = \epsilon^{(1)}(\omega)\omega^2/(\epsilon_0 c^2)$, the real part of the fourth term and the first term cancel out ($\epsilon = \epsilon^{(1)} + i\epsilon^{(2)}$). Also, in the slowly varying envelope approximation

(SVEA), changes in $\tilde{E}$ occur over distances much larger than the wavelength. This allows terms like $\nabla^2\tilde{E}_i$ to be dropped. It is not clear that the SVEA is valid considering the width of the QW layers is less than one wavelength. However, as long as the result in the SVEA shows only small changes in $\tilde{E}$, the approximation is probably valid. In this case, Eq. (D.8) can be written as

$$(\hat{n}\cdot\nabla)\tilde{E}_i + \alpha(\omega)\tilde{E}_i = \frac{i\omega^2\tilde{P}_i e^{i(\vec{k}'-\vec{k})\cdot\vec{r}}}{2k\epsilon_0 c^2}, \tag{D.12}$$

where $\alpha(\omega) = \epsilon^{(2)}(\omega)\omega^2/(2k\epsilon_0 c^2)$ is the absorption coefficient and $\vec{k} = k\hat{n}$.

In the case of $n = +1$ sideband generation, there are three frequency components to consider. The incident NIR beam propagates in the z-direction polarized in the x-direction. The THz beam propagates in the x-direction polarized in the z-direction. The propagation direction and polarization of the sideband are unknown. The polarization must satisfy

$$\tilde{P}_{SB,x}e^{i(\vec{k}'_{SB}\cdot\vec{r}-\omega_{SB}t)} = 2\epsilon_0\chi^{(2)}_{xzx}\tilde{E}_{NIR}e^{i(k_{NIR}z-\omega_{NIR}t)}\tilde{E}_{THz}e^{i(k_{THz}x-\omega_{THz}t)}. \tag{D.13}$$

This means that $\vec{k}'_{SB} = k_{NIR}\hat{z} + k_{THz}\hat{x}$ and $\omega_{SB} = \omega_{NIR} + \omega_{THz}$, as expected from momentum and energy conservation, respectively. The electric field wavevector $\vec{k}_{SB}$ is assumed to be in the same direction as the polarization wavevector $\vec{k}'_{SB}$ as this should minimize phase mismatch. When Eq. (D.12) is applied to the x-component of $\tilde{E}_{SB}$, we obtain

$$\frac{d\tilde{E}_{SB}}{dz} + \alpha(\omega_{SB})\tilde{E}_{SB} = \frac{i\omega^2_{SB}}{k_{SB}c^2}e^{i\Delta k\hat{n}_{SB}\cdot\vec{r}}\chi^{(2)}_{xzx}(\omega_{NIR}+\omega_{THz})\tilde{E}_{NIR}\tilde{E}_{THz}, \tag{D.14}$$

where $\Delta k = \sqrt{k_{NIR}^2 + k_{THz}^2} - k_{SB} \simeq k_{NIR} - k_{SB}$. Equation (D.14) has been simplified by noting that $k_x \ll k_z$ for the sidebands. The derivative with respect to x was thus ignored and k_z was replaced with k. One problem with this expression is that it results in a sideband wavevector that is not perpendicular to the polarization.

An equation similar to Eq. (D.14) can be written for the NIR beam:

$$\frac{d\tilde{E}_{NIR}}{dz} + \alpha(\omega_{NIR})\tilde{E}_{NIR} = \frac{i\omega_{NIR}^2}{k_{NIR}c^2} e^{-i\Delta k \hat{n}_{SB}\cdot\vec{r}} \chi_{xzx}^{(2)}(\omega_{SB} - \omega_{THz})\tilde{E}_{SB}\tilde{E}_{THz}^*, \quad \text{(D.15)}$$

If we assume that $\tilde{E}_{THz}$ is constant over the area of interest and that $\tilde{E}_{NIR}$ is little affected by the nonlinear interaction, then Eq. (D.14) and D.15 can be written as

$$\tilde{E}_{NIR} = A_0 e^{-\alpha(\omega_{NIR})z} \quad \text{(D.16)}$$

$$\frac{d\tilde{E}_{SB}}{dz} + \alpha(\omega_{SB})\tilde{E}_{SB} = \frac{i\omega_{SB}^2}{k_{SB}c^2}\chi_{xzx}^{(2)}\tilde{E}_{THz}A_0 e^{-\alpha(\omega_{NIR})z + i\Delta kz}, \quad \text{(D.17)}$$

where $\Delta k \hat{n}_{SB}\cdot\vec{r}$ has been approximated as Δkz. The solution is

$$\tilde{E}_{SB}(z) = \frac{1}{\Delta\alpha + i\Delta k}\frac{ik_{SB}}{n_{SB}^2}\chi_{xzx}^{(2)}\tilde{E}_{THz}A_0(e^{(-\alpha(\omega_{NIR})+i\Delta k)z} - e^{-\alpha(\omega_{SB})z}), \quad \text{(D.18)}$$

where $\Delta\alpha = \alpha(\omega_{SB}) - \alpha(\omega_{NIR})$. If absorption and phase-matching are ignored, we obtain

$$\frac{\tilde{E}_{SB}}{A_0} = \frac{ik_{SB}}{n_{SB}^2}\chi_{xzx}^{(2)}\tilde{E}_{THz}z. \quad \text{(D.19)}$$

Equations (D.18) and (D.19) can be used to evaluate the expected sideband conversion for a given QW structure. The conversion will be equal to $(n_{SB}/n_{NIR})(\tilde{E}_{SB}/A_0)^2$.

An expression for $n = +2$ sidebands can be obtained in a similar fashion.

$$\tilde{E}_{SB}^{n=+2}(z) = \frac{1}{\Delta\alpha + i\Delta k}\frac{3ik_{SB}}{2n_{SB}^2}\chi_{xzzx}^{(2)}\tilde{E}_{THz}^2 A_0(e^{(-\alpha(\omega_{NIR})+i\Delta k)z} - e^{-\alpha(\omega_{SB})z}). \quad \text{(D.20)}$$

Appendix E

Low-frequency modulation derivation

When a quantum well is driven by a low-frequency field ($\Omega \ll \gamma$), the change in the susceptibility can be understood in terms of a quasi-static modulation of the exciton line. The susceptibility of a single exciton line can be written as

$$\chi(\omega_{NIR}) = \frac{1}{\hbar^2 A w \epsilon_0} \frac{|\mu_{01}|^2}{\omega_{10} - \omega_{NIR} - i\gamma_{10}}, \tag{E.1}$$

where A and w are the QW area and width, μ_{01} is the interband matrix element, $\hbar\omega_{10}$ is the exciton energy, and γ_{10} is the dephasing rate. The exciton energy is of course a function of the electric field E. The effect of a small amplitude electric

field, $\delta E\cos(\Omega t)$, on the susceptibility can be written as

$$\chi = \chi(E_0) + \frac{d\chi}{dE}\Big|_{E_0} \delta E\cos(\Omega t), \tag{E.2}$$

with

$$\frac{d\chi}{dE} = \frac{1}{\hbar^2 A w \epsilon_0}\frac{-|\mu_{01}|^2\omega'_{10}(E_0)}{(\omega_{10}-\omega_{NIR}-i\gamma_{10})^2}, \tag{E.3}$$

where $\omega'_{10}(E_0) = (d\omega_{10})/(dE)|_{E_0}$. The NIR field propagating through the QW layers can be written as

$$E_{NIR} = A_0 e^{i(k_0 z-\omega_{NIR}t)}e^{-\alpha_0 z}\exp\left(i\frac{\omega_{NIR}}{2n_0 c}\chi(t)z\right), \tag{E.4}$$

where k_0, α_0, n_0 are the NIR wavevector, absorption, and index of refraction in the absence of the drive field. $\chi(t)$ is the time dependent part of χ. The approximation that $\chi(t) \ll \chi(E_0)$ has been made to simplify this equation. Since $\omega_{NIR}\chi(t)z/(2n_0c) \ll 1$, Eq. (E.4) can be simplified to

$$E_{NIR} = A_0 e^{i(k_0 z-\omega_{NIR}t)}e^{-\alpha_0 z}\times$$
$$\left[1 + i\frac{\omega_{NIR}}{2n_0 c}\frac{1}{\hbar^2 A w\epsilon_0}\frac{-|\mu_{01}|^2\omega'_{10}(E_0)}{(\omega_{10}-\omega_{NIR}-i\gamma_{10})^2}z\delta E\cos(\Omega t)\right]. \tag{E.5}$$

In the presence of the driving field, new frequency components arise in E_{NIR}. The $\omega_{NIR}+\Omega$ component is

$$E(\omega_{NIR}+\Omega) = A_0 e^{-\alpha_0 z}\frac{i\omega_{NIR}}{n_0 c}z\delta E\zeta(\omega_{NIR}), \tag{E.6}$$

where

$$\zeta(\omega_{NIR}) = \frac{1}{4\hbar^2 A w \epsilon_0} \frac{-|\mu_{01}|^2 \omega'_{10}(E_0)}{(\omega_{10} - \omega_{NIR} - i\gamma_{10})^2} \tag{E.7}$$

Equation (E.6) looks identical to Eq. A.18, derived from the coupled wave equations, with $\Delta\alpha = \Delta k = 0$. Equation (E.7) is very similar to what would be obtained using the low frequency term of Eq. (4.8) with $\omega_{THz} = 0$. The difference is that μ_{11} is replaced by ω'_{10}, and there is a factor of 1/4 instead of 1/2. Using the exciton model described in Chapter 4, $\omega'_{10} \simeq -17.4$ eÅ at 10 kV/cm, while $\mu_{11} \simeq -22$ eÅ. Thus, the sideband signal is predicted to be smaller in this quasi-static calculation. This inconsistency is not understood, but certainly the $\chi^{(2)}$ model approaches a very similar function as the quasistatic calculation at low frequencies.

Appendix F

Heat transfer in Gallium Arsenide

This appendix models heating of a GaAs sample with an Aluminum layer deposited on the surface. Heating of the Aluminum layer is assumed to dominate over heating of the GaAs lattice. First, the temperature in the sample will be modelled while the THz pulse is on, as displayed schematically in Fig. F.1. The sample is represented as an infinite sheet of width c with a constant heat source on one side of the sample. Loss of heat due to conduction to the cold finger or through radiation is assumed to be negligible during the pulse.

If the temperature of the sample at position x at time t is represented by

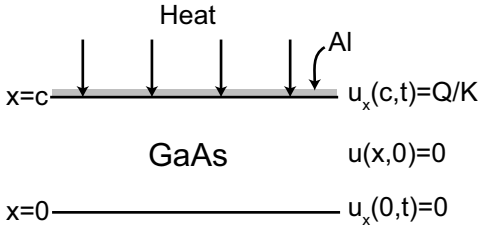

Figure F.1: Diagram of THz heating of Aluminum layer on GaAs sample. Boundary conditions and initial conditions are specified.

$u(x,t)$, then this function must satisfy the one-dimensional diffusion equation,

$$u_t(x,t) = ku_{xx}(x,t), \tag{F.1}$$

where u_t is the partial derivative of u with respect to time and u_{xx} is the second partial derivative of u with respect to position. The thermal diffusivity, k, can be written as $k = K/(\rho\sigma)$, where K is the thermal conductivity, ρ is the density, and σ is the specific heat. For GaAs at 10 K, $K \approx 20$ W/cmK, $\sigma \approx 1.5 \times 10^{-3}$ J/gK, and $\rho = 5.32$ g/cm^3, giving a value of $\sim$2500 cm^2/s for k. (The values of K and σ are not very certain. See Ref. [76].)

The boundary conditions are displayed in Fig. F.1. The condition $u_x(0,t) = 0$ means that no heat passes through the $x = 0$ boundary (a good assumption since this side of the sample is not touching anything). The condition $u_x(c,t) = Q/K$ means that a constant heat flux Q is entering the sample at the boundary $x = c$ where the Aluminum is located. The initial condition $u(x,0) = 0$ means that the initial temperature is uniform (the actual value is arbitrary, so 0 is chosen).

This problem can be solved by defining $u(x,t) = U(x,t) + f(x)$, where $f(x)$ is chosen so that $U_x(0,t) = U_x(c,t) = 0$. This gives boundary conditions that allow the differential equation for $U_x(x,t)$ to be solved using separation of variables. However, the differential equation becomes inhomogeneous. The solution can be found by expanding $U_x(c,t)$ in a Fourier series. The result is

$$\begin{aligned} u(x,t) = \quad & \tfrac{kQt}{Kc} + \textstyle\sum_{n=1}^{\infty} \tfrac{-2Qc(-1)^n}{K(n\pi)^2} \exp\left[-k\left(\tfrac{n\pi}{c}\right)^2 t\right] \cos\left(\tfrac{n\pi x}{c}\right) \\ & + \tfrac{Q}{2Kc}x^2 - \tfrac{Q}{6K}c. \end{aligned} \tag{F.2}$$

Based on this equation, the time scale over which the temperature changes across the sample is $\tau = (c/\pi)^2/k$, which is $\sim$70 ns for $c = 400$ μm. This is surprisingly fast! Equation (F.2) can easily be shown to satisfy Eq. (F.1) and the boundary conditions. Figure F.2(a) plots Eq. (F.2) for a series of times. At $t = 0$, just when the heating begins, the temperature is uniform at 10 K. The sample heats up at later times, with the side close to the heat source at a higher temperature. The heat source Q is set to 1.5 kW/cm^2 to give an increase in temperature comparable to that observed experimentally for full THz power. This corresponds to $\sim$0.15% absorption of a THz beam with an intensity of 1 MW/cm^2. After about 100 ns, the summation in Eq. (F.2) can effectively be ignored due to the exponential, so the solution is really quite simple.

After the THz pulse is over, the temperature should become uniform very

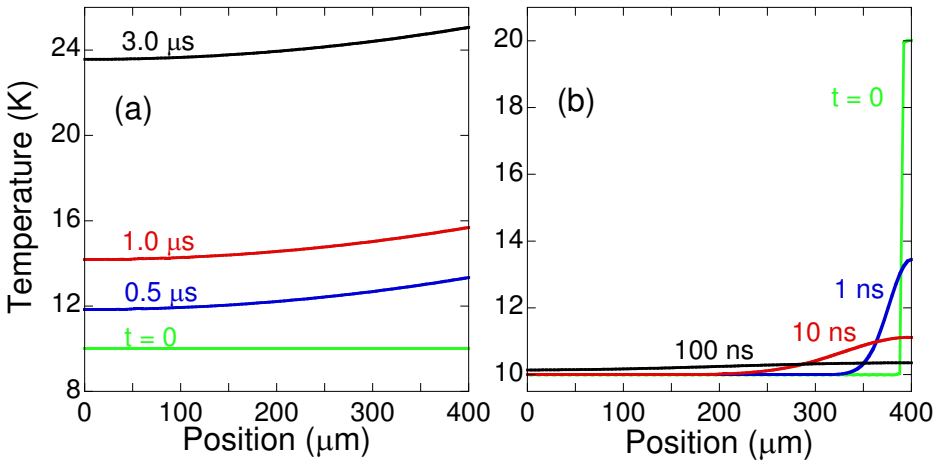

Figure F.2: Simulated temperature as a function of position for a series of times. In (a) there is a heat source at $x = 400$ μm, which starts at $t = 0$. In (b) the temperature is much higher close to the $x = 400$ μm side at $t = 0$.

quickly, on a time scale of ∼70 ns. To illustrate, the temperature distribution is calculated for a sample with one side initially at a higher temperature in Fig. F.2(b). The temperature is fairly uniform after only 100 ns.

These calculations imply that when a THz pulse heats up the Aluminum on a GaAs sample, the temperature distribution during the pulse should give a higher temperature near the Aluminum, where the QWs are located. The temperature after the THz pulse should become uniform after a few 100 ns, causing the temperature at the QWs to drop. (On much longer time scales, the temperature of the sample will of course lose heat to the cold finger.) Based on Fig. F.2(a), the drop should be quite small for pulses of 3 μs. However, one can imagine that under some conditions (or using different thermal constants) the temperature drop

at the QWs could be more significant. This effect means that measurements of the temperature (through shifts in absorption) a few μs after the THz pulse do not necessarily represent the temperature during the THz pulse.

Appendix G

Experimental Procedures

G.1 Equipment instructions

G.1.1 Cryostat

The cryostat is a CTI Cryogenics Model 22 closed-cycle Helium refrigerator that can cool down to ∼10 K in about an hour. The cryostat is connected to a CTI Cryogenics Model 8200 Helium compressor through two high pressure Helium lines. It is also connected to the controller built into the compressor and to a Lakeshore 330 temperature controller. The sample is glued to a rectangular piece of copper that is screwed to a copper mount attached semi-permanently to the cryostat cold finger. A little bit of Apiezon vacuum grease applied between

these pieces can improve thermal conduction and lower the base temperature. A Lakeshore temperature diode can be screwed to the sample mount, and insulated Nichrome heater wire is wrapper around the semi-permanent copper mount. A voltage can be applied to samples by connecting the pins glued to the sample mount to the 10 wires with pins soldered on the ends, each labelled by a letter. Teflon tape is used to secure the wires to the semi-permanent copper mount. The cryostat is mounted on two translation stages for lateral motion and on a labjack for vertical motion.

Instructions for cool down

1. Evacuate cryostat to less than $\sim 2 \times 10^{-6}$ T. This may only take 2 to 3 hours, but overnight is good.

2. Turn on cooling water for the compressor.

3. Turn on compressor, wait until cold. (Continue pumping on the cryostat during the cool down until just above 77 K. (May want to leave the valve slightly open until at $\sim$12 K.)

The cryostat can stay cold for 2 to 3 days before it starts to warm up. Occasionally, the temperature starts creeping up really soon after cooling down. This problem can be fixed by pumping on the cryostat again for just a few minutes (make sure

the pressure is low before opening the valve between the pump and cryostat). I have found that the temperature stays pretty stable at ∼10 K without temperature regulation, but the heater can certainly be used with the temperature controller. At times, we found that the heater caused some kind of outgassing that would cause the temperature to creep up. This problem seems to be fixed now since the heater wire is glued to the copper mount using Stycast 2850 instead of teflon tape.

To warm up the cryostat, turn off the compressor and the cooling water. Warm up takes several hours.

Maintenance

The Helium pressure in the compressor must be maintained at 250 psi. Occasionally there is a need to add additional Helium to the compressor. The procedure for this can be found in the manual, but a high-pressure regulator and a special flared fitting needs to be used. These should be found in the lab. Occasionally decontamination must be performed (see the manual). There is a "T" that can be connected to a Helium bottle for this purpose. Also, there is a compressor adsorber that is supposed to be changed every 12 months. I don't think it needs to be changed this often because the cryostat is not used that heavily.

G.1.2 Argon laser (Coherent Innova 300)

The Argon laser puts out up to 12 W of power at multiple lines in the blue. It must be cooled with several gallons per minute of deionized water from the Coherent heat exchanger, which is cooled by the building water. For pumping the Ti:Sapphire, the Argon laser is run at ∼6.5 W (light regulated) using ∼48 amps with aperture number 8. The Argon laser should be run for at least an hour every couple weeks at about this power. When it is turned on, it should usually be run for at least a half an hour at this kind of power.

Instructions for turning on

First of all, be careful with this laser. It puts out a lot of power!

1. Turn on building cooling water, heat exchanger
2. Turn on circuit breaker
3. Enable laser with key
4. Make sure laser blocked or going to Ti:Sapphire
5. Set to current regulation, 40 amps, turn on
6. Wait ∼15 minutes for laser to stabilize
7. Increase current to ∼48 amps, set to light regulation at 6.5 W.

Instructions for turning off

1. Record info in log book
2. Set to current regulation, turn down to 40 amps
3. Turn off
4. disable laser with key
5. Turn off circuit breaker
6. Wait ∼10 minutes for laser to cool off
7. Turn off heat exchanger, building cooling water

Maintenance

A rebuilt laser tube was installed in the summer of 2002 by Laser Innovations, so it may need to be replaced in the near future. Sometimes the power needs to be peaked up by pressing the "Tune" button and adjusting the knobs on the back end of the laser. At one point the power became quite unstable and would not regulate the power well. Sometimes this may mean that the output coupler or the windows need to be cleaned with methanol (see manual). It turned out that the Brewster window was actually dirty and was heating up. We cleaned it using ABF (ammonium bifluoride), which worked really well. (ABF is similar to HF,

so be careful). Laser Innovations is a good place to call when you need help or repairs.

G.1.3 Titanium:Sapphire laser (Coherent 890)

The Ti:Sapphire is a cw laser that in principle can be tuned from 675 nm to 1100 nm, providing up to ∼1 W of power. Typically, it puts out 400 to 500 mW when pumped by the Argon laser with 6.5 W. It is tuned by rotating a birefringent filter using a computer controlled Newport motion controller/linear actuator. There are 4 to 8 cm^{-1} jumps in the tuning, which don't seem possible to eliminate. As the tuning crystal rotates, the wavelength continues making these steps until it moves out of the good tuning range. The wavelength will then jump from one end of the tuning range to the other. The output coupler can be changed to determine the wavelength range it operates at. I have only used the "short" and "mid" range output couplers. The "short" output coupler range is about 735 nm to 820 nm, and the "mid" range is about 780 nm to 870 nm. Perhaps these ranges can be extended by better alignment.

Turning on and off the Ti:Sapphire is controlled by turning on and off the Argon laser. Deionized cooling water from the heat exchanger is also sent to the Ti:Sapphire. (This must be turned off if the Argon laser is run without the Ti:Sapphire or water may condense on the Sapphire crystal.) After the laser has

warmed up for at least 15 minutes, the laser power can be peaked up by adjusting the two knobs on the end of the laser (above the output). This doesn't change the beam alignment.

The linear actuator that controls the laser wavenumber should always be sent to a fixed position when turning off the laser just in case the power to the motion controller goes out (it loses the position). The Newport motion controller should always be left on. Values for the laser power and wavenumber should be recorded in the log book.

Labview vi's

1. `Encoder Mike.vi`: Moves Newport linear actuator (we previously used an actuator called "encoder mike") to change Ti:Sapphire wavenumber.

2. `Encoder Mike INIT.vi`: Initializes Newport motion controller, sets position using `Encoder Mike global`. Must be run after power-cycling motion controller.

3. `Encoder Mike GLOBAL`: Global Labview variable that keeps track of the linear actuator position.

4. `Ti:S calibrator2.vi`: Scans the linear actuator while measuring the wavenumber. Useful for checking step size, laser tuning.

5. `Find wavenumber.vi`: Iteratively seeks out a laser wavenumber.

Maintenance

Sometimes the alignment needs to be tweaked to peak up the power. The cover must be taken off and laser goggles should be worn. Adjust the upper and lower cavity mirrors (see manual) to peak up the power. More detailed procedures are in the manual. Sometimes it is a good idea to clean some of the optics with methanol at this time (see manual).

Improving the tuning range and tuning jumps is tricky. The jumps can sometimes be improved by rotating the Sapphire crystal about the vertical axis. This is done by loosening a clamp on the crystal mount and rotating by hand (with the Argon laser aperture closed), so precise, reproducible changes are impossible. The power must be peaked up again after each adjustment. Sometimes a rotation about the horizontal axis can significantly improve the power and the tuning range as well. It may be a good idea to have a Coherent service call if the tuning poses too much of a problem.

The output couplers can be changed pretty easily as outlined in the manual. Only the output coupler needs to be changed. The power will have to be peaked up after the change.

G.1.4 Wavelength meter

The New Focus Fizeau wavelength meter is used to monitor the wavelength of the Ti:Sapphire. A beam splitter sends ∼100 mW of the laser to the wavelength meter. (The polarization should be vertical.) This much power is not needed, but there is plenty of power to spare. There is an alignment laser inside the wavelength meter activated by pushing the `Mode` button. Once the Ti:Sapphire is aligned with the alignment laser, the meter displays a measure of how big the signal is as a % of the maximum and a measure of the uniformity of illumination of the CCD detector. The signal should be peaked up using only small adjustments. An OD1 filter (at least) should be placed before the input. Focusing of the beam into the input aperture is not necessary. (Focusing can cause the measured wavelength to jump around.) The wavelength meter is left on all the time.

Labview vi's

1. `Wavelength Meter.vi`: Reads the laser wavenumber.

2. `wavemeter setup.vi`: Initializes the wavelength meter. Must be run after power-cycle.

G.1.5 Acousto-optic modulator

An IntraAction AOM-602N acousto-optic modulator (AOM) is used to pulse the NIR beam. The AOM forms a pressure grating using an RF source (IntraAction Model ME signal processro) that diffracts the NIR beam. The RF source is turned on and off with a trigger–forming a pulse in the diffracted signal. (Make sure the RF cable doesn't get to close to any signal cables.) For alignment, the laser should first be sent straight through the AOM aperture. Then, look for the first-order diffracted beam while making slight adjustments to the incident angle. Maximize the first order beam until there is a hole in the zero order beam.

G.1.6 SPEX Monochromator

The SPEX 0.85 m double monochromator is used for sideband experiments and when high resolution is needed. I have seen the resolution go down to $\sim$0.3 cm^{-1}, but it could probably be even better. Inside, there are two 1800 lines/mm holographic gratings, 5 mirrors, and two apertures, so only about 10% of the light entering the SPEX reaches the exit slit. The light should be horizontally polarized or the efficiency is much worse. The slits are usually set to 400 μm, giving a resolution of $\sim$1 cm^{-1}. (Usually the entrance slit is set to 100 μm to ensure the NIR beam is coming to a good focus at the slit.)

Alignment is performed by first sending a laser into the monochromator with no focusing lens. Adjust the beam to get maximum power through the slit and so that it is centered on the first mirror. (There are white mirror covers under the SPEX that can be used for this purpose.) The laser should also be centered vertically on the slit. Then, put in the lens and adjust to get maximum power through the slit while keeping the beam centered on the first mirror. The laser should then be aligned. Check that the laser makes it all the way to the exit slit, and make sure that it is centered where the detector will be (don't let the beam actually hit the detector). If the beam is way off, either the alignment into the SPEX is bad or the SPEX itself is misaligned (bad news). After the laser is aligned into the SPEX, place two irises in the beam path to align with in the future.

The output wavelength of the SPEX is controlled by a SPEX MSD Mini-step-driver, which is interfaced through the SPEX 232/488RET GPIB Controller . These are left on all the time. There is a counter on the side of the SPEX that shows what wavenumber it is at. This wavenumber can only controlled by computer, using the Labview vi's in the next section. The SPEX should only be scanned from high to low wavenumbers.

Labview vi's

1. `SPEX init.vi`: Initializes SPEX communications and wavenumber.
2. `SPEX global`: Global Labview variable that keeps track of the SPEX wavenumber.
3. `SPEX read position.vi`: Reads SPEX wavenumber from SPEX GPIB controller. Use when Labview is restarted.
4. `SPEX goto wavenumber.vi`: Moves SPEX to desired wavenumber.

G.1.7 Photomultiplier Tube

A Hamamatsu R7400U-20 photomultiplier tube (PMT) detector was mounted on the SPEX for most of the experiments. A PMT was used due to its high noise-free gain ($\sim 10^6$) needed for these measurements. The photocathode for this PMT is multialkali, which gives a quantum efficiency of $\sim$10% at 800nm. The efficiency dies off rapidly past $\sim$830 nm. Cooled GaAs PMTs could probably give a somewhat better signal to noise, but GaAs PMTs cannot tolerate much power and are more expensive.

A voltage of -900 V was applied to the PMT anode from an SRS high voltage source. The output current was sent to an SRS preamp shunted by a 10 kΩ resistor. This resistor made the time constant a few μs.

G.1.8 Acton Monochromator/Intensified CCD

An Acton 0.275 meter triple grating monochromator with a Princeton Instruments intensified CCD (ICCD) was used for experiments as well. The monochromator has two switchable gratings, 1200 lines/mm and 300 lines/mm. The best resolution obtained for the 1200 lines/mm grating was $\sim$4 cm^{-1} (0.5 meV) with the slits at about 50 μm. An ICCD is attached to the monochromator. This detector is similar to a PMT in that it amplifies electrons ejected from a photocathode, but it provides an entire spectrum at once using the CCD. The signal is intensified when a high-voltage pulse is applied to the detector. This pulse is also used to gate the detection on time scales as short as a few ns. The ICCD is cooled with a TE-cooler, reducing dark counts.

Operation instructions

1. Open Nitrogen valve to purge ICCD

2. Turn on small chiller, building cooling water

3. Turn on PI Detector controller along with the cooler switch, wait for `status` LED to turn green.

4. Block monochromator, turn on PI Pulse Generator Model PG-200.

5. Connect external trigger to PI pulse generator or use internal trigger

6. Set pulse gate width and gate delay.

7. Set center wavelength and grating of monochromator using Acton Spectradrive Stepping Motor Scan Controller.

8. Run Labview vi: `ICCD Front Panel.vi` (or similar). Select `init CCD` the first run.

9. Unblock monochromator. If saturated (counts $>$ 16000), immediately block monochromator and reduce gate width.

There is an output on the back of the PI pulse generator (monitor gate 1) which provides a reference for the gate pulse. This can be used to ensure the pulse timing is correct.

Labview vi's

1. `ICCD Front Panel.vi`: Reads spectrum from ICCD, performs averages.

   (a) Enter center wavelength and grating of monochromator and the desired display units (nm or cm^{-1})

   (b) Select `background` and `init CCD` buttons. (Leave other buttons at default settings.)

(c) Enter 0 for the number of averages

(d) Deselect the `Hold here to stop after averaging` button

(e) Run the program, block input to monochromator

(f) Enter number of averages, select `Hold here to stop after averaging` button, wait for measurement to end.

(g) Run the program again with `background` and `init CCD` buttons deselected (this will subtract the previous background scan from future measurements).

Troubleshooting

Sometimes the program will freeze up. The solution is usually to stop the program, push the reset button on the PI Detector controller, and run the program again, making sure to select the `init CCD` button. Occasionally, Labview needs to be restarted altogether. Also, there seems to be more communication problems when the ICCD is run at a repetition rate of 2 Hz or faster.

G.1.9 Lamp

White light is provided by an Oriel Quartz-Tungsten-Halogen lamp in an Oriel lamp housing with an Oriel 300 W Radiometric Power Supply (Model 68831). The

light is coupled into a multimode optical fiber (62.5 μm core) in order to provide a more point-like source for reflectivity/transmission experiments. The lamp is typically run at 100 W (electrical power), but only about 20 μW is typically coupled into the fiber since the lamp is an extended source. The power supply (not the lamp itself) is left on all the time.

G.1.10 LEDs

There are two near-infrared LEDs, both of which are manufactured with receptacles (FC) that allow direct connection to an optical fiber. The LEDs used have broad (50 nm FWHM) emission wavelengths centered at either 810 nm (Zarlink MF272) or 850 nm (Appointech). They are both mounted in a box with the diode leads connected to BNC inputs. The maximum dc forward current is 100 mA for the 810 nm LED and 60 mA for the 850 nm LED. About 100 μW is coupled into the fiber (62.5 μm core) for the 850 nm LED near its maximum current, while significantly less is coupled into the fiber for the 810 nm LED. The coupled power can vary quite a bit from one LED to another.

For simple reflectivity/transmission experiments, the LEDs can be sourced with the Keithley 230 voltage source. For THz EO experiments, in which the LED must be pulsed, the HP 214B Pulse Generator must be used as it can supply the large peak currents needed. Due to the low differential resistance of the LEDs

for forward voltages, the pulsed voltage must be turned up fairly high in order to get powers of $\sim$100 μW.

G.1.11 SRS Pulse generator

This SRS DG535 pulse generator is used to control all of the timing. It can be triggered internally or by the FEL advanced trigger. One output (AB) provides a pulse for the RF source of the AOM and usually triggers the scope or the lock-in. The other output (CD) provides voltage pulses for the sample or triggers the HP high voltage pulse generator.

Labview vi's

1. `SRDG535.vi`: Sets the output voltage of output CD. It can only be set to one polarity and cannot be set to zero. For voltage scans the program prompts the user when the polarity needs to be changed or when the sample should be shorted. The voltage when the polarity needs to be changed is determined by the voltage step size and must be changed in the program.

G.1.12 Keithley 230 voltage source/Keithley 196 DMM

Labview vi's

1. `Keithley 196 DMM Read.vi`: Reads Keithley DMM
2. `Keithley 230.vi`: Sets Keithley 230 voltage
3. `SimpleIV.vi`: Measures IV curve using the two Keithley's.

G.1.13 HP scope

Labview vi's

1. `Sig_avg2.vi`: Measures signal and background on scope (2 channels at once). The times over which the signal and background are averaged are set in `Scope globals`.
2. `Scope globals`: Labview global variable that stores the time intervals for the signal and background for two channels.
3. `SPEX w_scope.vi`: Scans SPEX wavenumber and measures scope.

G.1.14 SRS 830 lock-in amplifier

Labview vi's

1. `SR830_Read.vi`: Reads in-phase and quadratures signals from lock-in

2. `SR830_Read_autoscale.vi`: Reads in-phase and quadratures signals from lock-in and tries to auto scale. (Not recommended)

3. `SPEX w_SR830 no auto read.vi`: Scans SPEX wavenumber and measures lock-in. (no autoscale feature)

G.2 Alignment and collection procedures

G.2.1 NIR and THz alignment

Realignment of the NIR and THz beams at the sample must be performed for THz EO experiments occasionally. Fig. G.1(a) provides a good reference when visualizing this procedure.

1. Send the Ti:Sapphire through the focusing lens onto a sample (at room temperature).

2. Find the reflected beam and adjust the sample position until the reflected beam is well collimated far away from the lens. This ensures that the NIR

focus is at the sample.

3. Turn on the FEL alignment laser. It should be focused by the off-axis-parabolic (OAP) to a spot near the edge of the sample.

4. Make sure the alignment laser focus looks good (circular spot instead of ellipse). The OAP is mounted on a mirror mount so the angle can be adjusted to improve the focus.

5. Center alignment laser focus on sample edge by translating the OAP (for rough alignment, if needed) and by adjusting the OAP mount (for fine alignment). Make sure the focus isn't messed up in this process.

6. Move the sample out of the way and place a card at the intersection of the beams.

7. Move the NIR beam to the center of the alignment laser focus by translating the NIR focusing lens. If they are too far off, better rough alignment must be done.

The alignment from this procedure should be pretty good although the focus of the alignment laser may not be the same as the focus for the THz beam. Adjustments can be made during THz EO measurements to improve the alignment as long as the initial alignment is good enough.

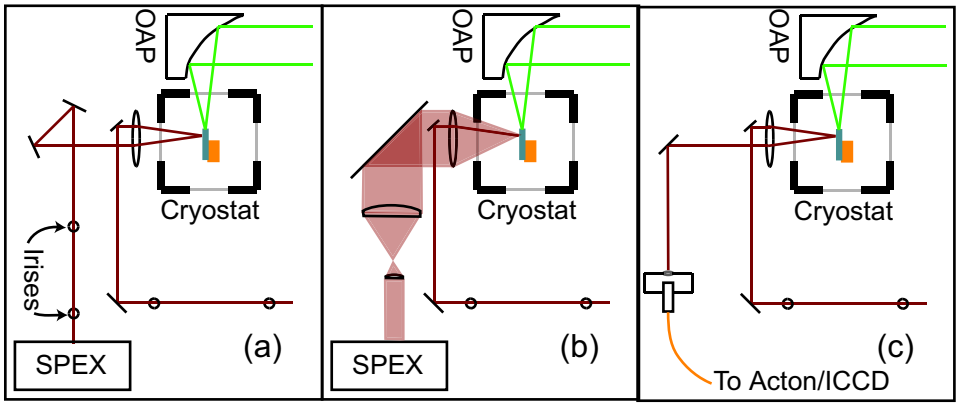

Figure G.1: Collection setups for (a) sending the reflected NIR beam and any sidebands to the SPEX, (b) sending PL to the SPEX, and (c) sending the reflected NIR beam to the Acton/ICCD.

When the beams are aligned, two irises should be placed in the NIR beam path before the focusing lens so that the laser can just be aligned to these two points in the future. A large iris can be placed in the THz beam path as well, making sure the THz beam always comes in along the same path.

G.2.2 NIR collection

NIR light from sideband, reflectivity, transmission, and PL measurements must be collected and sent to the SPEX/PMT or the Acton/ICCD. Figure G.1 displays three different collection setups commonly used. When sending light to the SPEX, free-space optics are used. NIR light is aligned to two irises as described in Section G.1.6. Reflected/transmitted beams along with any sidebands are aligned using two mirrors before the irises (see Fig. G.1(a)), but PL is more complicated. The

PL is collimated by a 2 inch lens, so the PL diameter is too big for the 1 inch mirrors used. Instead, the PL is reduced by two lenses and then aligned to the SPEX (see Fig. G.1(b). This method is rather difficult and sometimes results in poor coupling into the SPEX.

When the Acton/ICCD is used, the NIR light must be coupled into an optical fiber since the Acton/ICCD is on a different table. The setup for collection of the reflected NIR beam is displayed in Fig. G.1(c). Typically, a compact Thorlabs fiber optic collimator is used to couple light into the fiber. The easiest method of alignment is to send light from another source through the other end of the fiber for back-alignment. (The Oriel lamp or even a desk lamp pushed up near a fiber coupler works well.) The NIR beam is then aligned to the secondary source coming out of the fiber optic collimator. When PL is sent to the Acton/ICCD, the setup in Fig. G.1(b) is used with the fiber optic collimator placed before the SPEX.

G.3 Measurement Procedures

G.3.1 Sideband Measurements

There are a quite a few sideband measurements that can be performed, but the initial procedure is always roughly the same.

Initial Procedure

1. Evacuate cryostat, cool down

2. Turn on Argon laser/Ti:Sapphire laser, allow to warm up 15 min, set power to 6.5 W (light regulation), check Ti:Sapphire power.

3. Turn on RF source for AOM; SRS pulse generator; SRS high voltage power supply; scope; lock-in; preamp.

4. Pulse Ti:Sapphire at 1.5 Hz, high duty-cycle. Make sure 1st order beam from AOM is strong, hole in zeroth order beam.

5. Chop Ti:Sapphire at 1 kHz (using AOM), 50% duty-cycle.

6. Align Ti:Sapphire to two irises before cryostat by adjusting two periscope mirrors. Typically full Ti:Sapphire power is necessary to see the beam well on the irises. Make sure beam is blocked. Put attenuators back in afterward.

7. Disconnect pump from cryostat if not done already.

8. Move cryostat until NIR beam hitting near the sample edge by looking at sample through focusing lens. (Make sure any reflected beams are blocked, so you don't fry your eyes.)

9. Turn on FEL alignment laser, make sure passing through alignment iris correctly. Move sample until alignment laser focus is hitting the sample's edge. Use a dental mirror to see in the side.

10. Align reflected NIR beam to SPEX. Shutter should be closed.

11. Put in attenuators before the SPEX. With ∼0.5 mW incident on the sample, attenuation of OD5 is appropriate.

12. Turn on high voltage to PMT, move SPEX to laser wavenumber.

13. Connect PMT signal from the preamp (usu. set to amplify ×20) to the lock-in. The lockin should be triggered by the SRS pulse generator.

14. Open SPEX shutter, if no signal use `SPEX w_SR830 no auto read.vi` to do a short scan.

15. Peak laser signal up. Do another SPEX scan to find the laser wavenumber, move SPEX there.

16. Initialize SPEX (using `SPEX init.vi`) to the wavenumber shown on the wavelength meter.

17. Close SPEX shutter, take out attenuators, move laser to good wavenumber for sidebands.

18. Trigger pulse generator with FEL advanced trigger, pulse Ti:Sapphire for $\sim$200 μs, apply any voltages to the sample.

19. Move SPEX to expected sideband wavenumber using `Goto Sideband.vi`, connect trigger and PMT signal to scope.

20. Connect pyro signal to scope, make sure there's a signal.

21. Open SPEX shutter, shout "Hooray" if you see sidebands. Make sure the preamp isn't overloaded.

22. Perform a short sideband scan using `SPEX w_scope.vi` to determine the sideband offset (should be the FEL wavenumber for $n = 1$ sidebands).

23. Peak up the sideband signal by attenuating FEL power some (so power dependence is linear) and tweaking the OAP mount. Then adjust the sample position to increase signal.

When performing other measurements, make sure the SPEX never passes through the laser wavenumber unless attenuated. This usually means closing the SPEX shutter (or blocking the laser) when moving the laser or SPEX wavenumber.

Troubleshooting (no sideband signal)

1. FEL blocked or alignment laser on? Check reference pyro signal.

2. Check the timing

3. Make sure the Ti:Sapphire isn't jumping around.

4. Check that PMT signal is going to scope

5. Turn on FEL alignment laser, make sure hitting sample edge.

Labview vi's

1. `Goto Sideband.vi`: Iteratively seeks out laser wavenumber and moves SPEX to SB position.

2. `Resonance scan.vi`: Scans laser wavenumber and SPEX with fixed offset, measures signal on scope.

3. `Sweep V w_scope.vi`: Scans voltage while measuring signal on scope. For Sideband voltage scans.

4. `Scan laser and SPEX and V.vi`: Runs `Sweep V w_scope.vi` for many laser wavenumbers. For SB maps.

5. `powerdep.vi`: Measures scope for FEL power dependence.

6. `powerdepNIR.vi`: Measures scope for NIR power dependence.

G.3.2 Change in Reflectivity/Transmission using LED

1. Evacuate cryostat, cool down
2. Start up ICCD, turn on SRS pulse generator, HP high voltage pulse generator.
3. Turn on Oriel lamp, couple to optical fiber.
4. Flip in mirror sending fiber output onto NIR optical path (see Fig. 2.9 on page 40), align beam to irises.
5. Disconnect pump from cryostat if not done already.
6. Move cryostat until NIR beam hitting near the sample edge by looking at sample through focusing lens. (Make sure reflected beams are blocked.)
7. Turn on FEL alignment laser, make sure passing through alignment iris correctly. Move sample until alignment laser focus is hitting the sample's edge. Use a dental mirror to see in the side.
8. Couple reflected/transmitted beam into fiber.
9. Look at ICCD signal on computer and peak up signal by adjusting coupling into fiber.
10. Connect pyro signal to scope, make sure there's a signal.

11. Connect ICCD gate reference to scope. Adjust gate until ICCD detecting only during the relatively flat part of the FEL pulse (1-2 μs).

12. Connect HP pulse generator output to scope, center on FEL pulse/ICCD gate. Voltage pulse should be $\sim$10 μs long.

13. Connect HP pulse generator output to LED while leaving connected to scope. Connect fiber to LED instead of lamp.

14. Look for ICCD signal on computer. Increase LED voltage until enough signal, while monitoring the voltage on the scope.

15. Peak up any change in reflectivity/transmission due to the FEL by adjusting OAP mount, sample position.

16. Take a background spectrum with `background` button in vi selected, block LED.

17. Take reflectivity/transmission spectra with `background` button deselected.

This procedure can easily be modified for doing linear reflectivity/transmission measurements without the FEL. The lamp can be used in these cases instead of the LEDs.

Labview vi's

1. `ICCD Front Panel_FEL2`: Same as `ICCD Front Panel` but also measures the reference pyro signal on the scope and stores in separate files.

G.3.3 Change in Reflectivity/Transmission using Ti:Sapphire

1. Evacuate cryostat, cool down
2. Turn on Argon laser/Ti:Sapphire laser, allow to warm up 15 min, set power to 6.5 W (light regulation), check Ti:Sapphire power.
3. Turn on RF source for AOM; SRS pulse generator; scope.
4. Pulse Ti:Sapphire at 1.5 Hz, high duty-cycle. Make sure 1st order beam from AOM is strong, hole in zeroth order beam.
5. Align Ti:Sapphire to two irises before cryostat by adjusting two periscope mirrors. Typically full Ti:Sapphire power is necessary to see the beam well on the irises. Make sure beam is blocked. Put attenuators back in afterward.
6. Disconnect pump from cryostat if not done already.
7. Move cryostat until NIR beam hitting near the sample edge by looking at sample through focusing lens. (Make sure any reflected beams are blocked, so you don't fry your eyes.)

8. Turn on FEL alignment laser, make sure passing through alignment iris correctly. Move sample until alignment laser focus is hitting the sample's edge. Use a dental mirror to see in the side.

9. Send reflected/transmitted beam to photodiode, connect output to amplifier, then to scope. (See below for photodiode and amplifier options.)

10. Trigger SRS pulse generator with FEL advanced trigger, pulse Ti:Sapphire for $\sim$200 μs

11. Connect pyro signal to scope, make sure there's a signal.

12. Move Ti:Sapphire to wavenumber where changes are expected. Look for change in reflectivity/transmission on the scope.

13. Peak up changes in signal with FEL attenuated as much as possible by adjusting the OAP mount and the sample position.

14. Take spectra using `drefl.vi`.

There is a very small photodiode that can be used in conjuction with the SRS preamp to get a time resolution of roughly 0.5 μs. There is also a $\sim$0.5 μs delay when using the SRS preamp. A large area photodiode can be used with a fast preamp (Matec model 254) to get a time resolution of $\sim$100 ns. The signal to noise tends to be much better using the SRS preamp.

Labview vi's

1. `drefl.vi`: Scans the NIR laser and measures the reflected signal on the scope with and without the FEL using `Sig_avg2.vi`.

G.3.4 Change in Photoluminescence with Acton/ICCD

1. Evacuate cryostat, cool down

2. Turn on Argon laser/Ti:Sapphire laser, allow to warm up 15 min, set power to 6.5 W (light regulation), check Ti:Sapphire power.

3. Turn on RF source for AOM; SRS pulse generator; HP scope.

4. Pulse Ti:Sapphire at 1.5 Hz, high duty-cycle. Make sure 1st order beam from AOM is strong, hole in zeroth order beam.

5. Align Ti:Sapphire to two irises before cryostat by adjusting two periscope mirrors. Typically full Ti:Sapphire power is necessary to see the beam well on the irises. Make sure beam is blocked. Put attenuators back in afterward.

6. Disconnect pump from cryostat if not done before.

7. Start up ICCD

8. Move cryostat until NIR beam hitting copper sample mount (to get lots of scattered light). Set laser to lowest wavelength available (in order to see it), take out one NIR attenuator to get ∼5 mW.

9. Align scattered light to fiber coupler.

10. Put NIR attenuator back in, move cryostat until NIR beam hitting sample edge. Change Ti:Sapphire to appropriate excitation wavelength.

11. Look at ICCD signal on computer and peak up signal by adjusting coupling into fiber.

12. Connect pyro signal to scope, make sure there's a signal.

13. Connect ICCD gate reference to scope. Adjust gate until ICCD detecting only during the FEL pulse.

14. Peak up any change in PL due to the FEL.

15. Take a background spectrum with `background` button in vi selected, block LED.

16. Take PL spectra with `background` button deselected.

This procedure can easily be modified for measuring PL without the FEL. The PL can be sent to the SPEX in this case as well.